
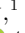

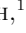















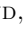


The Lyman α Reference Sample XIV: Lyman α imaging of 45 low redshift star-forming galaxies and inferences on global emission.

JENS MELINDER ¹, GÖRAN ÖSTLIN ¹, MATTHEW HAYES ¹, ARMIN RASEKH ¹, J. MIGUEL MAS-HESSE ²,
JOHN M. CANNON ³, DANIEL KUNTH ⁴, PETER LAURSEN ^{5,6}, AXEL RUNNHOLM ¹, E. CHRISTIAN HERENZ ⁷,
MATTEO MESSA ^{1,8}, DANIEL SCHAEERER ⁸, ANNE VERHAMME ⁸, T. EMIL RIVERA-THORSEN ¹, LUCIA GUAITA ^{9,10},
THOMAS MARQUART ¹¹, JOHANNES PUSCHNIG ¹², ALEXANDRA LE RESTE ¹, ANDREAS SANDBERG ¹, EMILY FREELAND ¹
AND JOANNA BRIDGE

¹Stockholm University, Department of Astronomy and Oskar Klein Centre for Cosmoparticle Physics, AlbaNova University Centre, SE-10691, Stockholm, Sweden

²Centro de Astrobiología (CAB), CSIC-INTA, ESAC, 28692 Villanueva de la Cañada, Spain

³Department of Physics & Astronomy, Macalester College, 1600 Grand Avenue, Saint Paul, MN 55105, USA

⁴Institut d'Astrophysique, Paris, 98 bis Boulevard Arago, F-75014 Paris, France

⁵Cosmic Dawn Center (DAWN)

⁶Niels Bohr Institute, University of Copenhagen, Jagtvej 128, DK-2200, Copenhagen N, Denmark

⁷European Southern Observatory, Av. Alonso de Córdova 3107, 763 0355 Vitacura, Santiago, Chile

⁸Geneva Observatory, University of Geneva, 51 Chemin des Maillettes, CH-1290 Versoix, Switzerland

⁹Departamento de Ciencias Físicas, Facultad de Ciencias Exactas, Universidad Andres Bello, Fernandez Concha 700, Las Condes, Santiago, Chile

¹⁰Núcleo de Astronomía, Facultad de Ingeniería y Ciencia, Universidad Diego Portales, Av. Ejército 441, Santiago, Chile

¹¹Department of Astronomy and Space Physics, Box 515, 75120 Uppsala, Sweden

¹²Universität Bonn, Argelander-Institut für Astronomie, Auf dem Hügel 71, D-53121 Bonn, Germany

ABSTRACT

We present Ly α imaging of 45 low redshift star-forming galaxies observed with the Hubble Space Telescope. The galaxies have been selected to have moderate to high star formation rates using far-ultraviolet (FUV) luminosity and H α equivalent width criteria, but no constraints on Ly α luminosity. We employ a pixel stellar continuum fitting code to obtain accurate continuum subtracted Ly α , H α and H β maps. We find that Ly α is less concentrated than FUV and optical line emission in almost all galaxies with significant Ly α emission. We present global measurements of Ly α and other quantities measured in apertures designed to capture all of the Ly α emission. We then show how the escape fraction of Ly α relates to a number of other measured quantities (mass, metallicity, star formation, ionisation parameter, and extinction). We find that the escape fraction is strongly anti-correlated with nebular and stellar extinction, weakly anti-correlated with stellar mass, but no conclusive evidence for correlations with other quantities. We show that Ly α escape fractions are inconsistent with common dust extinction laws, and discuss how a combination of radiative transfer effects and clumpy dust models can help resolve the discrepancies. We present a star formation rate calibration based on Ly α luminosity, where the equivalent width of Ly α is used to correct for non-unity escape fraction, and show that this relation provides a reasonably accurate SFR estimate. We also show stacked growth curves of Ly α for the galaxies that can be used to find aperture loss fractions at a given physical radius.

Keywords: cosmology: observations — galaxies: evolution — galaxies: starburst — radiative transfer — ultraviolet: galaxies — techniques: image processing — methods: data analysis

1. INTRODUCTION

Photons emitted in the Ly α line at 1216 Å (carrying an energy of 10.2 eV) come from a radiative transition in the hydrogen (H I) atom from the second lowest en-

ergy state to the ground state ($2p$ to $1s$). The flux emitted in this line comes from two processes, recombination and collisional excitation. Recombination, when ionized atoms recombine with free electrons which go through a cascade of radiative transitions to reach the ground state, is the more important of these (responsible for $\sim 90\%$ of the line flux). In this way ionized gas will emit photons in a number of emission lines at different wavelengths, with energies corresponding to the energy levels involved. Ly α is a resonance line and has the highest transition probability of all radiative transitions in the hydrogen atom — roughly 68% of all recombination events result in the emission of Ly α photon (assuming case B recombination and a gas temperature of 10^4 K, [Dijkstra 2014](#)). Because of the resonant nature of the line a large majority of the Ly α photons emitted from the nebular regions will typically be re-absorbed and re-emitted many times by the neutral interstellar medium (ISM) on their way out from the galaxies. This means that ISM properties affecting radiative transfer — such as kinematics, neutral gas geometry, and dust column densities — will be very important, and needs to be taken into account when estimating the output Ly α luminosity (e.g. [Laursen et al. 2009](#); [Verhamme et al. 2012](#); [Gronke & Dijkstra 2016](#)).

Given that hydrogen is the most common element in the Universe, and is the fundamental ingredient in the star formation process, studying molecular, neutral, and ionized hydrogen in both absorption and emission is an important window to the astrophysics of galaxies. Young and massive stars dominate the radiation output of star-forming galaxies, and are mostly distributed in stellar clusters. The regions close to these intense sites of star formation are mostly ionized (H II regions), and thus emit strongly in recombination lines. This radiation is also known as nebular line emission, and for non-resonant hydrogen transitions (such as the optical Balmer recombination lines H α and H β) measurements of the nebular line strength can be used to accurately determine the luminosity of ionizing photons from massive stars in star-forming regions inside galaxies, and thereby infer the star formation rate (SFR) in them.

Because of the strength and rest wavelength of the Ly α line it was suggested as a probe of high redshift galaxies already by [Partridge & Peebles \(1967\)](#). However, the first searches for Ly α emission in nearby star-forming galaxies were largely unsuccessful. Instead of a strong emission line, Ly α was found to be in absorption or much weaker than expected ([Meier & Terlevich 1981](#)). Absorption of continuum and Ly α photons by the surrounding neutral medium is of course expected, and even in strong emitters the line is often superposed

on an absorption trough. The measured Ly α flux from these galaxies did thus not match the expectations from the photon production as estimated from stellar continuum or H α observations. Furthermore, the unexpected weakness of the Ly α emission was also observed for active galactic nuclei ([Davidson et al. 1977](#)).

With more sensitive space-based instruments (i.e., International Ultraviolet Explorer — IUE, Hopkins Ultraviolet Telescope — HUT, Galaxy Evolution Explorer — GALEX, Hubble Space Telescope — HST) and larger galaxy samples extragalactic spectroscopic Ly α detections in star-forming galaxies became common-place (e.g., [Giavalisco et al. 1996](#)). These single aperture/slit observations did not have any information on the spatial distribution of Ly α . For the HST Cosmic Origins Spectrograph (COS) observations the physical size of the aperture was also quite small and aperture losses of scattered Ly α emission were thus likely large and impossible to constrain. The first Ly α imaging at high resolution of low redshift galaxies showed the effects of scattering clearly ([Kunth et al. 2003](#); [Hayes et al. 2005](#); [Östlin et al. 2009](#)), but the observations were hampered by the strong background of geocoronal Ly α emission present in the line filter. The *Lyman- α Reference Sample* (LARS) was designed to simultaneously measure Ly α emission on small scales (using HST/COS spectroscopy) and large scales (using far-ultraviolet — FUV — imaging) for an unbiased sample of highly star-forming galaxies. The first part of the sample, which contains 14 galaxies, was presented in [Hayes et al. \(2014\)](#) and [Östlin et al. \(2014\)](#). By combining data from many different instruments and wavelength ranges this study made it possible to perform a systematic investigation of global Ly α emission and how it relates to other galaxy properties. In addition, the relatively large field of view of the FUV imaging data allowed measuring and characterizing the Ly α halos (scattered emission) in a sample of well-characterized galaxies for the first time ([Guaita et al. 2015](#); [Rasekh et al. 2022](#)). These studies, and others (e.g., [Yang et al. 2017a](#)), have strongly confirmed the theoretical predictions (e.g., [Laursen et al. 2009](#)) that the radiative transfer causes Ly α radiation to be spatially scattered and thus significantly more extended than both the stellar continuum and the non-resonant nebular line emission.

Studies of star-forming galaxies in the nearby universe have shown that strong net Ly α emission is associated with: high specific SFRs (e.g., [Cowie et al. 2011](#); [Hayes et al. 2014](#)), low extinction (e.g., [Giavalisco et al. 1996](#); [Hayes et al. 2014](#)), low metallicity (e.g., [Giavalisco et al. 1996](#)), low neutral gas covering fraction (e.g., [Rivera-Thorsen et al. 2015](#)), high ionisation parameter (e.g., [Yang et al. 2017a](#)), turbulent ionised gas kinematics

(e.g., Herenz et al. 2016), and significant outflow velocities (e.g., Kunth et al. 1998; Heckman et al. 2011). However, while these conclusions hold when comparing strong emitters to non-emitters, they should not be mistaken for direct correlations. Comparisons of Ly α relative output (equivalent widths, $W_{\text{Ly}\alpha}$, or escape fractions, f_{esc}) with these observables for galaxies with non-zero escape show either no (sSFR, metallicity), weak (H I covering fraction, outflow velocity), or fairly strong correlations (extinction) — and with significant scatter that cannot be explained by measurement uncertainties (Hayes 2015). Recently, Runnholm et al. (2020) published a statistical study of the LARS galaxies. By using multivariate regression techniques they show that a combination of observables can be used to predict Ly α output of star-forming galaxies to within a factor of $\sim 50\%$ (0.19 dex). In this study the most important observables for predicting Ly α luminosity were found to be FUV luminosity and extinction. The distribution and surface brightness profile derived properties of Ly α for the sample used in this paper were studied in Rasekh et al. (2022). The main results from this paper were that brighter Ly α emitters have smaller halo fractions (a smaller fraction of their Ly α emission is detected far from star-forming regions) and that the spatial distribution of Ly α from them is more circularly symmetric. However, the correlations found in this work are quite weak and show significant scatter. Investigations of the neutral gas (H I) in the LARS galaxies are currently ongoing and results from part of the sample have been published in Pardy et al. (2014) and Le Reste et al. (2022). A comparison of the neutral gas and Ly α properties of the full sample will be presented in Le Reste et al. (in prep.).

The dependence on extinction has been further explored by, e.g., Scarlata et al. (2009), Atek et al. (2014), and Bridge et al. (2018). These studies show that even with radiative transfer effects a simple dust screen model is insufficient to explain the observations. Most galaxies have escape fractions that are lower than expected, which is a natural consequence of resonant radiative scattering increasing the path lengths, and thus causing Ly α radiation to suffer from more extinction than nebular extinction measurements using other (non-resonant) recombination lines would indicate. However, many galaxies with quite substantial nebular extinction have Ly α escape fractions that far exceed the fractions inferred from observed H α /H β ratios and using standard extinction curves.

At high redshift ($z = 2 - 7$) Ly α can be used to detect galaxies, and to spectroscopically confirm their redshifts (e.g., Malhotra & Rhoads 2004). The first sam-

ples of Ly α emitters (LAEs) were found using narrow-band techniques (e.g., Cowie & Hu 1998), which enables surveys covering large areas at specific high redshift slices, but provides no information on the Ly α line profile. Narrow band Ly α observations — combined with broad band imaging to reject low redshift interlopers — thus provides a powerful and secure method to find high redshift galaxies (e.g., Ouchi et al. 2018), but it is very challenging to characterize them further using only low spatial resolution imaging. Follow-up Ly α spectroscopy of high- z galaxies (e.g., Erb et al. 2014; Sobral et al. 2018) and direct Ly α spectroscopy using Integral Field Unit (IFU) spectroscopy (e.g., Adams et al. 2011; Herenz et al. 2017) have provided a wealth of data on high redshift LAEs. Trainor et al. (2019) present optical spectroscopy for a large sample (~ 700) of redshift 2–3 LAEs, finding that the equivalent width of metal line absorption (related to neutral gas density or geometry) and the [O III]/H β ratio (indicating overall ionisation state) can be used to predict $W_{\text{Ly}\alpha}$, albeit with large scatter. With simple assumptions on the stellar population age and star formation history, and without accounting for radiative scattering in a dusty medium, the escape fraction of Ly α should be directly proportional to the equivalent width (Sobral & Matthee 2019). Sobral & Matthee (2019) use this to construct an empirical estimator of escape which relies only on $W_{\text{Ly}\alpha}$. However, many of the high redshift Ly α surveys are limited to either massive galaxies (when pre-selected from broad-band surveys) or to strong Ly α emitters (narrow-band or direct spectral detections), and it is uncertain if the same correlations and conditions also apply to low-mass galaxies or galaxies with low f_{esc} and high extinction.

The first observations of large scale Ly α halos at high redshift were done by Steidel et al. (2011) in a stack of Lyman break galaxies at $z \sim 3$. The stacked narrow-band images showed extended Ly α halos surrounding the galaxies. The spatial scales are very large compared to observations of extended Ly α in nearby galaxies (Guaita et al. 2015; Rasekh et al. 2022), but the sample properties and resolution/field-of-view are very different. Other narrow-band and IFU spectroscopy surveys also show the same, Ly α is invariably more extended than the FUV (e.g., Momose et al. 2014; Leclercq et al. 2017) or H α emission (e.g., Matthee et al. 2016).

With observations of low redshifts LAEs giving a more comprehensive understanding of the effects that radiative transfer has on the Ly α output, current and future Ly α surveys will give important constraints on reionisation and the very first galaxies (e.g., Jensen et al. 2013; Smith et al. 2015; Runnholm et al. 2020). In this work, we present the extension of LARS (eLARS), in-

creasing the number of nearby star-forming galaxies imaged in Ly α from 14 to 45 and widening the sample window to include also galaxies with lower star formation rates. This paper is organized as follows. In Section 2 we describe the data set used in this work along with details on the data reduction. In Section 3 we outline the Ly α continuum subtraction method used and also specify the assumptions and limitations of the code. In addition, this section contains a description on how we determine sizes and perform photometry on the various line, continuum, and property maps. In Section 4 we present maps of Ly α , FUV continuum and H α for the 45 galaxies, along with surface brightness profiles, and demonstrate that the Ly α is more extended than FUV/H α emission in all galaxies with significant Ly α escape. Section 5 presents global measurements of Ly α and other quantities from our data and also investigates possible correlations between them. In Section 6 we discuss some implications of our results and how they compare to previous work. Finally, Section 7 summarizes our conclusions and results. Together with this paper we also release Ly α images and accompanying reduced HST data for the 45 galaxies to the community.

Throughout this paper we use a Λ CDM cosmology with $\{H_0, \Omega_m, \Omega_\Lambda\} = \{70 \text{ km s}^{-1} \text{ Mpc}^{-1}, 0.3, 0.7\}$.

2. THE DATA

2.1. Overall survey strategy

The observational strategy for LARS is described in detail by Östlin et al. (2014), and the same strategy for imaging Ly α emission from a combination of broad and narrow-band HST filters is employed for the extended sample. For clarity we give a brief description of the strategy here. The basic idea is to use a combination of FUV filters of the Solar Blind Channel of the Advanced Camera for Surveys (ACS/SBC) on the Hubble Space Telescope (HST) to measure the flux emitted in nebular Ly α emission and the FUV stellar continuum, and then isolate the emission from the Ly α emission line using continuum subtraction methods. This strategy was employed by Kunth et al. (2003) to obtain the first HST Ly α image of a low redshift galaxy, and later for a sample of six blue compact galaxies (Hayes et al. 2005, 2007; Östlin et al. 2009). These earlier surveys used the F122M filter in the SBC as the Ly α on-line filter. For the LARS galaxies, which are at slightly higher redshift, it was possible to use a different filter setup, utilizing multiple long-pass filters of the SBC. In addition to the much lower geocoronal background the higher throughput of the long-pass filters combined with having sharp cut-on profiles on the blue side, means that con-

tinuum subtraction using these filters are more contrast sensitive and can reach lower $W_{\text{Ly}\alpha}$ levels.

The slope of the stellar continuum spectrum at the wavelength of Ly α is highly sensitive to the age of the stellar population and effective attenuation from dust (to a lesser extent, also to stellar metallicity). The slope for a stellar population producing Ly α is not very sensitive to age, but the continuum subtraction needs to be performed also in regions that do not produce Ly α photons (due to scattering). Hence, without access to multiple filters spanning both blue- and redward of the Ly α line, spectral energy distribution (SED) fitting is needed to accurately estimate the FUV continuum flux. Hayes et al. (2009) showed that to securely constrain the effect on the FUV continuum of stellar ages, mass, and stellar attenuation at least four continuum data points are needed, spanning the FUV to optical wavelength range. A further refinement to the method is possible by adding narrow-band observations of H α which makes it possible to quantify the contribution of nebular continuum to the SED (along with H β to extinction correct the H α map). The details of SED fitting and continuum subtraction is further described in Sec. 3.1

To summarize, the imaging observations obtained for the original 14 galaxies and the extended sample are three FUV filters (one containing Ly α emission), three ultraviolet/optical broad band filters, and two optical narrow-band filters (for H α and H β). For three of the galaxies (LARS 13, LARS 14, and Tololo 1247-232) only one FUV continuum filter was used.

2.2. Sample selection

The availability of FUV long-pass filters in SBC sets the upper limit on redshift of the galaxies that can be targeted with our technique. The longest wavelength SBC long-pass filter is F165LP, and at least one continuum FUV filter is needed for accurate continuum subtraction. This means that the reddest Ly α on-line filter that can be used is F150LP, giving an upper redshift limit of 0.3 (but note that the longer wavelength SBC filters are less efficient, which makes it hard to target faint galaxies at high redshift). Geocoronal Ly α emission and Milky Way absorption of Ly α puts a lower limit to the redshift range at around 0.01. The selection of galaxies included in the original LARS sample is described in detail by Östlin et al. (2014). The main astrophysical selection criteria are star formation rate (based FUV luminosity) and stellar age (using H α equivalent width, $W_{\text{H}\alpha}$). Given that the H α line fluxes are measured in SDSS apertures they will underestimate the total SFR of larger galaxies. The $W_{\text{H}\alpha}$ cut of 100 Å in particular means that the sample only includes galaxies with young

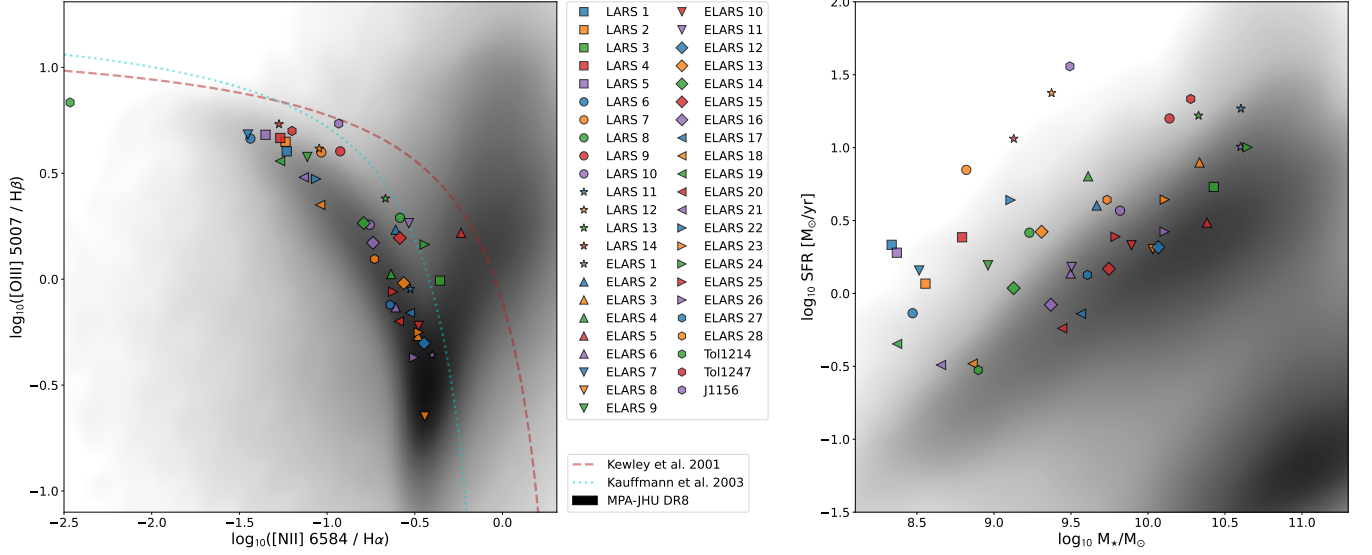


Figure 1. Left panel: Emission line diagnostics for the sample. The grey-shaded region shows the density of galaxies from SDSS DR8. All but one of the galaxies fall in the region dominated by emission from H II regions. Right panel: Galaxy main sequence diagram using data from the JHU-DR8 derivation of stellar masses and SFRs. Note that Tol 1214 and Tol 1247 do not have SDSS data and emission line data from other sources (see Table 1) are used. LARS 9 is not included in the MPA-JHU DR8 catalogues, for this galaxy we use SFR and stellar mass from the Granada Flexible Stellar Population Synthesis analysis of DR14 data (Montero-Dorta et al. 2016). Note the majority of galaxies in the sample are not included in the DR9+ stellar mass and emission line property catalogues, which is why we chose to use DR8 for this comparison.

stellar populations that produce Ly α photons. This selection also leads to the sample being biased towards high specific SFR (irregular and merging systems), and against the inclusion of high mass galaxies.

For the extended sample we decided to broaden the criteria and include galaxies with lower specific star formation rate ($W_{\text{H}\alpha} > 40 \text{ \AA}$). Most of these galaxies are also thus naturally fainter in the FUV and to reach acceptable signal to noise while optimizing the use of HST exposure time we elected to observe targets in the continuous viewing zone (CVZ) (at $\delta \sim 60 \text{ deg}$). The longer HST orbit time makes the observations more efficient, but has the drawback that contamination from the [O I] geocoronal emission is harder to avoid (see Section 2.3). Furthermore, given the overall lower surface brightness of the galaxies we also chose to only include lower redshift galaxies ($z \lesssim 0.05$) in the extended sample. The lower redshift cut-off was 0.028 which was selected to get a throughput for the Ly α line of $> 85\%$ in the F125LP filter. The redshift band $0.036 < z < 0.044$ was excluded to avoid contamination of the [O III] 4959+5007 \AA lines in the H β narrow-band filter.

With these considerations taken into account we started off by selecting galaxies from the Sloan Digital Sky Survey (SDSS, DR8) with $W_{\text{H}\alpha} > 40 \text{ \AA}$ and matched the coordinates to the GALEX (DR3) catalogues to find FUV fluxes for the sources. Similar to the original LARS selection we excluded active galactic

nucleus (AGN) galaxies by rejecting galaxies with H α line widths (FWHM) larger than 300 km s^{-1} (or line of sight velocity dispersion larger than 130 km s^{-1}), and with emission line ratio diagnostics from SDSS spectra ($[\text{O III}]/\text{H}\beta$ and $[\text{N II}]/\text{H}\alpha$). In addition we required the galaxies to have Milky Way extinction of less than 0.03. We then selected galaxies from the remaining list trying to cover a range of FUV luminosities — going down to $\log(L_{\text{FUV}}/L_{\odot}) = 9.0$ (with L_{FUV} from the GALEX FUV channel, defined as $\lambda \times L_{\lambda}$ at a rest wavelength of $1524 \text{ \AA} / (1+z)$), and morphologies — compactness, clumpiness, disk inclination, and spiral arm structure. The final number of galaxies selected using this method is 26 and are all part of the extended LARS observational programme. Compared to the original 14 galaxies this includes more continuously star-forming spiral galaxies.

In addition to these 40 galaxies we include five more galaxies in the sample, which all have the HST imaging required to perform the continuum subtraction. ELARS 1 (NGC 6090) is a luminous infrared galaxy which was also part of the Östlin et al. (2009) sample, but was missing H β narrow-band imaging. This galaxy and ELARS 2 (Markarian 65), a compact face-on spiral starburst galaxy, both fulfil the selection criteria and were already observed in the SBC long-pass filters as part of HST program 11110 (PI: S. McCandliss). Adding these galaxies to the sample was thus a

cheap addition in terms of observational time, and they were both part of the extended LARS observational program. Tololo 1247-232 is a Lyman continuum (LyC) leaking galaxy (Puschnig et al. 2017) and Tololo 1214-277 is a LyC leaker candidate (Östlin et al., in prep.). They were both observed with the LARS filter setup to study the connection between the escape of ionizing photons and Ly α . SDSS J115630.63+500822.1 is an extreme star burst galaxy at higher redshift than the rest of the sample and was observed in multiple FUV and optical filters by Hayes et al. (2016) in order to study extended O VI emission.

In Table 1 we show the basic properties that were used to select the sample. This table also includes the Galactic extinction (Schlafly & Finkbeiner 2011) from the Infrared Science Archive, NASA/IPAC (DOI:10.26131/IRSA537) along the sightline to the galaxies, these are very low for all of the galaxies by design. The physical properties of the galaxies, derived from the SDSS optical spectra, are given in Table 2. The SDSS star formation rates (SFR) and masses are taken from the MPA-JHU catalogue (Brinchmann et al. 2004; Salim et al. 2007). These are derived from H α and continuum spectral fitting, respectively, and we show the total estimates for SFR and stellar mass. For the emission line derived quantities (oxygen abundance and [O III] λ 5007/[O II] λ 3727 ratio), we use the SDSS based estimates from Runnholm et al. (2020). For the three galaxies not included there we use the references given in the table. Note that, apart from O32 and metallicity, we do not use the SDSS measurements for the analysis and comparisons done in this paper. They are presented here for completeness and to help characterize the sample properties.

The left panel of Figure 1 shows the location of the complete sample of galaxies in a standard BPT diagram (Baldwin et al. 1981). With the exception of one galaxy, the chosen sources all lie along the star-forming locus. The outlier (ELARS05) lies in a region of the diagram where galaxies with a low-ionisation nuclear emission-line region (LINER) normally fall. The inclusion of this source in the sample was not intended, and was likely caused by uncertain line fluxes in the selection process. The right panel of Figure 1 shows where the sample falls in a galaxy main sequence diagram (e.g., Brinchmann et al. 2004; Rodighiero et al. 2011). The grey-shaded region is a density map of SFR and stellar mass for nearby galaxies ($z \lesssim 0.2$) from the MPA-JHU analysis of emission line data in SDSS DR8. As noted above, the values for the LARS galaxies were pulled from the same catalogue (with a few exceptions given in the figure caption). While the final sample is not randomly selected

it should be noted that no information on actual Ly α emission was used in the process. The complete sample thus provides an unbiased data set of extended Ly α emission from star forming galaxies.

2.3. Observations

All observations were carried out using HST with three different cameras: ACS/SBC, ACS/Wide Field Camera (WFC), and Wide Field Camera 3 (WFC3)/UVIS. A list of which filters were used for the individual targets can be found in Table 7. While we used archival data when available the bulk of the data set consists of observations from HST program 12310 (Östlin et al. 2014, the original LARS, observed from 2010–2012), and HST program 13483 (ELARS, observed from 2013–2014). The observations for Tol 1214-277 come from HST program 14923 (Östlin et al., in prep.), for Tol 1247-232 from HST program 13027 (Puschnig et al. 2017), and for J1156 from HST program 13656 (Hayes et al. 2016, Rutkowski et al., in prep). All of the data presented in this paper were obtained from the Mikulski Archive for Space Telescopes (MAST) at the Space Telescope Science Institute. The specific observations analyzed can be accessed here: [10.17909/4s6m-7255](https://archive.stsci.edu/missions/Hubble/program/10.17909/4s6m-7255).

The FUV continuum and Ly α images were obtained with SBC. The FUV filter set was chosen to avoid contamination from geocoronal Ly α , but the O I λ 1302 Å line is strong enough to severely compromise the F125LP observations. The exposures in this filter were thus done with the telescope in Earth shadow. For the extended sample, which used a CVZ observational setup, this is harder to manage but the timing of the F125LP exposures was planned to minimize the time spent observing outside of shadow. We do not detect any significant change in the background between the original and the extended sample.

The typical exposure times in the Ly α filter were 3×600 s, and 3×400 in the continuum filters. Using three sub-exposures with small offsets for the SBC observations was done to cover the gap in the middle of the detector, and, to a smaller extent, limiting the effect of bad pixels in the detector.

The optical continuum of the galaxies was imaged in three filters with WFC3/UVIS (for some of the archival observations the ACS/WFC was used instead), in general using two blue (F336W and F438W) and one red (F775W) filter. For the ELARS observations with UVIS

Table 1. Sample characteristics

ID	SDSS ID	Redshift	$W_{H\alpha}$	$\log(L_{H\alpha})$	$\log(L_{FUV})$	$E(B - V)(MW)$	Common name
			(\AA)	(erg/s)	(L_{\odot})		
(1)	(2)	(3)	(4)	(5)	(6)	(7)	(8)
LARS01	SDSS-J132844.05+435550.5	0.028	560	41.43	9.92	0.0144	Mrk 259
LARS02	SDSS-J090704.88+532656.6	0.030	312	40.77	9.48	0.0152	Shoc 240
LARS03	SDSS-J131535.06+620728.6	0.031	238	41.53	9.52	0.0193	Arp 238
LARS04	SDSS-J130728.45+542652.3	0.033	234	40.93	9.93	0.0168	
LARS05	SDSS J135950.92+572622.9	0.034	333	41.36	10.01	0.0099	Mrk 1486
LARS06	SDSS-J154544.52+441551.8	0.034	455	40.56	9.20	0.0164	KISSR 2019
LARS07	SDSS-J131603.91+292254.0	0.038	423	41.50	9.75	0.0090	IRAS 13136+2938
LARS08	SDSS-J125013.50+073441.5	0.038	167	40.78	10.15	0.0288	
LARS09	SDSS-J082354.96+280621.6	0.047	505	41.81	10.46	0.0275	IRAS 08208+2816 ^a
LARS10	SDSS-J130141.52+292252.8	0.057	99	41.15	9.74	0.0101	Mrk 0061
LARS11	SDSS-J140347.22+062812.1	0.084	105	41.54	10.70	0.0216	
LARS12	SDSS J093813.44+542824.9	0.102	408	42.11	10.53	0.0154	LEDA 27453
LARS13	SDSS-J015028.39+130858.4	0.147	201	42.07	10.60	0.0619	IRAS 01477+1254
LARS14	SDSS-J092600.41+442736.1	0.181	578	42.21	10.69	0.0161	
ELARS01	SDSS-J161140.81+522727.0	0.029	215	41.68	10.08	0.0172	NGC 6090
ELARS02	SDSS-J132109.07+590605.3	0.043	92	41.05	10.03	0.0091	Mrk 65
ELARS03	SDSS-J114511.42+614230.6	0.035	65	40.99	10.17	0.0186	UGC 06727
ELARS04	SDSS-J172823.84+573243.4	0.029	103	41.06	10.08	0.0333	NGC 6387
ELARS05	SDSS-J110501.98+594103.5	0.034	41	40.95	9.986	0.0062	SBS 1102+599A
ELARS06	SDSS-J115840.58+645753.0	0.034	47	40.34	9.680	0.0132	
ELARS07	SDSS-J101242.97+613302.8	0.035	268	40.92	9.595	0.0105	
ELARS08	SDSS-J103020.91+611549.3	0.031	48	40.49	9.568	0.0088	
ELARS09	SDSS-J132734.70+664516.6	0.030	94	40.68	9.563	0.0126	
ELARS10	SDSS-J110504.41+593957.3	0.033	75	40.66	9.556	0.0062	SBS 1102+599B
ELARS11	SDSS-J092715.48+583654.4	0.030	58	40.55	9.507	0.0300	MRK 1417
ELARS12	SDSS-J130607.16+591302.4	0.032	46	40.57	9.494	0.0136	SBS 1304+594
ELARS13	SDSS-J105100.65+655940.5	0.032	125	40.85	9.468	0.0103	VII Zw 348
ELARS14	SDSS-J112722.07+604454.1	0.033	82	40.58	9.367	0.0103	SBS 1124+610
ELARS15	SDSS-J134437.82+611424.3	0.035	54	40.44	9.391	0.0148	MCG +10-20-017
ELARS16	SDSS-J135209.13+560631.4	0.035	64	40.24	9.333	0.0091	
ELARS17	SDSS-J102656.29+584941.6	0.031	44	40.19	9.243	0.0061	
ELARS18	SDSS-J152053.59+571122.1	0.029	59	39.93	9.029	0.0105	
ELARS19	SDSS-J120506.35+563330.9	0.031	133	40.30	9.028	0.0131	
ELARS20	SDSS-J133858.25+614957.6	0.031	73	40.34	9.021	0.0156	
ELARS21	SDSS-J141911.37+654946.3	0.033	61	39.82	9.005	0.0110	
ELARS22	SDSS-J170912.73+604950.0	0.047	153	41.10	10.09	0.0213	SBS 1708+608
ELARS23	SDSS-J144827.20+630210.4	0.051	49	40.79	10.08	0.0179	
ELARS24	SDSS-J144305.31+611838.6	0.048	83	41.51	9.996	0.0193	
ELARS25	SDSS-J101201.93+603720.3	0.045	56	40.48	9.833	0.0100	KUG 1008+608
ELARS26	SDSS-J115241.69+661827.2	0.046	43	40.50	9.693	0.0100	
ELARS27	SDSS-J150247.62+622018.9	0.045	47	40.32	9.734	0.0106	
ELARS28	SDSS-J115218.74+585657.0	0.046	131	40.86	9.710	0.0255	
Tol1214	—	0.026 ^b	1644 ^c	40.74	9.008	0.0555	Tololo 1214-277
Tol1247	—	0.049 ^d	530 ^e	42.44	10.36	0.0750	Tololo 1247-232
J1156	SDSS-J115630.63+500822.1	0.236	323	42.36	11.05	0.0187	

NOTE—(3) SDSS spectroscopic redshift (DR8). (4–5) SDSS (DR8). (6) GALEX FUV. $L_{FUV} = \lambda \times L_{\lambda}/L_{\odot}$ at $\lambda = 1524/(1+z)$ \AA . (6) Galactic extinction from the Infrared Science Archive, NASA/IPAC (DOI:10.26131/IRSA537) and (Schlafly & Finkbeiner 2011)

^a Data from SDSS (DR12)

^b Fricke et al. (2001)

^c Guseva et al. (2011)

^d Puschnig et al. (2017)

^e Terlevich et al. (1991)

post-flash was used to limit the effect of charge transfer efficiency (CTE) losses. The typical exposure time for the optical continuum filters was 2×400 s. The choice of using only two dithers was motivated by data transfer limitations when packing observations in multiple filters into a single HST orbit. It should be noted that this limits what pixel scale can be achieved when drizzling the data, and how well cosmic rays are rejected (see Section 2.4). Given that the individual galaxies are at different redshifts the narrow-band filters used to capture $H\alpha$ and $H\beta$ photons vary. When possible we used UVIS narrow-band filters, but for some of the targets (the higher redshift galaxies in particular) ACS/WCS ramp filters were used instead. The typical exposure time in $H\alpha$ is 2×400 s., and 2×600 s. in $H\beta$.

Most of the galaxies are at similar redshift, which means that the cosmological surface brightness dimming is a small effect. The necessary exposure times are thus very similar despite a quite large range in distances. However, three of the targets (LARS 13, 14, and J1156) are at significantly higher redshift. For these galaxies the exposure times were scaled up to account for part of the surface brightness dimming, but the rest-frame depth reached is somewhat reduced.

2.4. Data reduction

Basic image reduction (bias and dark current subtraction, flat-fielding, and post-flash subtraction where applicable) was done with the standard HST reduction pipelines, and individual reduced image frames were downloaded from the Mikulski Archive for Space Telescopes (MAST). In Östlin et al. (2014) full-frame CTE correction was done with the stand-alone tool available at the time, and only for the ACS/WFC images. From 2016 full-frame CTE corrected data has been available directly from MAST and we used this corrected data for both WFC3/UVIS and ACS/WFC data (ISR WFC3 2016-002).

The optical observations use only two dithers per filter which has one major consequence for data reduction. The cosmic ray rejection performed during drizzling of the data fails to mask out many of the affected pixels. Before drizzling we thus performed an additional rejection using the LACosmic software (van Dokkum 2001). We implemented the LACosmic routines in a python wrapping script that flags the found pixels in the data quality layer of each individual frame. The flags are then recognized during drizzling and data affected by cosmic rays are excluded. The individual filters were registered and stacked using the standard HST drizzling software (Drizzlepac; Gonzaga et al. 2012) to a common pixel scale of $0.04''/\text{pxl}$. We also produced drizzled weight

maps for each filter that correctly reflect the total noise per pixel (inverse variance maps).

Sky subtraction is normally handled by the drizzle routine, but for the ACS/SBC data this subtraction is not able to fully remove large scale backgrounds. For the FUV filters we thus remove sky from the drizzled frames by estimating an average sky level well outside the galaxy (usually in the corners of the images). In some cases the sky background in the F125LP filter (because of geocoronal [O I] emission, see Section 2.3) varies substantially (by factors up to 10) between exposures, in this case we subtract the sky from each individual frame before drizzling. It should be noted that we perform this background subtraction also for the galaxies that may have $Ly\alpha$ emission to the edge of the chip (discussed further in Section 3.1.3). For the optical images, the sky subtraction done during drizzling is normally sufficient. However, for some of the galaxies the ACS/WFC ramp filters — and the WFC3/UVIS quad filters — show a residual background gradient which may be caused by problems due to reflected background light in the detector. For the frames affected by this we fitted and removed a spatially varying background from each drizzled frame.

The observations in the different filters for each galaxy are done in multiple HST orbits at different times (however, all observations for a given galaxy and filter are observed in the same orbit). Because of this the guide star used is not necessarily the same for all filters which leads to world coordinate system (WCS) offsets of up to $0.5''$ between the drizzled images. Registering images to a common WCS before drizzling using standard techniques (e.g., Drizzlepac TweakReg) does not work for the SBC images. Instead we chose to register the images by using cross-correlation techniques (PYRAF/XREGISTER). The reference image for the registration was the F438W filter (or equivalent). The average registration uncertainty is around 0.2 pixels ($\sim 0.008''$), but never exceeds 0.5 pixels. After registration we also inspect all of the images to make sure that the reduction steps have been successful, and to construct a mask for each galaxy which marks areas not covered by all filters (particularly important for SBC which has a smaller field of view than the optical filters). These masks are then used for the continuum subtraction and photometry. Color composites of the galaxies using the U, B, and I (HST equivalent bands), showing the stellar continuum are shown in Figures 2, 3, 4, 5, and 6.

In order to perform accurate continuum subtraction from pixel-based SED fitting) the effect of the points spread function (PSF) varying between filters needs to

Table 2. SDSS derived properties

ID	$\log(M_*)$	SFR($H\alpha$)	$E(B-V)_{\text{neb}}$	O32	$12 + \log(O/H)$
	(M_\odot)	($M_\odot \text{ yr}^{-1}$)			
(1)	(2)	(3)	(4)	(5)	(6)
LARS01	8.34	2.15	0.149	4.1215 ± 0.0006	8.2182 ± 0.0001
LARS02	8.56	1.17	0.058	4.5481 ± 0.0004	8.2186 ± 0.0040
LARS03	10.4	5.37	0.656	1.3374 ± 0.0001	8.4163 ± 0.00001
LARS04	8.79	2.43	0.116	4.3706 ± 0.0002	8.1787 ± 0.0003
LARS05	8.37	1.90	0.085	6.5808 ± 0.0008	8.0747 ± 0.0004
LARS06	8.47	0.731	0.010	4.9972 ± 0.0009	8.0638 ± 0.0351
LARS07	8.82	7.04	0.235	4.3694 ± 0.0003	8.3396 ± 0.0001
LARS08	9.23	2.61	0.310	1.8424 ± 0.0009	8.5055 ± 0.00003
LARS09	10.1	15.8	0.231	5.9102 ± 0.0003	8.3679 ± 0.00003
LARS10	9.82	3.69	0.237	1.4772 ± 0.0006	8.5049 ± 0.0001
LARS11	10.6	18.5	0.330	0.8637 ± 0.0017	8.4277 ± 0.0004
LARS12	9.37	23.7	0.152	5.6296 ± 0.0004	8.3121 ± 0.0006
LARS13	10.3	16.6	0.298	2.6281 ± 0.0032	8.5019 ± 0.0003
LARS14	9.13	11.5	0.084	8.0942 ± 0.0039	7.9919 ± 0.0416
ELARS01	10.6	10.1	0.446	0.6193 ± 0.0114	8.2278 ± 0.0054
ELARS02	9.67	4.01	0.342	1.3851 ± 0.0371	8.5022 ± 0.0009
ELARS03	10.3	7.91	0.381	0.6950 ± 0.0254	8.3670 ± 0.0056
ELARS04	9.61	6.36	0.277	0.8170 ± 0.0144	8.4838 ± 0.0015
ELARS05	10.4	3.06	0.300	1.3531 ± 0.0520	8.4560 ± 0.0031
ELARS06	9.50	1.37	0.249	0.6497 ± 0.0255	8.4442 ± 0.0047
ELARS07	8.51	1.44	0.131	5.7574 ± 0.1313	8.0152 ± 0.0103
ELARS08	10.0	2.01	0.365	0.3456 ± 0.0266	8.1079 ± 0.0195
ELARS09	8.96	1.56	0.109	2.3410 ± 0.0458	8.3176 ± 0.0069
ELARS10	9.89	2.14	0.536	0.4988 ± 0.0201	8.3688 ± 0.0071
ELARS11	9.50	1.52	0.129	1.1299 ± 0.0262	8.5014 ± 0.0010
ELARS12	10.1	2.07	0.436	0.3831 ± 0.0171	8.2901 ± 0.0091
ELARS13	9.31	2.65	0.154	1.4057 ± 0.0265	8.4589 ± 0.0016
ELARS14	9.13	1.09	0.201	1.4566 ± 0.0340	8.4981 ± 0.0012
ELARS15	9.75	1.48	0.235	1.0751 ± 0.0416	8.4984 ± 0.0017
ELARS16	9.37	0.836	0.205	1.0130 ± 0.0398	8.5064 ± 0.0002
ELARS17	9.57	0.726	0.257	0.7062 ± 0.0369	8.4000 ± 0.0075
ELARS18	8.86	0.330	0.123	1.6726 ± 0.0727	8.4300 ± 0.0076
ELARS19	8.37	0.451	0.164	3.7944 ± 0.0864	8.2358 ± 0.0077
ELARS20	9.44	0.577	0.217	0.5578 ± 0.0186	8.4096 ± 0.0052
ELARS21	8.66	0.323	0.120	2.2992 ± 0.1015	8.3374 ± 0.0159
ELARS22	9.11	4.37	0.108	2.0325 ± 0.0376	8.3930 ± 0.0042
ELARS23	10.1	4.40	0.310	0.5118 ± 0.0210	8.3488 ± 0.0086
ELARS24	10.6	10.0	0.296	0.9139 ± 0.0146	8.4588 ± 0.0018
ELARS25	9.78	2.45	0.150	0.6726 ± 0.0230	8.4685 ± 0.0038
ELARS26	10.1	2.65	0.437	0.5232 ± 0.0358	8.2764 ± 0.0132
ELARS27	9.61	1.34	0.072	0.6335 ± 0.0266	8.4553 ± 0.0051
ELARS28	9.73	4.38	0.211	1.0799 ± 0.0310	8.5035 ± 0.0008
Tol1214	8.90^a	0.298	0.000^b	16.607 ± 0.0421	7.2102 ± 0.0200^c
Tol1247	10.3^a	21.6	0.158^d	3.7224 ± 0.0209	8.3983 ± 0.0239^e
J1156	9.49	36.1	0.130	2.1096 ± 0.0191	8.4451 ± 0.0076

NOTE—(2–3) Total estimates from the SDSS MPA/JHU catalogues (Brinchmann et al. 2004; Salim et al. 2007). (4) Derived using $H\alpha/H\beta$ from SDSS (DR8). (5) $O32 = [O\text{ III}] \lambda 5007\text{\AA} / ([O\text{ II}] \lambda 3727\text{\AA} + [O\text{ II}] \lambda 3729\text{\AA})$ from Runnholm et al. (2020). (6) Derived using $O3N2$ strong line metallicity calibration of Yin et al. (2007) (Runnholm et al. 2020).

^a From HST SED fitting (LaXs)

^b Fricke et al. (2001)

^c based on line fluxes from Guseva et al. (2011)

^d Puschnig et al. (2017)

^e based on line fluxes from Terlevich et al. (1993)

be handled. While the PSF differences in the optical filters are quite small, the PSFs of the SBC filters (among these the Ly α filter) have very extended wings (see, e.g. Hayes et al. 2016, ISR ACS 2016-05) which makes them differ substantially from the optical filters. If PSF matching is performed without including the extended wings, the stellar continuum from the optical filters is under-estimated relative to the FUV filters. When subtracting the continuum from the Ly α filter too little flux will be subtracted in the wings, causing the Ly α surface brightness to be over-estimated in regions of the galaxy not dominated by a strong point-like source. To study low surface brightness Ly α halos it is thus critical to correctly constrain not only the core of the PSF but also the wings, and match the PSFs of all filters to a common reference.

We start by constructing 2D PSF models for all filters and galaxies. For the optical filters we use TINYTIM (Krist et al. 2011) to make models, but for the SBC images these models are not accurate enough. The SBC PSFs were instead constructed by stacking stars observed in the stellar cluster NGC 6681 during calibrations. For each galaxy we then made a maximum width 2D PSF model by normalizing the models for each filter to the same peak flux and then stacking them by maximum pixel value. Because of the non-standard shape of the SBC PSF matching cannot be done with a gaussian-based convolution kernel, which makes this a non-trivial task. Instead we match the images in individual filters to the maximum width model by convolving with a delta-function-based kernel (similar to the technique described in Becker et al. 2012). A detailed description of how we modeled the PSFs for the different cameras and filters, and how we performed PSF matching for the data is given in Appendix B.

In addition to the drizzled science images in each filter, the data reduction pipeline also produces weight frames. We use these weight frames to estimate the noise per pixel in each filter: $\sigma = 1/\sqrt{W}$, with σ denoting the standard deviation map (i.e., noise) and W the weight map. Because of the drizzling the pixel-to-pixel noise in the images is correlated (Fruchter & Hook 2002), but the noise map still represents the best possible estimate of the uncertainty for each individual pixel we can find. Nevertheless, it is important to note that errors on spatially integrated quantities estimated directly from the noise maps will underestimate the true noise. We perform a full Monte Carlo (MC) simulation of the continuum subtraction and photometry, using the noise maps as input (see Section 3.1.2). However, it should be noted that Voronoi binning will create binned noise maps that will underestimate the noise per bin and

that the resulting errors used in the MC are thus still underestimated. Because of the complicated nature of the how the Voronoi variable binning and noise correlations interact we have not tried to rescale the noise, thus the resulting uncertainties are underestimated by factors ranging between ~ 0 (for the maximum 25^2 Voronoi bin-size) to $\sim 40\%$ (for the minimum binsize of 1 pixel). The χ^2 fitting performed by LaXs (see Section 3.1) will be affected by this, with the effect that the fits appear to be slightly worse than they are. The global apertures (and annuli used for surface brightness profiles) are much larger than the maximum bin size and the error estimates for them will thus not be directly affected by the correlated noise.

3. ANALYSIS METHODS

3.1. Ly α continuum subtraction

With the drizzled and PSF-matched images in hand we can perform the pixel SED fitting necessary to obtain emission line maps for Ly α , H α , and H β . In addition to modeling the continuum underneath these lines the fitting software also produces maps of the best-fit parameters (stellar mass, age, and stellar extinction) and derived properties (e.g., nebular extinction, mechanical energy yields, ionizing flux) for the stellar populations and gas in each pixel. The continuum subtraction is done with the Lyman α eXtraction Software, written in `python`. This code was used for the results presented in Hayes et al. (2014) and Östlin et al. (2014), but development of the code has continued since then and we therefore describe the code in detail below. LaXs is run on both un-binned and Voronoi tessellated data but below we will use the term pixel also to describe the individual bins.

3.1.1. The Lyman α eXtraction Software, LaXS

We fit models to the measured continuum using χ^2 minimisation (i.e., weighted least-squares minimisation) on a semi-discrete grid of four parameters.

$$\chi_j^2 = \sum_i \frac{(F_{i,j} - M_i(m_y, m_o, t, E(B - V)))^2}{\sigma_{i,j}^2} \quad (1)$$

For each pixel, denoted by j above, we have measured continuum fluxes ($F_{i,j}$) and associated errors ($\sigma_{i,j}$) from four or five filters, denoted by i with $N = 4$ or 5 . The model fluxes for each of these filters (M_i) are calculated from stellar population models that depend on a number of parameters, some that are varied in the fitting, and some that are not.

The standard models used here are Starburst99 (Leitherer et al. 1999) single stellar population (SSP) templates which use a Kroupa IMF (Kroupa et al. 1993).

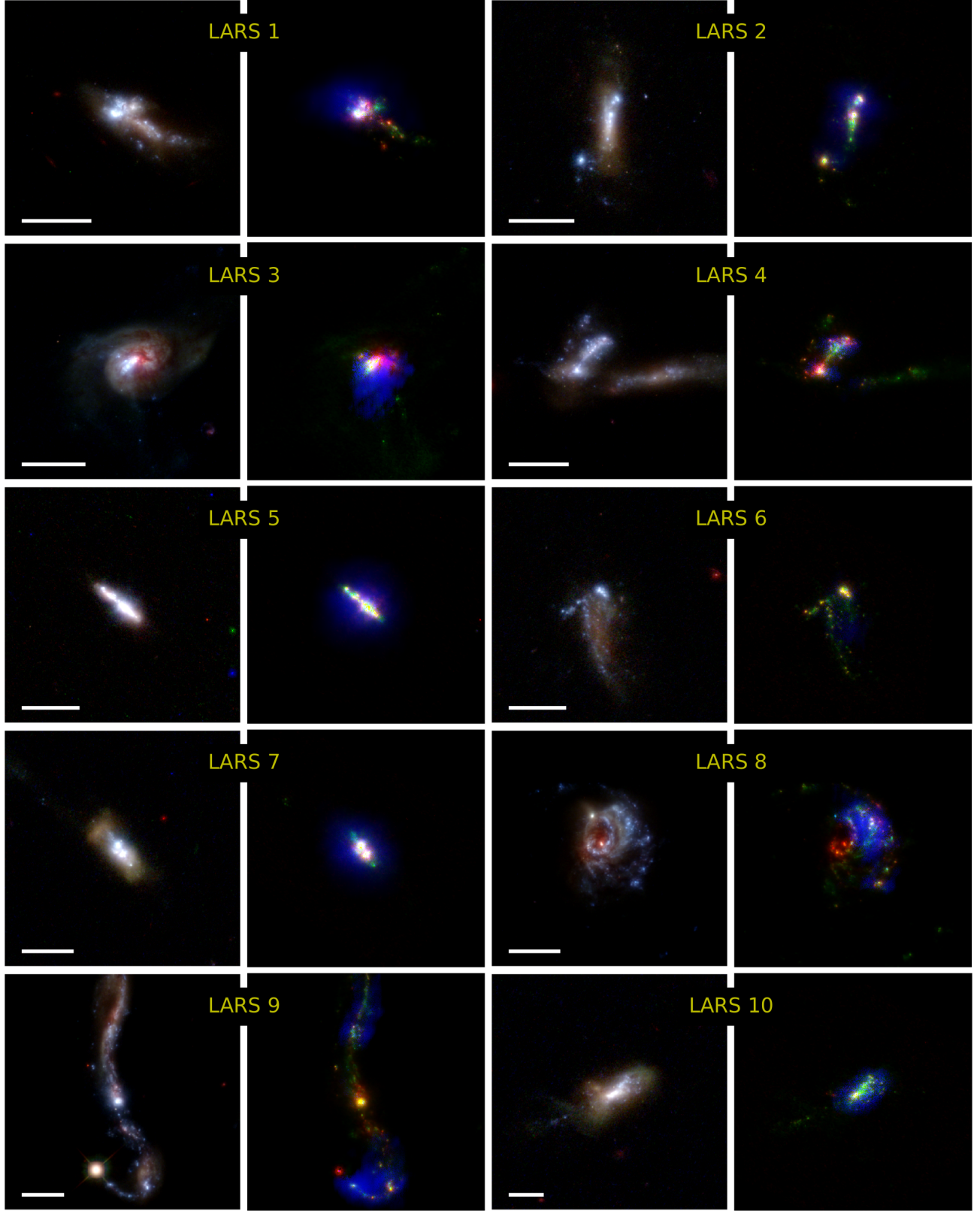


Figure 2. Color composites for the LARS 1–10 galaxies. Two panels are shown for each galaxy with the ID number connecting the corresponding panels. The left sub-panel for each galaxy shows a stellar continuum composite using the HST I, B, and U band images for the RGB channels. The scale bar in these panels has a length of 5 kpc. The right panel for each galaxy shows a composite of red ($H\alpha$), blue ($Ly\alpha$), and green (stellar continuum in the FUV at the wavelength of $Ly\alpha$). The $Ly\alpha$ maps have been adaptively smoothed to enhance the contrast and be able to show the low surface brightness parts of the galaxy.

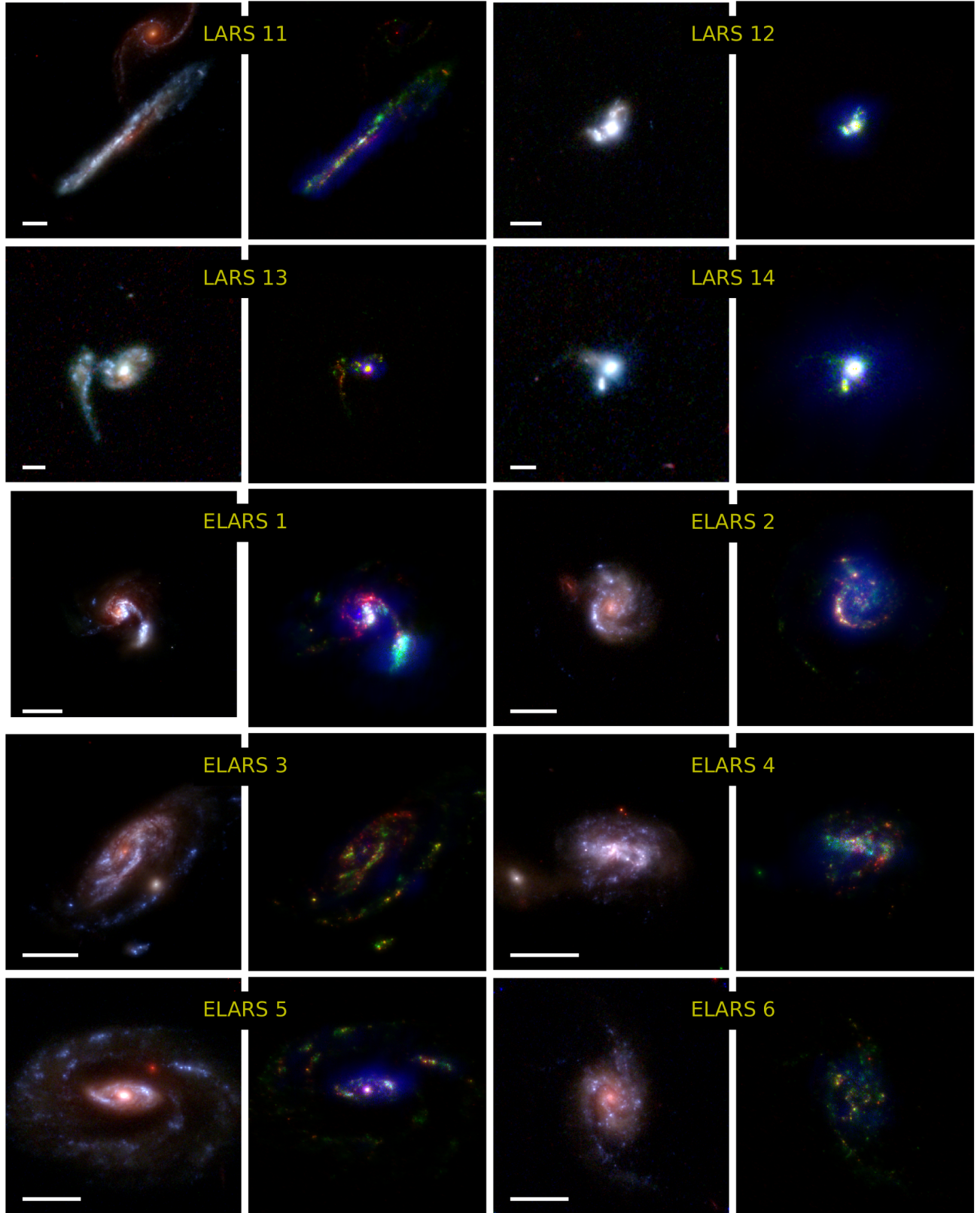


Figure 3. Color composites for the LARS 11–14 and ELARS 1–6 galaxies. See the caption for Figure 2 for details.

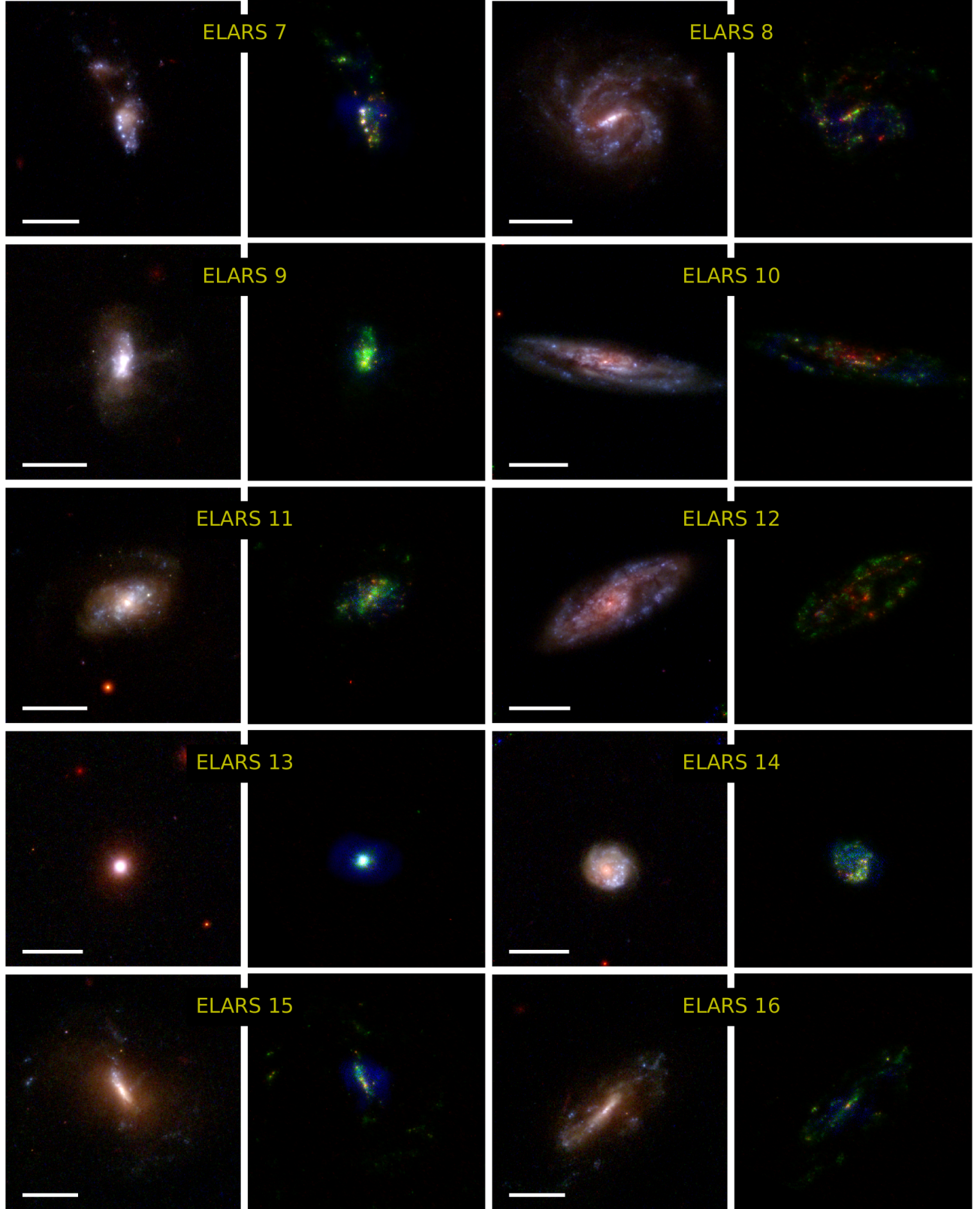


Figure 4. Color composites for the ELARS 7-16 galaxies. See the caption for Figure 2 for details.

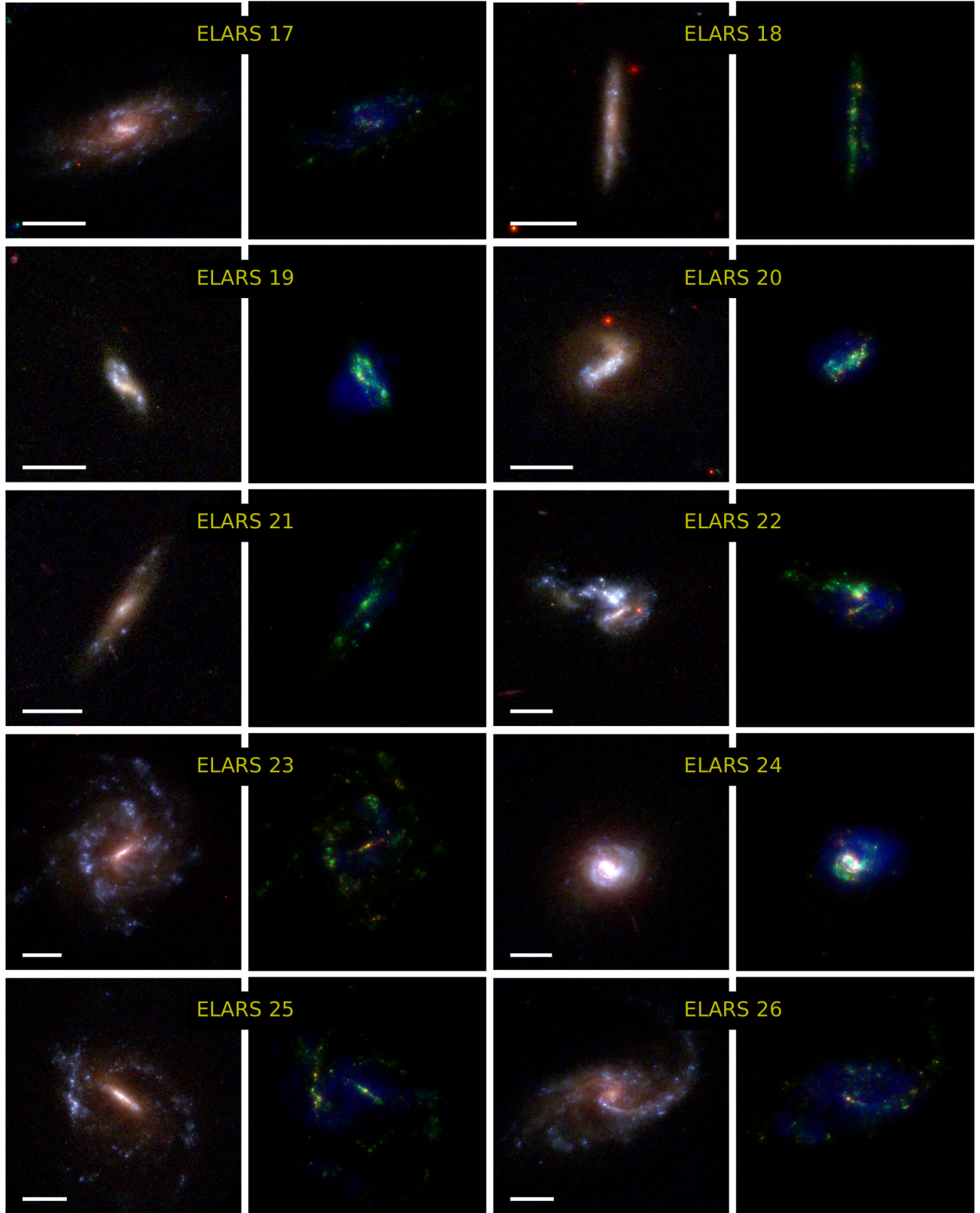


Figure 5. Color composites for the ELARS 17-26 galaxies. See the caption for Figure 2 for details.

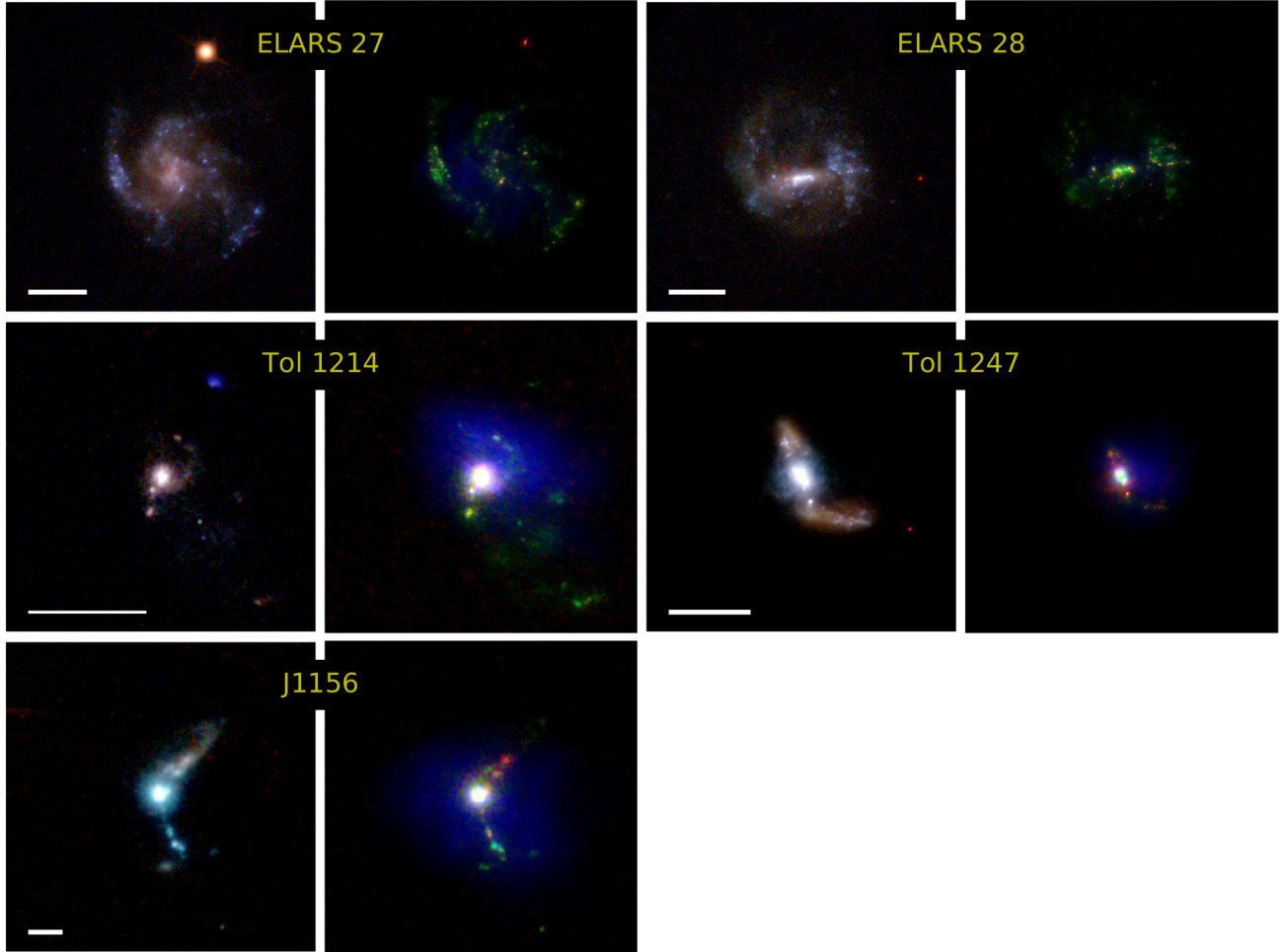


Figure 6. Color composites for the ELARS 27–28, Tol 1214, Tol 1247, and J1156 galaxies. See the caption for Figure 2 for details.

For the model SEDs we use the low resolution ($\Delta\lambda \sim 10$ Å) templates at an assumed metallicity and without nebular continuum. The metallicity used is limited by the available Starburst99 templates and we choose the one closest to the measured SDSS gas metallicities (given in Table 2). We then calculate a grid of template SEDs for a discrete set of stellar ages (t) and extinction ($E(B - V)_s$). We perform testing to find the most appropriate extinction curve for each galaxy (further detailed in Section 3.1.3). The parameter ranges and step sizes can be found in Table 3. The spectral templates for each age step is first reddened using the $E(B - V)_s$ steps and the flux in each observed filter calculated by using `pysynphot` and filter transmission curves for each continuum filter. The resulting template library contains $N_{\text{age}} \times N_{\text{ext}}$ SEDs that are normalized to a stellar mass of $10^6 M_\odot$. The observed fluxes in the Balmer line filters are also corrected for stellar absorption depending on the age of the models. This absorption is calculated using the Starburst99 high resolution stellar templates.

The model SED that is compared to the observations, M_i , is built from two stellar populations of this type, one old with fixed age of 1 Gyr and no extinction, and one young with a varying age and extinction. The final two free parameters in the fitting are the masses for the two components which are continuous parameters. The full model SED is thus:

$$M_i = m_o \times S(t_o, 0) + m_y \times S(t, E(B - V)_s), \quad (2)$$

where m_o and m_y are the old and young population masses, respectively, in units of $10^6 M_\odot$, $S(t, E(B - V))$ is the individual SED template for a given age and extinction, and t_o is the age of the old stellar population.

The minimisation is then performed by calculating the χ^2 for each SED model (each $\{t, E(B - V)_s\}$ pair) where we also solve a linear least squares problem to get the optimum normalisation (i.e., stellar masses). The best-fit stellar masses are thus not restricted to a discrete grid. The code is parallelized using the python package SCOOP¹ (Hold-Geoffroy et al. 2014), which — due to each pixel being independent from another — offers a speedup in execution time close to the number of threads available. The initial best-fitting SED model is then selected as the one which minimizes the χ^2 .

From this initial run we use the H α and H β line maps to produce a dust corrected H α map. The nebular continuum and line contribution to all observed continuum filters and pixels is then estimated by scaling the nebular continuum spectrum from Aller (1984) combined

with nebular lines from Anders & Fritze-v. Alvensleben (2003) with this H α map, again using `pysynphot` to calculate the flux in each filter. The resulting nebular continuum fluxes are subtracted from the observed filters and the entire fitting redone. The fraction of nebular continuum to observed flux in H α -detected regions range from $\sim 1\%$ in the FUV to $\sim 10\%$ in the red optical filter, but for the brightest line emitting regions (and particularly in the galaxies with highest specific SFR) the nebular contribution can be even higher. By forcing the nebular continuum to scale with the dust corrected H α this method provides the most secure determination of nebular continuum for the limited wavelength range. Furthermore, by virtue of directly observing both H α and H β we can treat the nebular continuum as a semi-independent quantity that does not have to be directly determined from the stellar continuum fitting (but note that the H α + H β continuum does come from the fitting).

3.1.2. Statistical error estimates from Monte Carlo simulations

To investigate the statistical errors of the continuum subtracted emission line maps (and the SED fit parameter maps) we perform Monte Carlo simulations using 100 realisations. The input data for each of these (fluxes in all filters and pixels) are generated from a Gaussian distribution with a standard deviation from the noise maps. LaXs is then run for each of these realisations and produces cubes of maps (containing the full output of all the 100 Monte Carlo realisations), along with maps of standard deviation, skewness and other statistical diagnostics. As previously mentioned, the continuum subtraction is computationally expensive, which means that we can only estimate statistical uncertainties for the binned maps, and that the number of Monte Carlo realisations that can be used is limited. However, tests on individual galaxies show that increasing the number of realisations to 1000 does not change the estimated uncertainties significantly. The full Monte Carlo cubes are used to estimate uncertainties in all integrated quantities presented in this paper (see Sections 4.2 and 5).

3.1.3. Systematic error estimates

In addition to statistical errors the continuum subtraction will also suffer from systematic uncertainties which originate in the assumptions made when building the SED templates. In addition to the four free parameters, there are five major fixed parameters (or assumptions) that go into the modeling. These are star formation histories (SFHs) for the two populations, stellar attenu-

¹ <https://github.com/soravux/scoop>

Table 3. LaXs parameters

Type	Parameter	Range	Steps/# tests	Uncertainty, Ly α /FUV
(1)	(2)	(3)	(4)	(5)
Free	m_o	> 0	Continuous	N/A
	m_y	> 0	Continuous	N/A
	t	10^6 – 10^{10} yrs	200	N/A
	$E(B - V)$	0–1.0	200	N/A
Fixed	Attenuation	CCM, SMC, Calz. ^a	3	10/1 %
	Z_*	0.001, 0.004, 0.008, 0.020 ^b	2/3	5/0.5 %
	t_o	10^9 – 10^{10} yrs	10	$\ll 1/0.1$ %
	SFH	SSP+SSP, CSF+SSP, SSP+CSF, CSF+CSF	4	$\ll 1/0.1$ %
	SP library	Starburst99, BPASS	2	$\ll 1/0.1$ %

NOTE—(1) The type is either Free, for parameters that are fitted, or Fixed, for the parameters which are kept constant. (3) For the Free parameters this is the number of steps in the fitting grid, for the Fixed parameters it is the number of tests performed on the systematic uncertainties. (5) This is the standard deviation of the total flux in the high-SNR region for Ly α and the Ly α continuum. We have not explored the systematic uncertainties on using a particular range for the free parameters and they are thus listed as not available. Statistical uncertainties of the free parameters are available from the Monte Carlo runs.

^a CCM — Cardelli et al. (1989), SMC — Prevot et al. (1984), Calz. — Calzetti et al. (2000).

^b The stellar metallicities tested are given by the available stellar population spectra in Starburst 99. For most galaxies we test three different metallicities, the nominal one (the closest match between Starburst 99 models and SDSS gas metallicities), and the ones just below and above.

ation law, age of the old stellar population, metallicity, and stellar population template library.

We estimate the systematic uncertainties from these five fixed parameters by running LaXs in a high signal-to-noise region in each galaxy ($\text{SNR} > 10$ in all filters). We vary each of these parameters on a grid while keeping all the other parameters fixed. In Table 3 we show the test ranges. Old stellar population age (t_o) can be chosen freely but only ages that are older than the young population component are tested. It should be noted that because the UV brightest parts of the galaxies are used as test regions the old population age assumption will have very little effect on the output, but given that we are interested in the FUV and Ly α systematic uncertainties this is the chosen method. The nominal SFHs used are two single stellar populations (burst models, SSPs) for both the young (with varying age) and old populations. We also test combinations of a burst model and a constant star formation (CSF) model. The extinction curves tested are CCM (Cardelli et al. 1989), SMC (Prevot et al. 1984), and Calzetti (Calzetti et al. 2000).

The resulting uncertainties are reported in Table 3, where the numbers given are the relative standard deviations (i.e., the standard deviation divided by the nominal case fluxes), averaged over the full sample, of the total FUV and Ly α flux in the high SNR region for the different assumed cases. We find that the assumption giving rise to the highest systematic uncertainty is the choice of extinction curve, which has an associated uncertainty of $\sim 10\%$ and $\sim 1\%$ for Ly α and the modeled

FUV continuum, respectively. The assumed metallicity is the second most important assumption with associated Ly α /FUV uncertainties of $\sim 5\%$ and $\sim 0.5\%$. It should be noted that this error is a conservative upper limit, given that the metallicity grid is very sparse and that we have a robust metallicity determination from the SDSS spectroscopy. Of course, this case could also be interpreted as testing the effects of metallicity gradients within the galaxies on the continuum subtraction. The remaining fixed parameters show much smaller Ly α systematic uncertainties ($\ll 1\%$).

The systematic uncertainty tests are also used to choose the extinction curve to use for each galaxy. For each galaxy, the results for the three curves are compared by co-adding the best-fit χ^2 inside the high SNR region in each case. We then do a simple model selection, choosing the attenuation law that has the lowest co-added χ^2 .

For the faintest levels of Ly α emission there is an additional systematic error resulting from the subtraction of geocoronal emission in the F125LP filter (see Section 2.4). For galaxies with wide-spread Ly α emission that fills the SBC chip the estimated background will thus include Ly α , which causes our maps to systematically underestimate the flux to an uncertain degree. However, comparing the removed background to average levels of geocoronal emission (using the ACS/SBC exposure time calculation tool and assuming a low level of geocoronal contamination) shows that geocoronal [O I] emission is dominating the background for most of the

galaxies (31 out of 45). The remaining 14 galaxies have larger (and unknown) systematic uncertainties on $\text{Ly}\alpha$ luminosities, $W_{\text{Ly}\alpha}$, and f_{esc} ; and have been marked in Table 5. However, it should be noted that inspecting the individual raw SBC data frames shows that most of these images have a flat background that varies significantly from frame to frame, which would not be the case for true $\text{Ly}\alpha$ emission from the galaxy. Three of the galaxies (LARS04, ELARS04, and ELARS08) are large, have a subtracted background significantly higher than the ETC estimate, and do not show any variation in the background. These three galaxies could thus suffer from substantial oversubtraction of $\text{Ly}\alpha$. Assuming that 100%/10% of the subtracted background is $\text{Ly}\alpha$ emission for these three galaxies results in the $\text{Ly}\alpha$ fluxes (as well as $W_{\text{Ly}\alpha}$ and f_{esc}) being underestimated by factors 2.43/1.14, 1.86/1.09, and 3.94/1.29 for LARS04, ELARS04, and ELARS08, respectively. More details on how the unknown background affects size and $\text{Ly}\alpha$ distribution measurements in galaxies is given in [Rasekh et al. \(2022\)](#). Furthermore, the uncertainty of the removed background is also a source of systematic error but is negligible compared to the statistical errors in the binned maps.

3.2. Photometry and size measurements

We measure the fluxes in the $\text{Ly}\alpha$, $\text{H}\alpha$, and FUV maps, as well as in some of the parameter maps output from LaXs (young population stellar mass, young population stellar age, $E(B - V)_s$). The parameter maps do strictly speaking not contain fluxes, but in the following we will refer to them as such to facilitate the description. All of the measurements are done on the Voronoi binned maps. To define the regions used for the surface brightness profile (or local estimates of the parameters above) we use two different methods.

3.2.1. Circular photometry

The first method is to use circular annuli centered on the brightest pixel in the FUV map. The largest radii for this estimate is given by the largest possible circle that can be fit within the field-of-view (also using the mask described in 2.4), and the smallest radius is 0.5 kpc. The number of bins is set to 30 which is a good compromise between SNR per bin and resolution. For the most distant galaxies (LARS13, LARS14, and J1156) we use logarithmic spacing of the bins, while for the rest of the galaxies a linear spacing is used. We have varied the number of bins (between 25 and 35 bins) to check the systematic errors on sizes and other spatial measurements, but the changes are small. Using a significantly smaller number of bins will of course increase

the SNR per bin greatly, but this comes at the cost of not being able to characterize the spatial variation.

With the bins defined we use the python package `photutils` to measure fluxes in the annuli of all maps. The measured fluxes are all converted into luminosities using the redshifts from SDSS (see Table 1). We compute rest frame surface brightness for $\text{Ly}\alpha$, $\text{H}\alpha$, and FUV in each bin by dividing the measured luminosity by the annulus area. For the surface brightness profiles the radius associated to each bin is the radius that divides the annulus into two equal areas ($r = \sqrt{r_{\text{inner}}^2 + r_{\text{outer}}^2}/2$). For the measurements in the stellar age and $E(B - V)_s$ maps we use luminosity weighted (from the FUV images) averages to make sure that low-SNR Voronoi bins are down-weighted. Note that this weighting scheme means that there is a bias towards lower average ages and extinction.

We also compute curves (annulus and aperture) for derived quantities $W_{\text{Ly}\alpha}$, $\text{Ly}\alpha/\text{H}\alpha$, $E(B - V)_n$, and f_{esc} . Nebular extinction is calculated assuming an intrinsic $\text{H}\alpha/\text{H}\beta$ ratio of 2.86 (case B recombination, $T = 10^4 \text{K}$, $n_e = 100 \text{cm}^{-3}$), and using the [Cardelli et al. \(1989\)](#), hereafter CCM) extinction law. The escape fraction is calculated by assuming an intrinsic $\text{Ly}\alpha/\text{H}\alpha$ ratio of 8.7 ([Henry et al. 2015](#), and references therein) and using the measured $E(B - V)_n$ for the same region:

$$f_{\text{esc}} = \frac{F_{\text{Ly}\alpha}}{8.7 F_{\text{H}\alpha} \cdot 10^{-0.4k(\text{H}\alpha)E(B - V)_n}}, \quad (3)$$

where $k(\text{H}\alpha)$ is the extinction coefficient at the $\text{H}\alpha$ wavelength. The CCM extinction curve assumes a dust screen model for the nebular emission. Opting to use the attenuation curve of [Calzetti et al. \(2000\)](#) instead for both the calculation and application of $E(B - V)_n$ in the expression above leads to somewhat lower escape fractions. For example, a $\text{H}\alpha/\text{H}\beta$ ratio of ~ 4 (corresponding to a Calzetti $E(B - V)_n$ of 0.29) leads to a factor 1.06 lower escape fraction, but this rises with $\text{H}\alpha/\text{H}\beta$ ratio. The difference is quite small for our galaxy sample and we adopt CCM extinction for all nebular line measurements in this paper. Note that the estimated f_{esc} (or $E(B - V)_n$) does not change if the SMC extinction curve is used because the CCM and SMC curves are very similar at the $\text{H}\alpha$ and $\text{H}\beta$ wavelengths.

For determining the global nebular extinction for the galaxies the $\text{H}\beta$ image limits how large an aperture can be used. Because of the dependence on the $\text{H}\alpha/\text{H}\beta$ ratio of $E(B - V)_n$, including non-detected data points for $\text{H}\beta$ leads to huge errors on the extinction. To obtain a safer estimate of $E(B - V)_n$ we find the radius where the $\text{H}\beta$ SNR drops below one. For calculating cumulative f_{esc} profiles we set the $E(B - V)_n$ outside of this radius to the

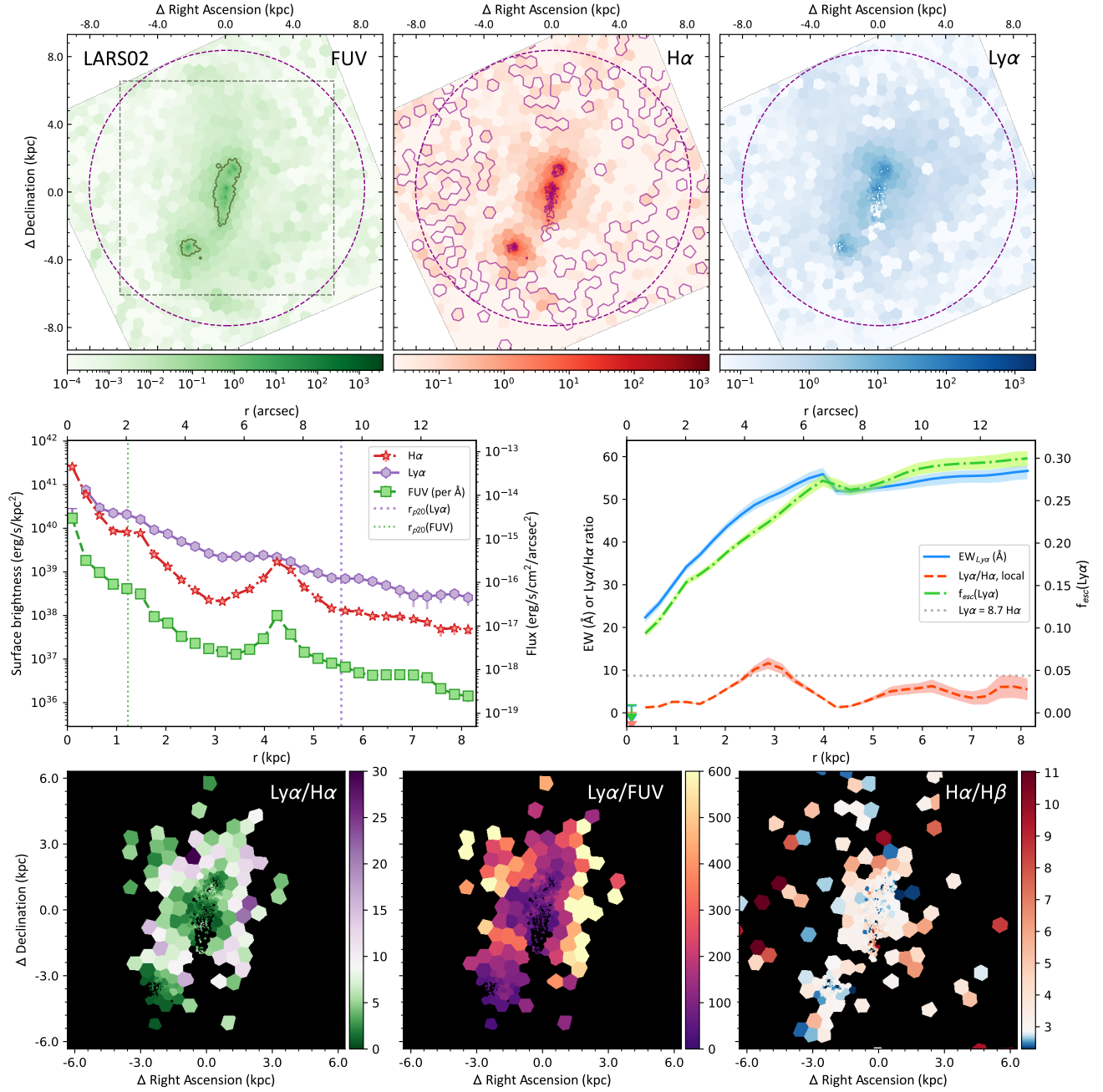


Figure 7. Compilation of measurements on LARS02 (example of a strong Ly α emitter). The maps and profiles are all constructed from Voronoi tessellated data. The top three panels show maps of (from left to right): stellar FUV continuum, H α emission, and Ly α emission. In the FUV map the dashed grey box shows the cut-out box used for the line ratio maps and the dark-green contour shows the Petrosian isophotal limit (corresponding to $r_{p,FUV}$). The purple contours in the H α map shows three logarithmically spaced Ly α levels. The purple dashed circle in the maps indicate the aperture (with radius r_{tot} used to obtain the total estimates of fluxes and other properties). The center of this circle is the central point for the surface brightness profile. The color bar for these panels is in units of 10^{-17} erg/s/cm 2 /Å (for FUV) and erg/s/cm 2 (for line maps). The middle left panel shows surface brightness profiles in FUV, H α , and Ly α . The upper limit symbols are placed at a surface brightness of two times the positive error (estimated from the Monte Carlo generated maps) for each data point. The middle right panel shows line ratio profiles. Note that these are cumulative profiles in all cases but for Ly α /H α . The lower panels contain line ratio maps for a cut-out region, from left to right: Ly α /H α , Ly α /FUV ($W_{Ly\alpha}$), and H α /H β . Bins with SNR < 2 in the input line maps have been masked in the ratio maps and are shown in black. The complete figure set (45 images) is available in the online journal.

value at that radius. For the edge-on galaxy LARS11,

H β is too faint all over the galaxy, and we cannot obtain

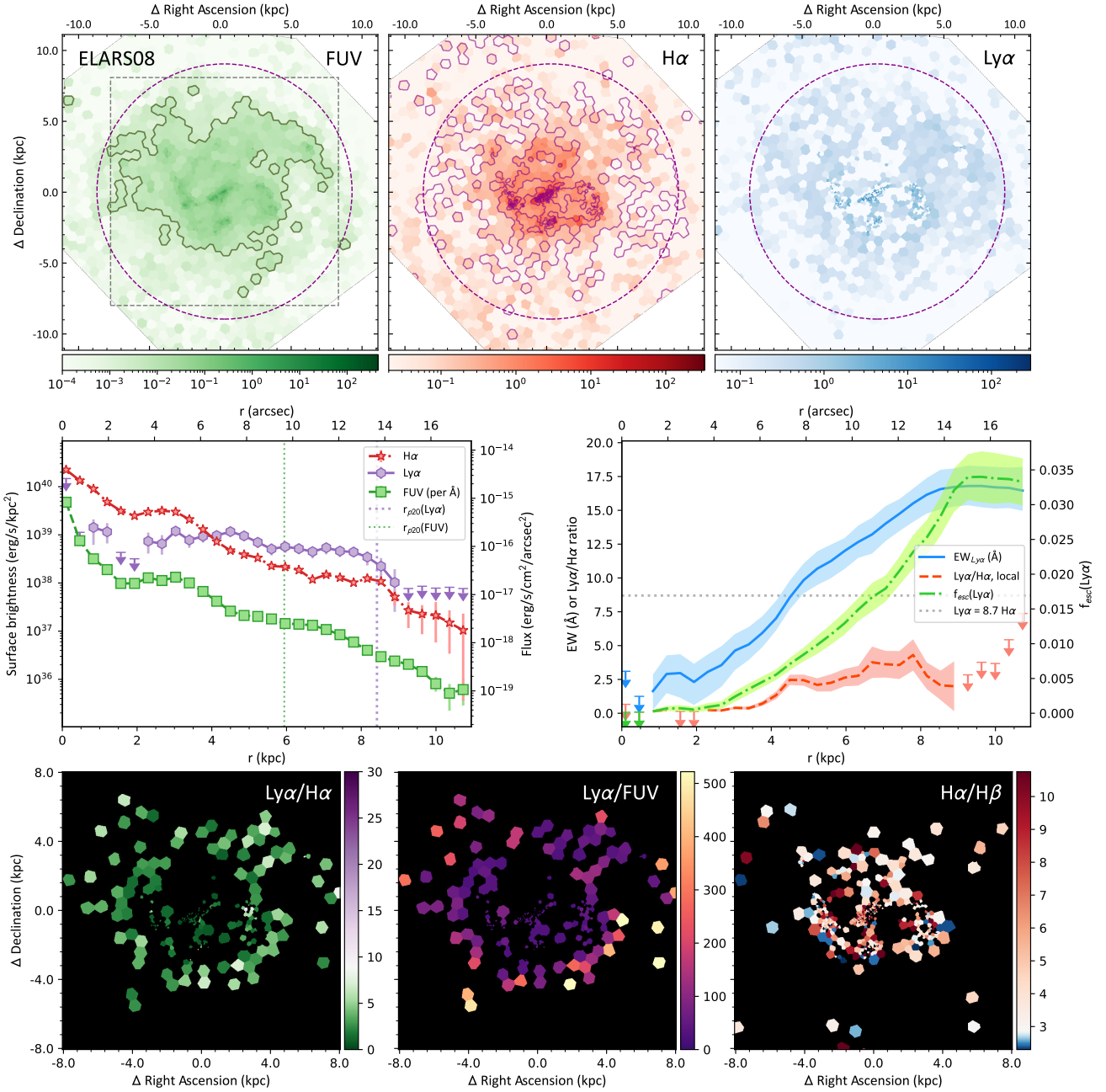


Figure 8. Compilation of measurements on ELARS08 (example of an intermediate $\text{Ly}\alpha$ emitter). A description of the elements in this figure is given in Figure 7. The complete figure set (45 images) is available in the online journal.

a meaningful $E(B - V)_n$ from HST imaging. For this galaxy we instead use a constant nebular extinction from SDSS (see Table 1) for all radii.

The local escape fraction (i.e. escape fraction within an annulus) of $\text{Ly}\alpha$ photons is very hard to interpret because of the resonant scattering of the photons. The same applies to $W_{\text{Ly}\alpha}$, although this is a direct ratio of observed quantities and is thus less model-dependent. Hence we do not measure f_{esc} and $W_{\text{Ly}\alpha}$ for each annulus but only for the apertures. However, we do measure

$\text{Ly}\alpha/\text{H}\alpha$ ratios for each annulus which can be used to show where scattered $\text{Ly}\alpha$ dominates.

3.2.2. Isophotal photometry

We also perform isophotal photometry on the binned $\text{Ly}\alpha$, $\text{H}\alpha$, and FUV maps. The number of isophotes used is 30 (variations between 25 and 35 still show little effect on the found size estimates), and we use logarithmic spacing from the maximum flux in the map to the 1σ surface brightness limit. The 1σ limit is computed from the Monte Carlo error simulations for each map using

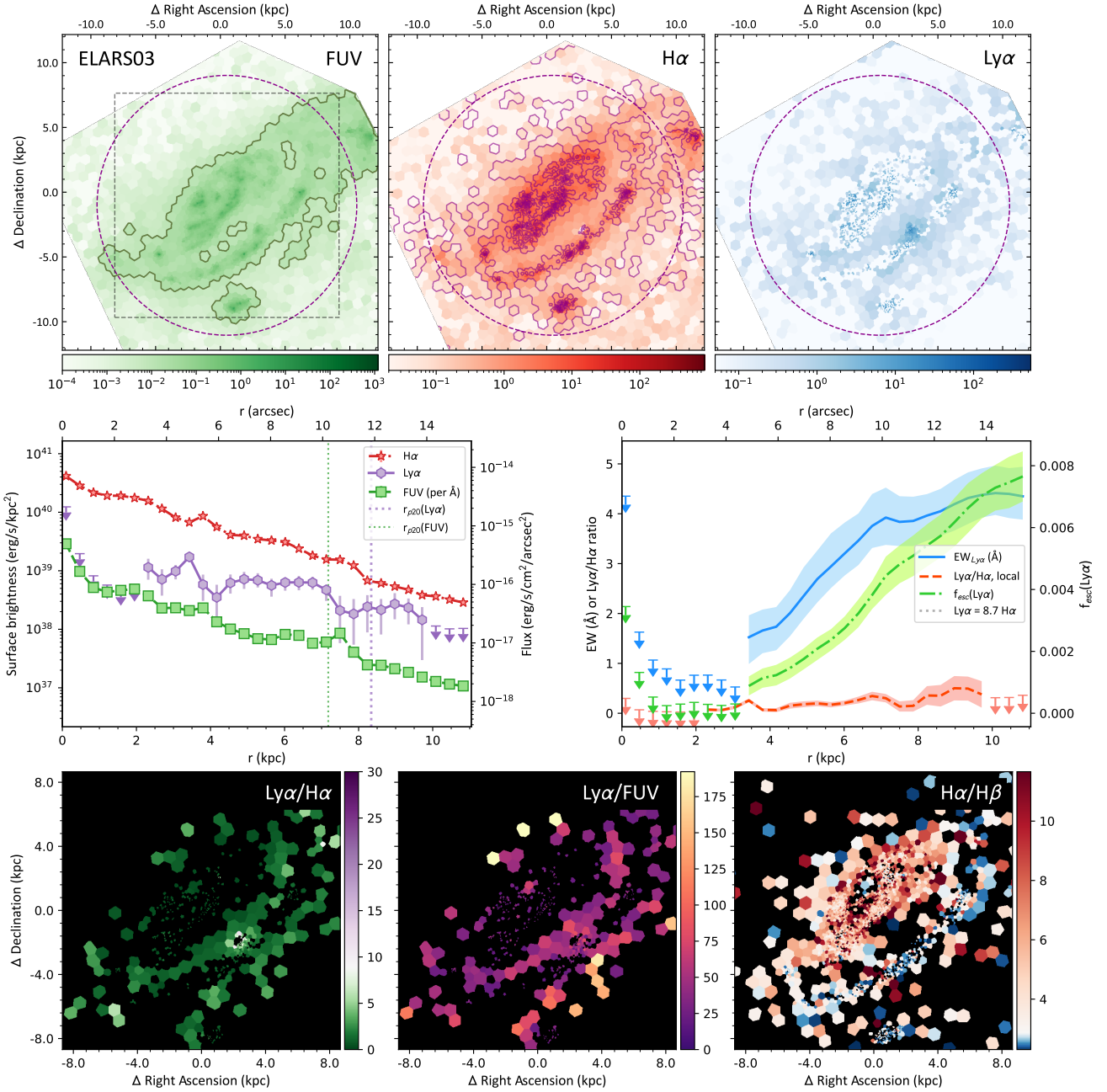


Figure 9. Compilation of measurements on ELARS03 (example of a weak Ly α emitter). A description of the elements in this figure is given in Figure 7. The complete figure set (45 images) is available in the online journal.

a sigma-rejection averaging routine (to find the limiting surface brightness well outside the source).

Each isophotal bin is then treated as a radial bin for surface brightness profiles with the effective radius for the region calculated as the radius of a circle with the same area as the isophotal region (i.e. the area for all pixels with flux higher than the lower limit of the current bin). The isophotal measurements are used to measure the Petrosian radii in the maps, but are otherwise not used in this paper.

3.2.3. Size measurements

We measure the sizes of the galaxies in two different ways. Apart from giving information on the spatial extent of the emission, these sizes can also be used to define global apertures. The size measurements for all galaxies are shown in Table 4.

Petrosian radii, r_p : We calculate 20% Petrosian radii (Petrosian 1976) in Ly α , H α , and FUV using the SDSS definition from Blanton et al. (2001). To get

Table 4. Size measurements

ID	r_{tot}	$r_{p,FUV}$	$r_{p,H\alpha}$	$r_{p,Ly\alpha}$
	(kpc)	(kpc)	(kpc)	(kpc)
(1)	(2)	(3)	(4)	(5)
LARS01	≥ 6.70	$1.490^{0.006}_{0.005}$	$1.570^{0.008}_{0.006}$	$3.520^{0.038}_{0.072}$
LARS02	≥ 8.13	$1.230^{0.019}_{0.021}$	$1.620^{0.406}_{0.022}$	$5.560^{0.171}_{0.388}$
LARS03	≥ 7.63	$1.180^{0.097}_{0.054}$	$1.100^{0.004}_{0.004}$	$8.610^{0.197}_{0.346}$
LARS04	3.28	$4.200^{0.056}_{0.063}$	$2.000^{0.021}_{0.017}$	$1.680^{2.502}_{0.174}$
LARS05	≥ 8.37	$1.090^{0.002}_{0.003}$	$1.490^{0.009}_{0.006}$	$3.140^{0.092}_{0.138}$
LARS06	5.45 ^a	$3.660^{0.293}_{0.144}$	$2.630^{0.737}_{0.074}$	$0.540^{0.488}_{0.854}$
LARS07	≥ 7.75	$1.080^{0.008}_{0.011}$	$1.060^{0.005}_{0.004}$	$4.250^{1.186}_{0.130}$
LARS08	≥ 7.45	$5.230^{0.088}_{0.052}$	$4.460^{0.069}_{0.069}$	$10.100^{0.563}_{4.616}$
LARS09	≥ 12.86	$6.840^{0.055}_{0.042}$	$5.590^{0.041}_{0.038}$	$10.740^{0.202}_{0.825}$
LARS10	5.72	$2.770^{0.234}_{0.192}$	$2.680^{0.037}_{0.049}$	≥ 10.960
LARS11	20.22	$9.010^{0.160}_{0.069}$	$8.770^{0.050}_{0.044}$	$19.170^{6.353}_{6.154}$
LARS12	19.39	$2.000^{0.009}_{0.006}$	$2.520^{0.035}_{0.027}$	$5.720^{0.434}_{0.333}$
LARS13	≥ 26.59	$0.800^{0.172}_{0.048}$	$7.190^{0.016}_{0.017}$	$28.050^{4.534}_{7.637}$
LARS14	≥ 37.62	$0.930^{0.010}_{0.018}$	$2.370^{0.012}_{0.010}$	$4.340^{0.270}_{0.607}$
ELARS01	≥ 6.85	$1.530^{0.004}_{0.004}$	$2.510^{0.017}_{0.023}$	$2.070^{0.061}_{0.054}$
ELARS02	7.40	$4.190^{0.018}_{0.022}$	$3.310^{0.051}_{0.065}$	$4.060^{0.313}_{0.337}$
ELARS03	10.03	$7.180^{0.035}_{0.046}$	$6.660^{0.020}_{0.023}$	$8.340^{0.276}_{0.334}$
ELARS04	≥ 9.65	$3.170^{0.017}_{0.012}$	$3.000^{0.007}_{0.008}$	$7.430^{0.082}_{0.123}$
ELARS05	≥ 10.74	$8.280^{0.149}_{0.134}$	$8.600^{0.000}_{0.001}$	$8.850^{0.129}_{0.079}$
ELARS06	9.08	$5.360^{0.179}_{0.167}$	$6.960^{0.120}_{0.198}$	$9.120^{0.105}_{0.303}$
ELARS07	10.23	$3.700^{0.104}_{0.121}$	$0.430^{0.021}_{0.019}$	$8.050^{0.913}_{3.982}$
ELARS08	9.00	$5.940^{0.095}_{0.161}$	$7.660^{0.033}_{0.031}$	$8.420^{0.506}_{0.386}$
ELARS09	5.63	$1.390^{0.014}_{0.013}$	$1.360^{0.020}_{0.015}$	$7.270^{0.440}_{0.135}$
ELARS10	≥ 8.59	≥ 9.340	$3.720^{0.020}_{0.020}$	$8.860^{3.757}_{0.270}$
ELARS11	5.52	$2.770^{0.053}_{0.017}$	$2.650^{0.011}_{0.013}$	$6.530^{0.546}_{0.285}$
ELARS12	6.28	$4.100^{0.170}_{0.069}$	$4.140^{0.005}_{0.003}$	$6.870^{0.638}_{0.133}$
ELARS13	3.40	$0.110^{0.000}_{0.000}$	$0.530^{0.014}_{0.010}$	$0.210^{0.018}_{0.011}$
ELARS14	4.14	$2.080^{0.054}_{0.079}$	$1.750^{0.002}_{0.003}$	≥ 7.280
ELARS15	8.07	≥ 9.460	$8.790^{0.000}_{0.000}$	$8.610^{4.129}_{1.398}$
ELARS16	4.13	$5.180^{1.371}_{0.541}$	$7.300^{0.000}_{0.000}$	$0.280^{1.944}_{0.780}$
ELARS17	7.49	$6.090^{0.000}_{0.000}$	$6.850^{0.000}_{0.000}$	$8.480^{0.121}_{0.267}$
ELARS18	5.77	$2.560^{0.143}_{0.058}$	$6.240^{0.000}_{0.000}$	≥ 6.750
ELARS19	4.33	$1.800^{0.082}_{0.077}$	$6.700^{0.038}_{0.163}$	$7.030^{0.417}_{0.099}$
ELARS20	4.04	$1.890^{0.025}_{0.023}$	$7.510^{0.000}_{0.000}$	≥ 6.400
ELARS21	3.23	$3.360^{0.000}_{0.000}$	$7.220^{0.000}_{0.000}$	≥ 6.660
ELARS22	9.74	$4.090^{0.138}_{0.134}$	$10.100^{0.000}_{0.000}$	$10.230^{0.232}_{1.546}$
ELARS23	12.87	$10.640^{0.298}_{0.207}$	$10.680^{0.071}_{0.090}$	$11.780^{0.406}_{0.219}$
ELARS24	11.05	$2.720^{0.077}_{0.057}$	$2.070^{0.258}_{0.028}$	$5.390^{0.262}_{0.567}$
ELARS25	≥ 12.31	$8.830^{0.415}_{0.270}$	$9.110^{0.000}_{0.000}$	$11.980^{0.356}_{2.611}$
ELARS26	11.87	$8.190^{0.460}_{0.198}$	$14.320^{0.000}_{0.000}$	$11.040^{0.389}_{0.709}$
ELARS27	≥ 8.18	$6.620^{0.150}_{0.214}$	$9.110^{0.000}_{0.000}$	$9.200^{0.336}_{0.230}$
ELARS28	7.38	$6.170^{0.084}_{0.087}$	$9.040^{0.000}_{0.000}$	$9.730^{1.437}_{0.154}$
Tol1214	≥ 5.92	$0.470^{0.007}_{0.008}$	$0.520^{0.013}_{0.010}$	$1.960^{0.805}_{0.070}$
Tol1247	≥ 10.50	$0.690^{0.003}_{0.004}$	$2.460^{0.008}_{0.007}$	$4.560^{0.117}_{0.099}$
J1156	26.64	$1.470^{0.020}_{0.248}$	$5.930^{0.078}_{0.022}$	$26.060^{6.400}_{0.540}$

^a Ly α is undetected in all circular annuli in this galaxy, the radius used for photometry and shown here is the maximum radius to the edge of the chip.

a more precise measurement of the radius we perform spline interpolation on the surface brightness profiles. As mentioned above these radii are calculated using isophotal photometry and are used to compare the size of Ly α emission and FUV stellar continuum of the galaxies, and to estimate specific star formation rates and star formation rate surface densities.

Total Ly α aperture, r_{tot} : Given that Ly α is often more extended than H α and FUV, global apertures based on petrosian radii in those maps fail to capture all of the Ly α emission from the galaxies. Apertures based on the isophotal photometry are problematic to use when based on Ly α , because of Ly α absorbed regions in the galaxies (see Section 4.1). Another option would be to use elliptical apertures which would possibly capture more of the Ly α emission from galaxies with asymmetric Ly α halos. We have performed some tests, but, because of the irregular nature of the Ly α spatial distribution in the galaxies, getting acceptable elliptical annuli requires extensive finetuning of the fitted elliptical isophotes. Also, given that we want to compare Ly α to other flux maps which often show quite different morphology, measurements from elliptical apertures will have have similar systematic uncertainties as circular apertures. We thus conclude that the safest estimate of global Ly α flux is found by using a large circular aperture centered on the FUV brightest pixel as described above.

The radius of this global aperture is defined as the radius where the annulus signal-to-noise ratio (SNR) of Ly α surface brightness drops below 1. If this happens at more than one radii we chose the largest radii where this condition is fulfilled. This condition is necessary because of the patchiness of Ly α emission and the problems with continuum absorption described above. Furthermore, if the Ly α SNR stays above one all the way out to the maximum radius, the total aperture is defined as the circle with this radius. In these cases the total radius is a lower limit to how far out the detectable Ly α extends. Given that the Monte Carlo derived uncertainties are used to derive r_{tot} we cannot estimate errors for this radius.

3.3. Line ratio maps

For the discussion on spatial Ly α properties of the sample we also make Ly α /H α , $W_{Ly\alpha}$, and H α /H β maps for the galaxies. These are created by using the 2D binned line maps from LaXs. None of the used line maps are extinction corrected. By using the Monte Carlo derived uncertainties for each line map we also create masks marking bins where SNR < 2 in any of the involved line maps. These masks are used to indicate

non-detected regions in the line ratio plots below. Note that, because of non-zero extinction, the masked region sometimes extend into the center of the galaxies when $H\beta$ becomes undetected. In this situation we display an upper limit to the ratio using the 1σ error on $H\beta$ in the ratio plots. Further out in the galaxies, both $H\alpha$ and $H\beta$ becomes too faint and the ratio is unconstrained.

4. THE SPATIAL DISTRIBUTION OF $Ly\alpha$ EMISSION, DUST AND STARS

The continuum subtraction code produces line maps for $Ly\alpha$, $H\alpha$, and $H\beta$, along with best fit stellar continuum maps at the respective wavelengths. In addition to the flux maps the code also outputs maps of the best fit parameters (stellar masses, $E(B - V)_s$, and stellar population age). In the following sections we use the map of stellar continuum at $Ly\alpha$ as the nominal FUV image. While the Voronoi tessellated maps yield the most secure representation of line fluxes and stellar population properties (and also include the full error estimate), we also run LaXs on the un-binned data.

For the descriptions of the binned maps we also divide up the galaxies into three sub-samples and define: i) *weak $Ly\alpha$ emitters*, with $W_{Ly\alpha} < 5 \text{ \AA}$; *intermediate $Ly\alpha$ emitters*, with $5 \leq W_{Ly\alpha} \leq 20 \text{ \AA}$; *strong $Ly\alpha$ emitters*, with $W_{Ly\alpha} > 20 \text{ \AA}$. The $W_{Ly\alpha}$ values used here are the global measurements (see Section 5), and the weak $Ly\alpha$ emitters also include net absorbers. With this definition there are 9 weak $Ly\alpha$ emitters among the galaxies (LARS04, LARS06, LARS10, LARS13, ELARS03, ELARS12, ELARS14, ELARS16, ELARS28), 21 intermediate $Ly\alpha$ emitters (LARS08-09, LARS12, ELARS02, ELARS04, ELARS06-11, ELARS15, ELARS17-23, ELARS25, ELARS27), and 15 strong $Ly\alpha$ emitters (LARS01-03, LARS05, LARS07, LARS11, LARS14, ELARS01, ELARS05, ELARS13, ELARS24, ELARS26, Tol 1214, Tol 1247, J1156).

4.1. $Ly\alpha$, $H\alpha$, and FUV color composites

In Figures 2, 3, 4, 5, and 6 we show color composites of $H\alpha$ (red), FUV (green), and $Ly\alpha$ (blue) for all of the galaxies. These composites are constructed from un-binned data, but applying mild smoothing with a bilateral denoising filter (python/scikit-image van der Walt et al. 2014). The smoothing makes it possible to show the extended, but somewhat patchy, $Ly\alpha$ emission together with the more concentrated emission from stars and $H\alpha$. The scaling (arcsinh) and cut-levels for the respective color channels and different galaxies have been chosen to increase contrast. From inspecting these images it is clear that $Ly\alpha$ is almost always more extended than the $H\alpha$ emission and stellar continuum. In many of

the galaxies the central parts are dominated by red and green, indicating that $Ly\alpha$ is weak or even in absorption there. The main limitation of the pseudo-narrowband technique used to isolate the $Ly\alpha$ emission is that it does not resolve emission and absorption of the line. In regions where the FUV continuum is strong and the column density of H I high, absorption may very well dominate the measurement which results in negative $Ly\alpha$ fluxes in the maps. As seen in the color composites (as well as in the binned images and surface brightness profiles) this turns out to happen in many of the galaxies in our sample.

The $Ly\alpha$ -FUV- $H\alpha$ color composites for LARS01-LARS14 differs from the previously published images in Hayes et al. (2013). Most of this comes from the change in calibration of the ACS/SBC instrument, but also from updates to the reduction process and continuum subtraction, and the choice of channel scaling in putting the new images together. We note that the earlier images and measurements were obtained with an incorrect calibration for the SBC and blue UVIS filters². The updated results in this paper thus replaces the earlier measurements (see also Section 5). Because of the arbitrary nature of how the smoothing and scaling was done we do not perform any detailed measurements on these images, but instead work with the binned maps for the following analysis.

4.2. Spatial $Ly\alpha$ properties of the sample.

In this paper we present detailed measurements of surface brightness profiles of the galaxies in the sample, and give an overall description of the profile properties for the different $W_{Ly\alpha}$ groups. An extensive statistical study of the $Ly\alpha$ profiles and how they relate to other properties of the galaxies is given in Rasekh et al. (2022). In the following section we will describe the spatial $Ly\alpha$ properties of the three sub-samples. How the global properties relate to one another is described in Section 5. Figures 7, 8, and 9 show maps of the fluxes and derived quantities, as well as surface brightness profiles of these. These three galaxies are shown as examples of the three sub-sample groups, figures for the full sample are available in the online journal. Surface brightness profiles measured in $Ly\alpha$ and FUV for the full sample are given in Table 8 in Appendix C.

4.2.1. Weak $Ly\alpha$ emitters

This subgroup is characterized by weak and very patchy $Ly\alpha$ emission. The small amounts of emission

² The changes in calibration are documented in ISR ACS 2019-05, and ISR 2021-04

that manages to escape comes out in select regions. The effect of continuum absorption is also strong in these galaxies, the Ly α flux measured in larger apertures tend to be close to zero or even negative. This has the effect that the radial profiles are quite messy, they jump up and down as single spots of emission enters the annuli.

Most of these galaxies are quite dusty (with the exception of LARS04), and from inspecting the H α /H β maps, the regions where Ly α escapes seems to have lower nebular extinctions. The $W_{\text{Ly}\alpha}$ maps are noisy and shows low values all over the galaxies, with the possible exception of ELARS03, which does show somewhat higher $W_{\text{Ly}\alpha}$ on the side inclined towards the observer, and particularly close to a star-forming knot in one of spiral arms. The Ly α /H α maps show a similar picture with values predominantly $\ll 8$. It should be noted that the intrinsic ratios may be larger than this, but obtaining an accurate local extinction corrected Ly α flux is not possible, because of the longer path lengths for the resonantly scattered Ly α photons. We use the non-extinction corrected Ly α /H α maps to signify where in the galaxies Ly α has been scattered away from the production sites. The specific distribution of dust may also cause variations of the Ly α /H α ratios, but unless there are significant dust column densities outside the H α or UV bright region this is unlikely to cause the high Ly α /H α ratios we observe in the outskirts of some of the galaxies from the stronger LAEs. In addition, obtaining dust corrected Ly α /H α maps that cover the full galaxies is not possible, because of low S/N in the H α /H β map.

In general these galaxies also lack Ly α halo emission (meaning emission visible outside the FUV/H α emitting areas), the emission is quite concentrated to small patches close to the UV center of the galaxies. Two of the galaxies (ELARS03 and ELARS28) do have measurable halo emission, and for ELARS03 this might extend outside the field-of-view.

4.2.2. Intermediate Ly α emitters

The intermediate emitters also have patchy Ly α emission, but the emission is stronger (or continuum absorption weaker). Some of these galaxies show quite asymmetric emission when inspecting the Ly α map (ELARS19–21, ELARS23). This is particularly true for the galaxies with a visibly inclined disk, where the emission comes out from the side closest to us (determined from the H α /H β ratio map). Also galaxies without a well-defined disk show very little Ly α emission in the regions with high H α /H β ratio.

Inspection of the surface brightness profiles show that Ly α is more extended than FUV/H α in all but a few cases (exceptions are LARS08, ELARS02, ELARS06,

and ELARS18). The other galaxies have extended Ly α halos, and six of them have emission extending outside the field-of-view. In the inclined disk cases, the emission is more extended in the off-axis direction (which is not visible in the profile plots).

The Ly α /H α ratio is below 8.7 in the galaxies, but higher than for the weak emitter sub-group. The strongest spots of Ly α in some of the galaxies do reach this limit, and are situated outside the FUV emitting part of the galaxies. ELARS04 and 11 shows some annulus regions with Ly α /H α > 8.7 , but with large errors.

4.2.3. Strong Ly α emitters

The strong emitters show Ly α in large portions of the image, although some absorption is visible, in particular in regions with high FUV surface brightness and/or high H α /H β ratio. The spatial distribution of Ly α is mostly symmetric, but in some galaxies there appears to be directions that are unfavored for escape (LARS01, LARS03, LARS11, ELARS01, ELARS24, Tol 1214).

Most of the galaxies in this group have low global $E(B - V)_n$, but, somewhat surprisingly, a few dusty galaxies are also included. Even though $W_{\text{Ly}\alpha}$ is higher than 20 Å globally the escape fractions are very low, indicating that we see Ly α emission from low-dust regions where the relative escape of the photons can be quite high. In these galaxies (LARS03, LARS11, ELARS01, and ELARS24) the Ly α emission shows up in distinct regions that likely indicates channels where the dust content is lower.

The profile plots show that the fraction of Ly α emission coming out in the halo varies among the galaxies. A majority of them (11 out of 15) show Ly α /H α > 8.7 in parts of the image, preferably in the halo, indicating that resonant scattering of the Ly α photons is in full effect. Most (13) also have Ly α emission extending all the way to the edge of the field-of-view.

4.2.4. Escape fraction and equivalent width variations with aperture size

The cumulative escape fraction profiles generally rise as you go further out, but many galaxies in all sub-groups show a dip in the profile. One explanation to this behaviour is strong gradients in the extinction profile (which directly affects the f_{esc} profile), but could also be due to Ly α continuum absorption in off-center regions with strong FUV emission and high H I column densities. The f_{esc} profile shape of these galaxies thus indicates that both direct (with weak resonant scattering) and indirect (via strong scattering) escape takes place in the galaxies.

In twelve of the galaxies we find that the shapes of the f_{esc} and $W_{\text{Ly}\alpha}$ cumulative profile differ from one an-

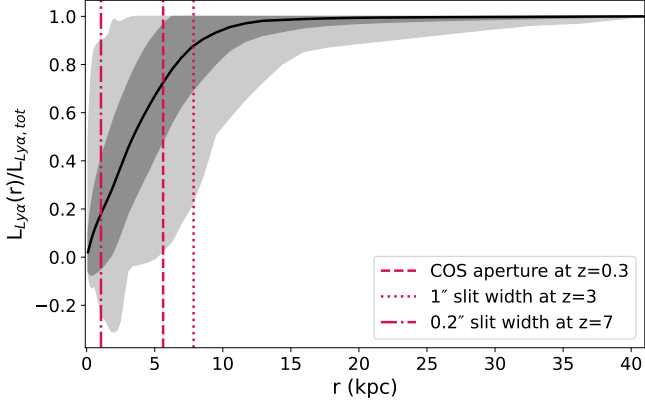


Figure 10. Average growth curve of Ly α luminosity for the galaxies in the sample with $W_{\text{Ly}\alpha} > 0 \text{ \AA}$. The dark grey shaded area shows the standard deviation (capped at a ratio of 1) over the sample at each radius and the light grey shade shows the full envelope of the sample.

other. This is somewhat unexpected given that they both provide a normalized estimate of escaping Ly α . In some of these cases (e.g., LARS01, LARS03) the escape fraction is highest in the center of the galaxies, decreases as the aperture grows bigger, and then starts to increase again further out. This is very different from the $W_{\text{Ly}\alpha}$ cumulative profile in these galaxies that just increases with radius. The cause of this difference lies in that $W_{\text{Ly}\alpha}$ provides an estimate of Ly α escape relative to the non-extinction corrected FUV luminosity. The measured FUV luminosity will thus not give the total budget of ionizing radiation, and will in particular differ from an absolute measure (f_{esc}) in dusty regions of the galaxies. We see this effect in dusty galaxies and in galaxies with strong extinction gradients in the sample. The specific case of high central escape with a sharp drop is likely the effect of choosing the brightest FUV coordinates to be the centrum for the apertures. This point is likely to have low extinction which leads to a high escape fraction. If the extinction then goes up with radius f_{esc} will drop. This effect is strongest in the dusty galaxies that often only have small relatively dust-free regions,

4.3. Average Ly α growth curves

Spectroscopic measurements of the Ly α line using a limited slit or aperture size can potentially miss part of the extended emission. Given the effects of resonant scattering this impacts Ly α much more than the other nebular lines or stellar continuum. With our Ly α imaging data we can follow the spatial emission profile further out and estimate slit losses for an aperture of a given physical size. It should be noted that observations of high redshift LAEs with VLT/MUSE (see Section 5.1) do not suffer from any slit losses given that this

instrument is an integral field unit spectrograph. The same is true for slitless spectroscopy (e.g., HST/WFC3 or JWST NIRCAM/NIRISS grism spectroscopy).

In Figure 10 we show the average growth curve of Ly α luminosity for the galaxies with confirmed global Ly α emission ($W_{\text{Ly}\alpha} > 0 \text{ \AA}$) together with physical sizes for three different spectroscopic slit (or aperture) sizes. Depending on the redshift and angular slit width these physical sizes will vary. The total luminosity used for this plot is measured within the total Ly α aperture described above. It should be noted that many of the galaxies (20/45) have detectable Ly α all the way out to the edge of the detector, which means that the total luminosity is a lower limit. The average $L_{\text{Ly}\alpha}(r)/L_{\text{Ly}\alpha,tot}$ curve thus shows an upper limit to the flux recovered at a given physical aperture size.

We have estimated slit losses (defined as $1 - L_{\text{Ly}\alpha}(r)/L_{\text{Ly}\alpha,tot}$) for three typical cases of Ly α spectroscopy. For these estimates we use the average curve shown in Figure 10 (with the exception of our own sample where we use the individual growth curves). We also provide estimates using infinite aperture Ly α luminosities ($L_{\text{Ly}\alpha,exp}$), obtained by fitting an exponential function for the surface brightness profile in the halo and extrapolating, from Rasekh et al. (2022). These slit loss estimates avoid the problem of Ly α extending outside the detector but suffer from unknown systematic uncertainties due to the assumption of purely exponential halos.

HST/COS aperture: For the data presented in this paper (with an average redshift of 0.05) the COS aperture suffers from quite severe losses. The average aperture loss for COS for our galaxies compared to $L_{\text{Ly}\alpha,tot}$ ($L_{\text{Ly}\alpha,exp}$) is 0.5 ± 0.2 (0.6 ± 0.3), where the uncertainty is the standard deviation for the sample. Inspecting the growth curves of our sample and looking at more distant galaxies at $z \sim 0.3$ (by calculating the physical aperture size at that redshift) we find that COS is able to recover more of the Ly α flux. The average aperture loss is then 0.27 ± 0.23 and 0.40 ± 0.26 for $L_{\text{Ly}\alpha,tot}$ and $L_{\text{Ly}\alpha,exp}$ total flux estimates, respectively.

High redshift LAE observed with a 1''slit: For galaxies at $z = 3.0$ and assuming a typical slit width of 1'' for ground-based multi object spectroscopy (MOS) studies of LAEs we find that the slit loss is 0.12 ± 0.18 and 0.25 ± 0.27 for $L_{\text{Ly}\alpha,tot}$ and $L_{\text{Ly}\alpha,exp}$ total flux estimates, respectively. The slit losses from pure Ly α scattering are not very significant in this case, but the issue could be further compounded by PSF losses which need to be computed assuming an extended source rather than a point source.

Extreme high redshift LAEs observed with

JWST/NIRSPEC: With JWST/NIRSPEC it is now possible to observe extreme redshift LAEs ($z \gtrsim 7$) using the NIRSPEC MOS mode. However, the slit width of a single micro-shutter array (MSA) shutter is very narrow ($0.2''$), which means that slit losses may be very high. Indeed, calculating the average slit loss at $z = 7.0$ within a single MSA shutter we find losses of 0.80 ± 0.21 and 0.82 ± 0.21 for $L_{\text{Ly}\alpha, \text{tot}}$ and $L_{\text{Ly}\alpha, \text{exp}}$ total flux estimates, respectively.

5. GLOBAL MEASUREMENTS OF $\text{Ly}\alpha$ AND OTHER PROPERTIES

Global luminosities and derived quantities are measured within r_{tot} , with three exceptions. The first is $E(B - V)_n$, which uses the smaller aperture size given by $\text{H}\beta$ (see Section 3.2.1). The total $\text{Ly}\alpha$ aperture is sometimes quite small (in particular for weak or non-emitters) and measured masses are therefore underestimated. To obtain total masses for the galaxies we thus re-measure global masses within a circular aperture of size determined from mass growth curves in the same way as for $\text{H}\beta$ (but with a SNR threshold of 1). The HST imaging derived masses are in general much higher than the masses from SDSS spectroscopy/imaging SED fits. This difference come from the apertures used for the HST imaging being much larger than the standard SDSS aperture.

The SFR density and specific SFR is determined within an isophotal region determined from the $\text{H}\alpha$ map with an effective radius of $r_{\text{p}, \text{H}\alpha}$ (given in Table 4). This aperture is in general smaller than the $\text{Ly}\alpha$ total aperture, but provides a much safer estimate of these observables due to large uncertainties in mass and SFR for large apertures. It should be noted that the measurements from the HST $\text{H}\alpha$ observations sometimes show significantly higher SFR than the SDSS measurements given in Table 2. This difference comes from the larger apertures used in our imaging measurements, when comparing measurements for the same aperture size the HST SFR estimates are consistent (within the errors) with the SDSS measurements. For consistency we use the imaging derived masses, extinctions and SFRs throughout this paper.

In addition to the measurements obtained from HST maps we also use SDSS derived values of $12 + \log(O/H)$ and $[\text{O III}] \lambda 5007 / [\text{O II}] \lambda 3727$ ratio (O32) from Runnholm et al. (2020). For the oxygen abundance the strong line N2P calibration (Yin et al. 2007)

is used, which can be estimated for all of the galaxies in the sample. The O32 ratio provides a diagnostic on the overall ionisation state of the nebular gas (e.g., Kewley & Dopita 2002). The luminosities and derived quantities for the full sample are given in Tables 5 and 6.

For the comparisons shown in this section we use the censored Kendall- τ test (Akritas et al. 1995, as implemented in the R package CENKEN) to check for correlations or anti-correlations. The censored test allows the inclusion of upper limits in the calculations, so that also the $\text{Ly}\alpha$ non-detected galaxies can be included. We use limits of $|\tau| > 0.3$ and $p_0 < 0.003$ to signify a strong correlation (or anticorrelation), but also discuss weaker trends.

5.1. The luminosity, equivalent width, and escape fraction of $\text{Ly}\alpha$

We detect global $\text{Ly}\alpha$ emission from 39 out of 45 galaxies at a signal-to-noise ratio of 2 or more (the median ratio for the detected galaxies is ~ 13). Three of the six non-detections are net absorbers and we measure a negative $\text{Ly}\alpha$ flux for them.

The luminosity of $\text{Ly}\alpha$ is expected to scale with FUV luminosity, primarily through the connection to star formation with the production of $\text{Ly}\alpha$ photons. In Figure 11 we show total luminosity of $\text{Ly}\alpha$ versus the FUV luminosity. There is indeed a strong correlation between the two ($\tau = 0.51$, $p_0 = 7.3 \cdot 10^{-7}$), but also substantial scatter. The spread seen here can be explained by the combination of dust extinction and resonant scattering of the $\text{Ly}\alpha$ photons (see Section 6.1). For an individual source this effect makes it hard to use $\text{Ly}\alpha$ observations as a direct probe of star formation. The plot also shows the range of $W_{\text{Ly}\alpha}$ the sample covers, from a few to ~ 100 Å.

Figure 11 also shows the relation between f_{esc} and $W_{\text{Ly}\alpha}$. Given that both of these quantities give $\text{Ly}\alpha$ luminosity normalized with measurements that are directly coupled to the star formation rate they are expected to correlate, which is also what we find ($\tau = 0.55$, $p_0 = 8.3 \cdot 10^{-8}$). However, also this relation shows significant scatter, in particular at low f_{esc} . The main difference between the two is that f_{esc} is an absolute estimate (based on extinction corrected $\text{H}\alpha$) of the fraction of $\text{Ly}\alpha$ photons that escapes the galaxy, while $W_{\text{Ly}\alpha}$ provides a relative estimate of the escape as compared to observed FUV continuum flux. In galaxies where much of the star formation is hidden by dust, the observed $W_{\text{Ly}\alpha}$ can still be quite high because the global aperture measurements are dominated by the non-dusty regions. The extinction corrected $\text{H}\alpha$ does not suffer from this (modulo extinction uncertainties) and thus yields a

Table 5. Global Ly α , H α , and FUV measurements

ID	L_{FUV}	$L_{\text{H}\alpha}$	$L_{\text{Ly}\alpha}$	$W_{\text{Ly}\alpha}$	f_{esc}
	(10^{40} erg/s/cm 2 /Å)	(10^{41} erg/s/cm 2)	(10^{41} erg/s/cm 2)	(Å)	
(1)	(2)	(3)	(4)	(5)	(6)
LARS01	1.978 $^{+0.004}_{-0.004}$	5.126 $^{+0.010}_{-0.014}$	8.345 $^{+0.089}_{-0.089}$	42.195 $^{+0.397}_{-0.458}$	0.134 $^{+0.002}_{-0.002}$
LARS02	0.733 $^{+0.004}_{-0.003}$	1.590 $^{+0.011}_{-0.012}$	4.154 $^{+0.093}_{-0.116}$	56.661 $^{+1.304}_{-1.946}$	0.299 $^{+0.010}_{-0.010}$
LARS03	0.561 $^{+0.003}_{-0.003}$	6.091 $^{+0.025}_{-0.021}$	1.917 $^{+0.076}_{-0.095}$	34.164 $^{+1.348}_{-1.848}$	0.005 $^{+0.000}_{-0.000}$
LARS04 ^a	1.338 $^{+0.002}_{-0.003}$	3.831 $^{+0.009}_{-0.011}$	0.276 $^{+0.062}_{-0.058}$	2.065 $^{+0.467}_{-0.435}$	0.006 $^{+0.001}_{-0.001}$
LARS05	2.613 $^{+0.006}_{-0.005}$	4.254 $^{+0.018}_{-0.013}$	6.516 $^{+0.107}_{-0.107}$	24.935 $^{+0.471}_{-0.467}$	0.126 $^{+0.002}_{-0.002}$
LARS06	0.375 $^{+0.004}_{-0.003}$	0.648 $^{+0.007}_{-0.006}$	≤ 0.089	≤ 2.374	≤ 0.012
LARS07	1.717 $^{+0.006}_{-0.008}$	3.789 $^{+0.016}_{-0.015}$	6.661 $^{+0.132}_{-0.144}$	38.801 $^{+0.935}_{-1.000}$	0.111 $^{+0.002}_{-0.002}$
LARS08	2.316 $^{+0.009}_{-0.016}$	11.072 $^{+0.345}_{-0.124}$	4.017 $^{+0.267}_{-0.193}$	17.345 $^{+1.302}_{-0.915}$	0.006 $^{+0.000}_{-0.000}$
LARS09	5.913 $^{+0.015}_{-0.011}$	18.962 $^{+0.035}_{-0.027}$	5.810 $^{+0.284}_{-0.272}$	9.827 $^{+0.477}_{-0.474}$	0.016 $^{+0.001}_{-0.001}$
LARS10	1.120 $^{+0.005}_{-0.007}$	2.005 $^{+0.012}_{-0.022}$	≤ 0.235	≤ 2.100	≤ 0.003
LARS11	8.725 $^{+0.051}_{-0.055}$	9.929 $^{+0.113}_{-0.079}$	17.899 $^{+1.304}_{-0.973}$	20.515 $^{+0.976}_{-0.710}$	0.065 $^{+0.009}_{-0.009}$
LARS12	8.502 $^{+0.043}_{-0.037}$	13.904 $^{+0.144}_{-0.092}$	15.396 $^{+0.896}_{-0.758}$	18.108 $^{+1.045}_{-1.041}$	0.027 $^{+0.001}_{-0.001}$
LARS13	11.956 $^{+0.229}_{-0.273}$	20.978 $^{+0.084}_{-0.074}$	≤ 2.989	≤ 1.774	≤ 0.004
LARS14	11.358 $^{+0.194}_{-0.129}$	18.908 $^{+0.239}_{-0.238}$	55.602 $^{+1.914}_{-1.982}$	48.955 $^{+2.281}_{-2.102}$	0.263 $^{+0.010}_{-0.010}$
ELARS01	2.443 $^{+0.003}_{-0.003}$	13.134 $^{+0.016}_{-0.017}$	5.169 $^{+0.063}_{-0.064}$	21.156 $^{+0.288}_{-0.297}$	0.012 $^{+0.000}_{-0.000}$
ELARS02	2.660 $^{+0.005}_{-0.004}$	6.188 $^{+0.036}_{-0.035}$	3.311 $^{+0.116}_{-0.082}$	12.444 $^{+0.450}_{-0.327}$	0.061 $^{+0.002}_{-0.002}$
ELARS03 ^a	2.779 $^{+0.008}_{-0.007}$	10.127 $^{+0.032}_{-0.025}$	1.227 $^{+0.145}_{-0.119}$	4.414 $^{+0.535}_{-0.428}$	0.005 $^{+0.001}_{-0.001}$
ELARS04	2.587 $^{+0.005}_{-0.005}$	4.223 $^{+0.015}_{-0.017}$	4.419 $^{+0.121}_{-0.107}$	17.078 $^{+0.511}_{-0.449}$	0.070 $^{+0.002}_{-0.002}$
ELARS05	2.217 $^{+0.009}_{-0.009}$	3.679 $^{+0.023}_{-0.018}$	5.881 $^{+0.217}_{-0.180}$	26.523 $^{+1.006}_{-0.890}$	0.148 $^{+0.006}_{-0.006}$
ELARS06	1.029 $^{+0.006}_{-0.007}$	1.312 $^{+0.018}_{-0.025}$	1.297 $^{+0.142}_{-0.096}$	12.610 $^{+1.402}_{-0.956}$	0.060 $^{+0.005}_{-0.005}$
ELARS07 ^a	1.148 $^{+0.009}_{-0.006}$	2.537 $^{+0.028}_{-0.032}$	0.811 $^{+0.129}_{-0.159}$	7.062 $^{+1.137}_{-1.383}$	0.032 $^{+0.006}_{-0.006}$
ELARS08 ^a	0.821 $^{+0.005}_{-0.004}$	1.740 $^{+0.019}_{-0.016}$	1.375 $^{+0.116}_{-0.113}$	16.738 $^{+1.413}_{-1.446}$	0.017 $^{+0.002}_{-0.002}$
ELARS09 ^a	0.817 $^{+0.004}_{-0.002}$	0.756 $^{+0.015}_{-0.012}$	0.461 $^{+0.079}_{-0.083}$	5.648 $^{+0.978}_{-1.029}$	0.054 $^{+0.010}_{-0.010}$
ELARS10	0.552 $^{+0.005}_{-0.007}$	1.379 $^{+0.016}_{-0.017}$	0.929 $^{+0.121}_{-0.104}$	16.825 $^{+2.425}_{-1.890}$	0.016 $^{+0.002}_{-0.002}$
ELARS11 ^a	0.697 $^{+0.003}_{-0.003}$	0.911 $^{+0.013}_{-0.011}$	0.621 $^{+0.070}_{-0.062}$	8.913 $^{+1.046}_{-0.916}$	0.065 $^{+0.007}_{-0.007}$
ELARS12 ^a	0.635 $^{+0.002}_{-0.004}$	2.311 $^{+0.019}_{-0.015}$	≤ 0.082	≤ 1.272	≤ 0.002
ELARS13	0.672 $^{+0.005}_{-0.004}$	0.886 $^{+0.006}_{-0.007}$	2.532 $^{+0.092}_{-0.087}$	37.700 $^{+1.627}_{-1.384}$	0.207 $^{+0.008}_{-0.008}$
ELARS14 ^a	0.515 $^{+0.003}_{-0.003}$	1.080 $^{+0.009}_{-0.011}$	≤ 0.066	≤ 1.270	≤ 0.005
ELARS15	0.404 $^{+0.004}_{-0.005}$	0.646 $^{+0.020}_{-0.018}$	0.807 $^{+0.116}_{-0.104}$	19.969 $^{+3.002}_{-2.643}$	0.124 $^{+0.018}_{-0.018}$
ELARS16	0.267 $^{+0.002}_{-0.003}$	0.345 $^{+0.009}_{-0.012}$	≤ 0.063	≤ 2.377	≤ 0.009
ELARS17	0.399 $^{+0.005}_{-0.006}$	0.571 $^{+0.018}_{-0.015}$	0.774 $^{+0.117}_{-0.097}$	19.403 $^{+3.108}_{-2.470}$	0.082 $^{+0.012}_{-0.012}$
ELARS18	0.220 $^{+0.003}_{-0.002}$	0.344 $^{+0.012}_{-0.012}$	0.173 $^{+0.059}_{-0.075}$	7.877 $^{+2.730}_{-3.330}$	0.030 $^{+0.013}_{-0.013}$
ELARS19 ^a	0.270 $^{+0.002}_{-0.002}$	0.430 $^{+0.008}_{-0.009}$	0.270 $^{+0.053}_{-0.043}$	9.996 $^{+2.028}_{-1.559}$	0.064 $^{+0.010}_{-0.010}$
ELARS20	0.273 $^{+0.002}_{-0.002}$	0.522 $^{+0.009}_{-0.006}$	0.215 $^{+0.049}_{-0.052}$	7.867 $^{+1.844}_{-1.964}$	0.031 $^{+0.008}_{-0.008}$
ELARS21	0.124 $^{+0.002}_{-0.002}$	0.118 $^{+0.010}_{-0.008}$	0.111 $^{+0.042}_{-0.039}$	8.961 $^{+3.473}_{-3.117}$	0.047 $^{+0.033}_{-0.033}$
ELARS22 ^a	2.723 $^{+0.011}_{-0.006}$	3.644 $^{+0.054}_{-0.055}$	1.854 $^{+0.139}_{-0.152}$	6.808 $^{+0.530}_{-0.562}$	0.056 $^{+0.005}_{-0.005}$
ELARS23	2.295 $^{+0.014}_{-0.011}$	4.222 $^{+0.081}_{-0.073}$	1.493 $^{+0.214}_{-0.241}$	6.507 $^{+0.958}_{-1.073}$	0.040 $^{+0.007}_{-0.007}$
ELARS24	2.007 $^{+0.010}_{-0.010}$	6.929 $^{+0.064}_{-0.071}$	4.472 $^{+0.180}_{-0.184}$	22.283 $^{+0.982}_{-0.927}$	0.004 $^{+0.000}_{-0.000}$
ELARS25 ^a	1.718 $^{+0.011}_{-0.011}$	1.954 $^{+0.040}_{-0.060}$	1.643 $^{+0.183}_{-0.203}$	9.564 $^{+1.098}_{-1.173}$	0.094 $^{+0.012}_{-0.012}$
ELARS26 ^a	1.037 $^{+0.008}_{-0.009}$	3.305 $^{+0.048}_{-0.053}$	2.233 $^{+0.176}_{-0.171}$	21.547 $^{+1.689}_{-1.829}$	0.059 $^{+0.005}_{-0.005}$
ELARS27 ^a	1.089 $^{+0.009}_{-0.010}$	1.865 $^{+0.038}_{-0.045}$	2.051 $^{+0.159}_{-0.156}$	18.832 $^{+1.638}_{-1.491}$	0.115 $^{+0.011}_{-0.011}$
ELARS28	1.180 $^{+0.006}_{-0.008}$	2.326 $^{+0.041}_{-0.048}$	0.370 $^{+0.150}_{-0.133}$	3.138 $^{+1.285}_{-1.128}$	0.013 $^{+0.005}_{-0.005}$
Tol1214	0.304 $^{+0.002}_{-0.002}$	0.925 $^{+0.015}_{-0.016}$	2.180 $^{+0.049}_{-0.045}$	71.715 $^{+2.008}_{-1.887}$	0.271 $^{+0.007}_{-0.007}$
Tol1247	10.381 $^{+0.022}_{-0.019}$	25.306 $^{+0.066}_{-0.062}$	24.794 $^{+0.391}_{-0.322}$	23.883 $^{+0.403}_{-0.351}$	0.059 $^{+0.001}_{-0.001}$
J1156	24.012 $^{+0.423}_{-0.429}$	31.913 $^{+0.763}_{-0.706}$	63.696 $^{+4.799}_{-4.555}$	26.527 $^{+2.124}_{-2.230}$	0.115 $^{+0.009}_{-0.009}$

^a The Ly α emission from these galaxies are potentially underestimated due to uncertain background subtraction, see Section 3.1.3.

Table 6. Derived galaxy properties

ID	SFR _{Hα}	SFR _{FUV}	sSFR _{Hα}	Σ_{SFR}	Mass	Age	$E(B - V)_s$	$E(B - V)_n$
	(M $_{\odot}$ /yr)	(M $_{\odot}$ /yr)	(10 $^{-10}$ yr $^{-1}$)	(M $_{\odot}$ /yr/kpc 2)	(10 10 M $_{\odot}$)	(Myr)		
(1)	(2)	(3)	(4)	(5)	(6)	(7)	(8)	(9)
LARS 1	3.86 $^{0.01}_{0.01}$	3.04 $^{0.01}_{0.01}$	2.83 $^{0.03}_{0.03}$	0.472 $^{0.003}_{0.003}$	1.65 $^{0.04}_{0.04}$	7.95 $^{0.71}_{0.50}$	0.09 $^{0.00}_{0.00}$	0.140 $^{0.002}_{0.002}$
LARS 2	0.86 $^{0.01}_{0.01}$	2.43 $^{0.06}_{0.06}$	2.44 $^{0.06}_{0.06}$	0.110 $^{0.001}_{0.001}$	0.57 $^{0.03}_{0.03}$	19.64 $^{1.37}_{1.74}$	0.17 $^{0.00}_{0.00}$	0.002 $^{0.009}_{0.006}$
LARS 3	25.52 $^{0.09}_{0.09}$	16.68 $^{0.65}_{0.44}$	26.70 $^{2.19}_{2.19}$	8.566 $^{0.297}_{0.284}$	2.15 $^{0.10}_{0.10}$	77.46 $^{1.37}_{1.14}$	0.39 $^{0.00}_{0.00}$	0.850 $^{0.011}_{0.015}$
LARS 4	3.06 $^{0.01}_{0.01}$	1.97 $^{0.01}_{0.01}$	2.72 $^{0.03}_{0.03}$	0.326 $^{0.003}_{0.003}$	1.77 $^{0.02}_{0.02}$	11.42 $^{0.58}_{0.61}$	0.09 $^{0.00}_{0.00}$	0.164 $^{0.003}_{0.004}$
LARS 5	3.19 $^{0.01}_{0.01}$	3.35 $^{0.01}_{0.01}$	4.05 $^{0.04}_{0.04}$	0.455 $^{0.003}_{0.002}$	0.84 $^{0.01}_{0.01}$	4.38 $^{0.61}_{0.49}$	0.07 $^{0.00}_{0.00}$	0.138 $^{0.002}_{0.002}$
LARS 6	0.40 $^{0.00}_{0.00}$	0.39 $^{0.00}_{0.00}$	1.47 $^{0.09}_{0.09}$	0.024 $^{0.001}_{0.001}$	0.39 $^{0.02}_{0.02}$	13.38 $^{1.86}_{1.01}$	0.05 $^{0.00}_{0.00}$	0.053 $^{0.010}_{0.012}$
LARS 7	3.70 $^{0.01}_{0.01}$	2.06 $^{0.01}_{0.01}$	6.97 $^{0.07}_{0.07}$	1.086 $^{0.004}_{0.008}$	0.86 $^{0.02}_{0.02}$	24.68 $^{0.74}_{0.90}$	0.06 $^{0.00}_{0.00}$	0.248 $^{0.003}_{0.002}$
LARS 8	41.73 $^{0.47}_{0.47}$	4.63 $^{0.07}_{0.07}$	4.68 $^{0.70}_{0.70}$	0.799 $^{0.105}_{0.165}$	10.01 $^{0.35}_{0.35}$	72.89 $^{8.50}_{8.41}$	0.12 $^{0.00}_{0.00}$	0.806 $^{0.006}_{0.008}$
LARS 9	23.08 $^{0.03}_{0.03}$	9.71 $^{0.13}_{0.09}$	4.59 $^{0.04}_{0.04}$	0.299 $^{0.002}_{0.002}$	5.85 $^{0.07}_{0.07}$	20.40 $^{6.72}_{4.24}$	0.10 $^{0.00}_{0.00}$	0.338 $^{0.002}_{0.002}$
LARS 10	5.72 $^{0.06}_{0.06}$	4.78 $^{0.09}_{0.10}$	5.22 $^{0.30}_{0.30}$	0.378 $^{0.024}_{0.019}$	2.35 $^{0.09}_{0.09}$	38.16 $^{1.49}_{1.27}$	0.19 $^{0.00}_{0.00}$	0.691 $^{0.019}_{0.022}$
LARS 11	16.90 $^{0.13}_{0.13}$	36.45 $^{1.79}_{1.82}$	1.36 $^{0.05}_{0.05}$	0.090 $^{0.001}_{0.001}$	15.24 $^{0.37}_{0.37}$	32.26 $^{0.52}_{0.50}$	0.19 $^{0.00}_{0.00}$	0.477 $^{0.050}_{0.050}$
LARS 12	34.98 $^{0.23}_{0.23}$	9.18 $^{0.08}_{0.08}$	12.19 $^{0.20}_{0.20}$	1.835 $^{0.027}_{0.021}$	3.20 $^{0.08}_{0.08}$	14.59 $^{0.92}_{1.60}$	0.05 $^{0.00}_{0.00}$	0.639 $^{0.004}_{0.005}$
LARS 13	40.47 $^{0.14}_{0.14}$	65.27 $^{1.30}_{1.99}$	28.27 $^{4.72}_{4.72}$	0.528 $^{0.009}_{0.008}$	3.83 $^{0.45}_{0.45}$	35.42 $^{1.92}_{2.72}$	0.22 $^{0.00}_{0.01}$	0.529 $^{0.008}_{0.007}$
LARS 14	13.03 $^{0.16}_{0.16}$	16.47 $^{0.21}_{0.17}$	13.29 $^{0.35}_{0.35}$	0.701 $^{0.007}_{0.006}$	1.18 $^{0.08}_{0.08}$	11.89 $^{2.59}_{2.41}$	0.08 $^{0.00}_{0.00}$	0.103 $^{0.003}_{0.003}$
ELARS 1	25.71 $^{0.03}_{0.03}$	6.18 $^{0.02}_{0.02}$	3.74 $^{0.05}_{0.05}$	1.329 $^{0.009}_{0.011}$	7.85 $^{0.08}_{0.08}$	21.52 $^{0.66}_{0.27}$	0.14 $^{0.00}_{0.00}$	0.535 $^{0.002}_{0.003}$
ELARS 2	3.32 $^{0.02}_{0.02}$	3.53 $^{0.02}_{0.02}$	1.39 $^{0.02}_{0.02}$	0.100 $^{0.001}_{0.001}$	3.08 $^{0.02}_{0.02}$	36.77 $^{0.49}_{0.53}$	0.07 $^{0.00}_{0.00}$	0.000 $^{0.000}_{0.000}$
ELARS 3	13.80 $^{0.03}_{0.03}$	29.22 $^{0.40}_{0.41}$	0.67 $^{0.01}_{0.01}$	0.044 $^{0.000}_{0.000}$	8.96 $^{0.11}_{0.11}$	26.60 $^{0.50}_{0.61}$	0.29 $^{0.00}_{0.00}$	0.385 $^{0.004}_{0.005}$
ELARS 4	3.89 $^{0.02}_{0.02}$	4.08 $^{0.02}_{0.01}$	1.47 $^{0.02}_{0.02}$	0.143 $^{0.001}_{0.001}$	3.32 $^{0.03}_{0.03}$	39.32 $^{0.71}_{0.54}$	0.09 $^{0.00}_{0.00}$	0.223 $^{0.002}_{0.003}$
ELARS 5	2.45 $^{0.01}_{0.01}$	7.30 $^{0.19}_{0.16}$	0.33 $^{0.01}_{0.01}$	0.010 $^{0.000}_{0.000}$	7.08 $^{0.07}_{0.07}$	49.82 $^{0.57}_{0.76}$	0.17 $^{0.00}_{0.00}$	0.088 $^{0.009}_{0.009}$
ELARS 6	1.34 $^{0.03}_{0.03}$	1.49 $^{0.01}_{0.02}$	1.44 $^{0.04}_{0.04}$	0.012 $^{0.000}_{0.000}$	1.53 $^{0.03}_{0.03}$	42.80 $^{1.86}_{1.76}$	0.08 $^{0.00}_{0.00}$	0.265 $^{0.008}_{0.012}$
ELARS 7	1.56 $^{0.02}_{0.02}$	1.40 $^{0.01}_{0.01}$	34.57 $^{1.00}_{1.00}$	6.469 $^{0.106}_{0.135}$	1.44 $^{0.08}_{0.08}$	30.81 $^{3.70}_{3.24}$	0.07 $^{0.00}_{0.00}$	0.055 $^{0.004}_{0.004}$
ELARS 8	4.94 $^{0.05}_{0.05}$	4.53 $^{0.15}_{0.15}$	0.65 $^{0.05}_{0.05}$	0.015 $^{0.001}_{0.001}$	4.55 $^{0.10}_{0.10}$	45.16 $^{1.05}_{1.07}$	0.22 $^{0.00}_{0.00}$	0.689 $^{0.025}_{0.026}$
ELARS 9	0.52 $^{0.01}_{0.01}$	3.00 $^{0.09}_{0.09}$	1.68 $^{0.70}_{0.70}$	0.096 $^{0.008}_{0.028}$	0.54 $^{0.04}_{0.04}$	42.33 $^{1.70}_{1.92}$	0.18 $^{0.00}_{0.00}$	0.105 $^{0.010}_{0.008}$
ELARS 10	3.50 $^{0.04}_{0.04}$	3.42 $^{0.17}_{0.16}$	3.01 $^{0.15}_{0.15}$	0.138 $^{0.006}_{0.005}$	2.02 $^{0.08}_{0.08}$	61.42 $^{3.19}_{3.53}$	0.23 $^{0.01}_{0.01}$	0.642 $^{0.021}_{0.023}$
ELARS 11	0.59 $^{0.01}_{0.01}$	2.25 $^{0.05}_{0.05}$	0.28 $^{0.01}_{0.01}$	0.027 $^{0.001}_{0.001}$	1.90 $^{0.07}_{0.07}$	35.56 $^{0.81}_{1.18}$	0.17 $^{0.00}_{0.00}$	0.075 $^{0.011}_{0.010}$
ELARS 12	2.68 $^{0.02}_{0.02}$	7.13 $^{0.28}_{0.26}$	1.15 $^{0.07}_{0.07}$	0.060 $^{0.004}_{0.003}$	3.14 $^{0.11}_{0.11}$	41.93 $^{1.87}_{1.66}$	0.29 $^{0.01}_{0.00}$	0.319 $^{0.022}_{0.019}$
ELARS 13	0.76 $^{0.01}_{0.01}$	1.40 $^{0.02}_{0.03}$	1.64 $^{0.03}_{0.03}$	0.849 $^{0.013}_{0.014}$	1.17 $^{0.08}_{0.08}$	3.29 $^{0.58}_{0.62}$	0.12 $^{0.00}_{0.00}$	0.191 $^{0.007}_{0.008}$
ELARS 14	0.72 $^{0.01}_{0.01}$	3.66 $^{0.11}_{0.12}$	1.91 $^{0.18}_{0.18}$	0.091 $^{0.007}_{0.004}$	2.40 $^{0.30}_{0.30}$	22.85 $^{2.18}_{1.65}$	0.25 $^{0.00}_{0.00}$	0.089 $^{0.009}_{0.009}$
ELARS 15	0.40 $^{0.01}_{0.01}$	2.31 $^{0.15}_{0.11}$	1.31 $^{0.13}_{0.13}$	0.005 $^{0.000}_{0.000}$	1.26 $^{0.06}_{0.06}$	74.92 $^{2.75}_{3.58}$	0.22 $^{0.01}_{0.00}$	0.059 $^{0.024}_{0.023}$
ELARS 16	0.41 $^{0.01}_{0.01}$	1.67 $^{0.12}_{0.13}$	2.64 $^{0.01}_{0.01}$	0.010 $^{0.000}_{0.000}$	0.86 $^{0.03}_{0.03}$	41.02 $^{2.86}_{4.05}$	0.23 $^{0.01}_{0.01}$	0.333 $^{0.018}_{0.023}$
ELARS 17	0.58 $^{0.01}_{0.01}$	1.34 $^{0.08}_{0.08}$	0.38 $^{0.00}_{0.00}$	0.003 $^{0.000}_{0.000}$	1.36 $^{0.04}_{0.04}$	60.70 $^{3.13}_{2.03}$	0.17 $^{0.01}_{0.01}$	0.263 $^{0.028}_{0.026}$
ELARS 18	0.36 $^{0.01}_{0.01}$	0.84 $^{0.04}_{0.04}$	8.83 $^{3.10}_{3.10}$	0.030 $^{0.001}_{0.001}$	0.53 $^{0.18}_{0.18}$	73.24 $^{7.94}_{7.09}$	0.18 $^{0.01}_{0.01}$	0.271 $^{0.015}_{0.022}$
ELARS 19	0.26 $^{0.01}_{0.01}$	0.35 $^{0.01}_{0.00}$	1.73 $^{0.27}_{0.27}$	0.003 $^{0.000}_{0.000}$	0.35 $^{0.02}_{0.02}$	23.29 $^{3.52}_{3.24}$	0.07 $^{0.00}_{0.00}$	0.047 $^{0.011}_{0.011}$
ELARS 20	0.42 $^{0.00}_{0.00}$	2.26 $^{0.14}_{0.13}$	0.39 $^{0.09}_{0.09}$	0.003 $^{0.000}_{0.000}$	4.28 $^{0.20}_{0.20}$	22.97 $^{3.78}_{2.60}$	0.26 $^{0.01}_{0.01}$	0.169 $^{0.024}_{0.024}$
ELARS 21	0.15 $^{0.01}_{0.01}$	0.16 $^{0.01}_{0.00}$	0.86 $^{0.00}_{0.00}$	0.002 $^{0.000}_{0.000}$	0.44 $^{0.05}_{0.05}$	77.33 $^{6.75}_{6.08}$	0.07 $^{0.00}_{0.01}$	0.348 $^{0.199}_{0.249}$
ELARS 22	2.05 $^{0.03}_{0.03}$	13.17 $^{0.26}_{0.20}$	1.97 $^{0.13}_{0.13}$	0.008 $^{0.000}_{0.000}$	1.27 $^{0.06}_{0.06}$	16.49 $^{1.68}_{1.37}$	0.21 $^{0.00}_{0.00}$	0.019 $^{0.008}_{0.006}$
ELARS 23	2.31 $^{0.04}_{0.04}$	14.29 $^{0.34}_{0.52}$	0.54 $^{0.21}_{0.21}$	0.007 $^{0.001}_{0.001}$	5.58 $^{0.11}_{0.11}$	38.63 $^{1.13}_{1.19}$	0.23 $^{0.00}_{0.00}$	0.007 $^{0.022}_{0.017}$
ELARS 24	67.01 $^{0.69}_{0.69}$	22.14 $^{0.63}_{0.65}$	6.80 $^{0.45}_{0.45}$	3.181 $^{0.204}_{0.164}$	8.97 $^{0.15}_{0.15}$	24.97 $^{1.32}_{1.11}$	0.29 $^{0.00}_{0.00}$	1.196 $^{0.024}_{0.024}$
ELARS 25	1.07 $^{0.03}_{0.03}$	5.87 $^{0.16}_{0.16}$	0.70 $^{0.21}_{0.21}$	0.006 $^{0.001}_{0.000}$	3.26 $^{0.20}_{0.20}$	22.96 $^{2.07}_{2.15}$	0.17 $^{0.00}_{0.00}$	0.009 $^{0.008}_{0.010}$
ELARS 26	2.32 $^{0.04}_{0.04}$	1.32 $^{0.03}_{0.02}$	0.58 $^{0.00}_{0.00}$	0.004 $^{0.000}_{0.000}$	4.51 $^{0.06}_{0.06}$	87.91 $^{5.14}_{5.07}$	0.07 $^{0.00}_{0.00}$	0.111 $^{0.020}_{0.019}$
ELARS 27	1.10 $^{0.03}_{0.03}$	1.31 $^{0.03}_{0.02}$	0.73 $^{0.01}_{0.01}$	0.005 $^{0.000}_{0.000}$	2.00 $^{0.03}_{0.03}$	62.93 $^{2.67}_{2.30}$	0.07 $^{0.00}_{0.00}$	0.041 $^{0.032}_{0.025}$
ELARS 28	1.74 $^{0.04}_{0.04}$	7.73 $^{0.42}_{0.27}$	11.11 $^{0.56}_{0.56}$	0.012 $^{0.000}_{0.000}$	1.41 $^{0.06}_{0.06}$	25.65 $^{2.64}_{2.28}$	0.24 $^{0.01}_{0.00}$	0.136 $^{0.011}_{0.020}$
Tol 1214	0.50 $^{0.01}_{0.01}$	0.41 $^{0.01}_{0.01}$	109.13 $^{6.02}_{6.02}$	0.574 $^{0.004}_{0.004}$	0.04 $^{0.01}_{0.01}$	34.90 $^{7.52}_{7.20}$	0.08 $^{0.00}_{0.00}$	0.000 $^{0.000}_{0.000}$
Tol 1247	25.76 $^{0.06}_{0.06}$	16.65 $^{0.07}_{0.05}$	21.26 $^{0.54}_{0.54}$	1.355 $^{0.008}_{0.008}$	1.41 $^{0.04}_{0.04}$	4.20 $^{0.75}_{0.72}$	0.09 $^{0.00}_{0.00}$	0.265 $^{0.002}_{0.002}$
J1156	34.22 $^{0.76}_{0.76}$	30.03 $^{0.47}_{0.45}$	1.62 $^{0.01}_{0.01}$	0.316 $^{0.003}_{0.002}$	3.45 $^{0.30}_{0.30}$	13.58 $^{3.32}_{5.34}$	0.06 $^{0.00}_{0.00}$	0.286 $^{0.008}_{0.011}$

NOTE—(1–3) Extinction corrected SFR. (4–5) Based on extinction corrected H α luminosity within a radius of $r_{\text{p,H}\alpha}$.

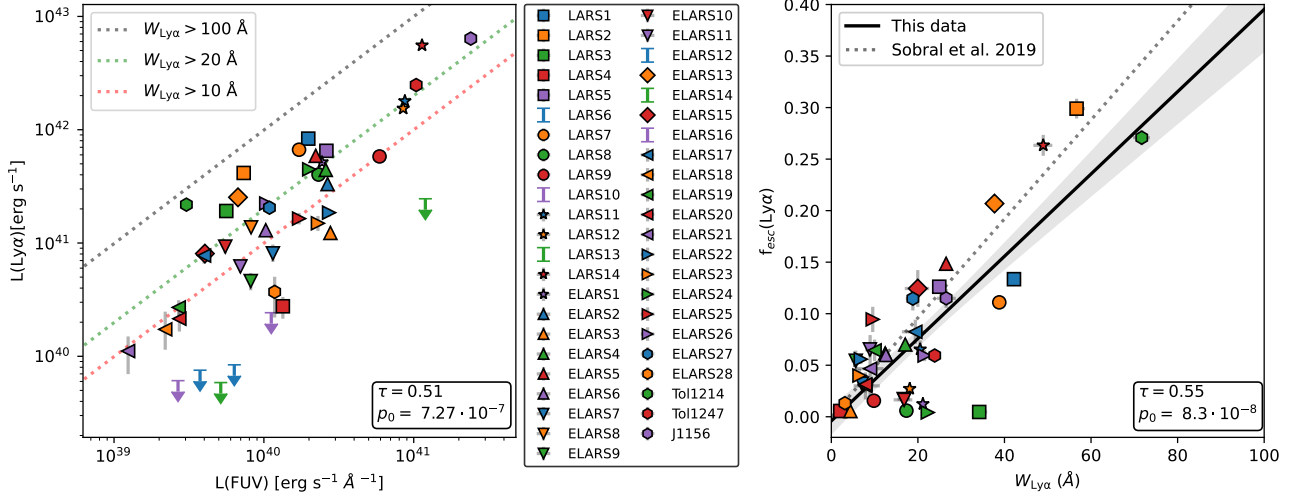


Figure 11. Left panel: The Ly α versus the FUV luminosity of the galaxies in this sample. Diagonal dashed lines show different limits of $W_{\text{Ly}\alpha}$. Right panel: f_{esc} vs $W_{\text{Ly}\alpha}$ for the galaxies. In addition to a linear fit to the current data, the relation from Sobral & Matthee (2019) is shown.

more complete picture of the ionizing photon budget. In these galaxies f_{esc} will sit below the locus in the figure. In Section 6.2 we fit f_{esc} as a linear function of $W_{\text{Ly}\alpha}$ and show how this allows Ly α to be used as a rough SFR diagnostic. Interestingly, all but one of the galaxies that fall well below the linear fit of f_{esc} vs $W_{\text{Ly}\alpha}$ in the figure have high nebular and stellar extinction. In the single case which seems to have low nebular extinction but still outlie the locus (ELARS22) the galaxy is inclined towards us and has a higher stellar than nebular extinction (0.23 and 0.05, respectively), perhaps indicating that the measured nebular extinction for this galaxy is under-estimated.

Another explanation that will cause a shift in this relation is the hardness of the stellar continuum (Sobral & Matthee 2019). A stellar population generating more ionizing flux (due to, e.g., younger age, lower metallicity, higher stellar rotation) will show a higher Ly α equivalent width, at constant f_{esc} . This effect can be measured by computing the ionizing production efficiency, ξ_{ion} , which is the ratio of ionizing photons to the dust corrected UV luminosity. For galaxies with multiple stellar populations a high ξ_{ion} value indicates that they are currently undergoing a starburst phase, while lower values indicates a less active star formation phase. For our sample we find an average $\log(\xi_{\text{ion}}/[\text{Hz erg}^{-1}]) = 24.9$ which is ~ 0.5 dex lower than the typical value for high redshift LAEs (e.g., Nakajima et al. 2018). This difference is not surprising given that our sample includes many galaxies that have lower SFR than the high redshift LAEs, and could explain the scattering of data points to lie to the left of the fitted line (i.e. galaxies with lower than average ξ_{ion}). As opposed to the effect of extinction,

inspecting ξ_{ion} for individual galaxies to see where they lie in the plot does not show any clear effects.

In Figure 12 we show the range of Ly α luminosities, FUV luminosities, and $W_{\text{Ly}\alpha}$ covered by our sample. Most of our galaxies have $40 < \log(L_{\text{Ly}\alpha}) < 42$ with a tail towards higher luminosities. Note that the non-emitters are included in the lowest bin. Comparing our data to the high redshift LAEs from Leclercq et al. (2017) it is clear that the LARS galaxies are in general fainter in Ly α (median $\log(L_{\text{Ly}\alpha})$ for LARS and MUSE LAEs are 41.3, and 42.3, respectively), but with some overlap. This difference could be due to luminosity bias, but is more likely to be caused by the quite different sample selection in this case. The MUSE LAEs are selected based on their Ly α emission, while the LARS galaxies were selected based on SFR and stellar population age. Indeed, when comparing the FUV luminosities of the two samples the difference is markedly lower (median $\log(L_{\text{FUV}})$ for LARS and MUSE LAEs are 40.1, and 40.3, respectively).

The same difference is seen in the $W_{\text{Ly}\alpha}$ histogram where the two samples are quite distinct (median $W_{\text{Ly}\alpha}$ for LARS and MUSE are 17 and 92 \AA , respectively). At high redshift finding the most extreme LAEs is more likely because of the larger volume covered, but also due to observing galaxies at the peak of star formation. It should thus be noted that the results from this study have to be treated with some care when comparing to high redshift studies, in particular if only the highest $W_{\text{Ly}\alpha}$ emitters are observed. However, the LARS+ELARS galaxies should be more representative of the Ly α properties of the general star forming galaxy population, with more dust and weaker Ly α emission.

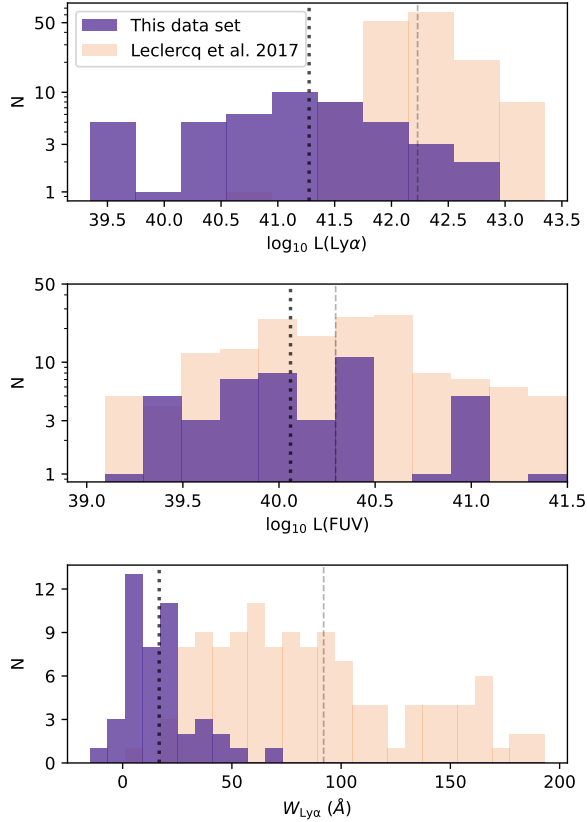


Figure 12. Histograms of $L_{\text{Ly}\alpha}$ (upper panel), L_{FUV} (middle panel), and $W_{\text{Ly}\alpha}$ (lower panel). In addition we also show histograms for data on high redshift LAEs from VLT/MUSE observations (Leclercq et al. 2017). Thick dotted vertical lines show the median $L_{\text{Ly}\alpha}$, L_{FUV} , and $W_{\text{Ly}\alpha}$ values for the net emitters in our data set and the thin dashed lines show the medians for the MUSE LAEs.

For the 14 galaxies previously presented in Hayes et al. (2014) we note that the $\text{Ly}\alpha$ luminosities, equivalent widths, and escape fractions have changed compared to the previous values. This is mainly due to the updated photometric calibration of ACS/SBC (10-30% change depending on filter) and WFC3/UVIS (10% for the F336W filter), but is also affected by the difference in global aperture between the earlier paper and this work.

5.2. The relation between f_{esc} and other properties

In Figure 13 we show the relation of f_{esc} to various properties of the galaxies that have been suggested to affect the escape of $\text{Ly}\alpha$ photons.

The stellar age and star formation quantities (global SFR, SFR density and specific SFR) are all related to ISM feedback and will strongly affect the kinematics of the ISM, both in terms of bulk motions and turbulence. With high relative (to the $\text{Ly}\alpha$ production sites) bulk motion of the neutral ISM $\text{Ly}\alpha$ photons will be able

to escape in the wings of the ISM absorption profile (e.g., Dijkstra 2017). Feedback induced turbulence and shocks will cause instabilities in the ISM that can create channels of low H I column density where $\text{Ly}\alpha$ photons can travel relatively unimpeded, also causing galaxies to have dispersion-dominated kinematics (Herenz et al. 2016). In the upper left and three middle row panels of the figure we show scatter plots of f_{esc} versus these quantities and find no strong correlations. For stellar age this may be because we use a global average (FUV-weighted) value, which includes star forming regions that are not directly involved in the $\text{Ly}\alpha$ radiative transfer. Kimm et al. (2019) perform radiation-hydrodynamic simulations of $\text{Ly}\alpha$ escape from star-forming regions and find that f_{esc} increases with stellar age up to ~ 10 Myr. Given that our total apertures contain multiple stellar populations with different ages and $\text{Ly}\alpha$ output, that we do not see this effect in our sample is expected. The overall lack of correlations with the SFR quantities could be explained by high SFR being linked to other properties that makes escape harder. For example, at low redshift the highest (extinction corrected) SFR is often found in the most dusty galaxies, and while similar systems are hard to find at high redshift they do exist (e.g., Casey et al. 2014), and many more are waiting to be detected by JWST. These dusty galaxies are also more likely to have higher global neutral gas masses. Hence, the increased mechanical energy injected into the ISM from high SFR may be combined with higher dust and gas content which will limit the escape of $\text{Ly}\alpha$ photons. Even though mechanical feedback from star formation will increase the escape probability on scales of H II regions, this is not seen in global measurements for the sample.

Both stellar mass and nebular metallicity are quantities that are linked to each other and to other galaxy properties that may affect $\text{Ly}\alpha$ escape, most notably H I mass (for the stellar mass), and dust extinction (for metallicity). In the top middle and right panels of Figure 13 we show scatter plots of f_{esc} versus these two properties. For stellar mass we find a weak anti-correlation ($\{\tau, p_0\} = \{-0.23, 0.029\}$) with substantial scatter. The anti-correlation is mainly driven by the lack of massive galaxies with high f_{esc} . From this data set it seems clear that $\text{Ly}\alpha$ escape is low in galaxies with the highest stellar mass, perhaps reflecting that these galaxies have larger neutral gas reservoirs (Pardy et al. 2014). The higher neutral gas content will in turn cause longer scattering path lengths for the $\text{Ly}\alpha$ radiative transfer, and could also make it harder for the star formation feedback to create clear channels for escape. For low stellar masses the scatter in f_{esc} is large, this could be

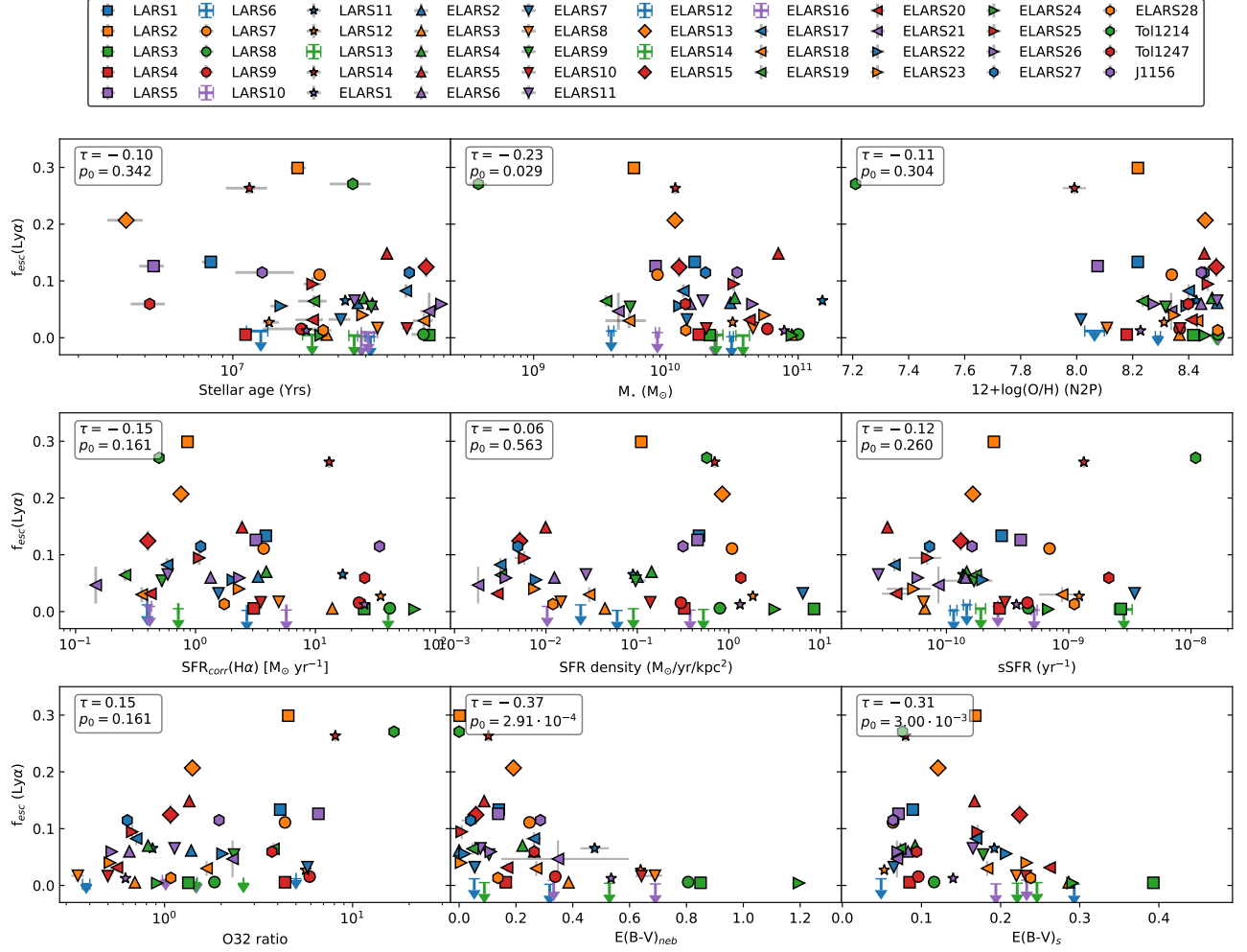


Figure 13. Scatter plots of f_{esc} versus various properties of the galaxies.

explained by variations in the neutral gas fraction, e.g., some of these galaxies may have small stellar masses compared to the neutral gas mass. In these galaxies f_{esc} will be low because of high H I column densities, while low mass galaxies that have used up a greater portion of their neutral gas will have higher escape fractions. Lower mass galaxies also have weaker gravitational potential which will make it easier for feedback to create low column density channels for Ly α escape (Laursen et al. 2009). This effect would make f_{esc} higher in low-mass galaxies on average, but would also show considerable scatter due to geometrical effects. A more detailed analysis of H I column densities and kinematics for this sample, and how they relate to Ly α escape will be given in a forthcoming paper (Le Reste et al., in prep.). The comparison with nebular metallicity does not show anything conclusive, but we note that there is a lack of data points in the low metallicity range.

The effect of ionisation state of the main star-forming regions in the galaxies (as measured by the SDSS O32

ratio) on global f_{esc} is shown in the bottom row left panel. We do not find any correlation of O32 with f_{esc} , but note that there are very few galaxies with low O32 (indicating that the ISM is not strongly ionized) that show strong Ly α escape. A highly ionized ISM in the regions where Ly α is produced thus seems to be a necessary condition for high ($\gtrsim 0.1$) f_{esc} . This result is consistent with earlier studies that also show a large scatter of f_{esc} at low O32 ratios (e.g., Henry et al. 2015; Jaskot et al. 2017; Yang et al. 2017b; Izotov et al. 2020), but we do not find any strong correlation. However, it should be noted that the sample selection is quite different for some of these studies in that the galaxies are all Ly α emitters and are selected to have strong emission. Our sample contains a number of galaxies with moderate to strong Ly α absorption which will increase the scatter substantially which is also seen in the study by Izotov et al. (2020).

In the bottom row middle and right panels we show scatter plots of f_{esc} versus nebular and stellar extinction.

Both of these are strongly anticorrelated with the escape fraction, $\{\tau, p_0\} = \{-0.37, 2.9 \cdot 10^{-4}\}$ for $E(B - V)_n$, and $\{\tau, p_0\} = \{-0.31, 3.00 \cdot 10^{-3}\}$ for $E(B - V)_s$. The correlation with nebular extinction was previously found by Runnholm et al. (2020) in a rank correlation study, where f_{esc} was found to have a strong dependence on $E(B - V)_n$. We will come back to the details of nebular extinction and escape fraction in Section 6.1. Given that nebular and stellar extinction are strongly correlated it is not surprising to find that the escape fraction is also anti-correlated to the stellar extinction.

5.3. The Ly α spatial distribution and escape fractions

As previously mentioned, a more thorough analysis and discussion of how the spatial distribution of Ly α relates to global observables for the sample in this study is given in Rasekh et al. (2022). In this paper we provide two simple observational diagnostics for the Ly α spatial extent: $r_{p, \text{Ly}\alpha}$, and $\xi_{\text{Ly}\alpha}$ (defined below). We also investigate the effect of FUV compactness (as measured by $r_p(\text{FUV})$) on the escape fraction.

In Figure 14 we show the dependence of f_{esc} on the compactness (as measured by r_p) of FUV and Ly α emission. There are no correlations found for any of these properties, but we note that high escape fractions are much less common in galaxies with large $r_{p, \text{FUV}}$. Galaxies with very extended FUV emission thus seem to be less likely to have high f_{esc} .

We define the Ly α overextension parameter, $\xi_{\text{Ly}\alpha}$, as the ratio between the Ly α and FUV continuum petrosian radii:

$$\xi_{\text{Ly}\alpha} = \frac{r_{p, \text{Ly}\alpha}}{r_{p, \text{FUV}}}. \quad (4)$$

This ratio is high for galaxies which have extensive Ly α halos caused by radiative transfer of the Ly α photons far away from where they were produced. The parameter is also high for galaxies with substantial continuum absorption in the central regions. Lower $\xi_{\text{Ly}\alpha}$ values are found in galaxies in which the Ly α escape happens along the line of sight or in which resonant scattering is less significant. In Figure 15 we show how $\xi_{\text{Ly}\alpha}$ relates to f_{esc} and $E(B - V)_n$ for our sample. We do not find any correlation between f_{esc} and $\xi_{\text{Ly}\alpha}$. Naively one might expect higher Ly α escape for galaxies where the photons escape directly with little or no radiative transfer (giving low $\xi_{\text{Ly}\alpha}$), but there are likely a number of competing effects which cause this prediction to fail. For example, in galaxies which have high escape fractions due to low dust content photons tend to travel longer paths before being destroyed, which naturally gives rise to larger Ly α halos. Hayes et al. (2014) found an anti-correlation between $\xi_{\text{Ly}\alpha}$ and $E(B - V)_n$ for the original LARS galaxies, however, this result is not confirmed

with the updated calibration and when including the 31 additional galaxies in this sample.

6. DISCUSSION

6.1. Ly α escape and dust extinction

As shown in Section 5.2 we find a strong anti-correlation between f_{esc} and $E(B - V)_n$. In Figure 16 we show this relation together with a number of extinction curves from the literature. When comparing to dust screen models (CCM and SMC) it is clear that Ly α escape cannot be described by these simple models, both in terms of the average slope of the curve and in terms of scatter. Similar to Hayes et al. (2011) we make the assumption that f_{esc} at $E(B - V)_n \approx 0$ can be < 1 (even very small amounts of dust will affect Ly α photons due to the scattering), and fit a function of the form:

$$f_{\text{esc}} = C \cdot 10^{-0.4k_{\text{Ly}\alpha} E(B - V)_n}. \quad (5)$$

We then fit a linear function to $\log f_{\text{esc}}$ (using a censored bayesian linear regression method, LINMIX³) which yields the parameter values $C = 0.075 \pm 0.019$ and $k_{\text{Ly}\alpha} = 3.30 \pm 0.73$ where the slope and intercept uncertainties are derived from the posterior probabilities. The best fit slope is significantly flatter than the CCM and SMC curves.

There are multiple causes for the scatter in the relation that can make the Ly α escape fraction move both up and down (see also Hayes et al. 2011).

- Resonant scattering of the Ly α photons in the neutral hydrogen gas cause the effective path lengths (or optical depth) to increase. This means that more photons are absorbed by dust and f_{esc} consequently goes down (e.g., Dijkstra 2017). For this data set the effect is clearly seen at low nebular extinction. Even with minimal dust content the effective optical depth at the Ly α wavelength becomes large and the escape fraction is strongly decreased compared to the prediction of the dust screen model.
- In a clumpy ISM (where most of the dust is confined within the dense clumps of H I gas), the Ly α photons can scatter on the surface of the clumps and thus avoid entering the regions where the dust content is highest. In this situation Ly α photons may suffer less from extinction than both the stellar continuum and the optical nebular line emission (an effect found in the theoretical work of Neufeld 1991), causing the escape fraction to be

³ <https://github.com/jmeyers314/linmix> and Kelly (2007)

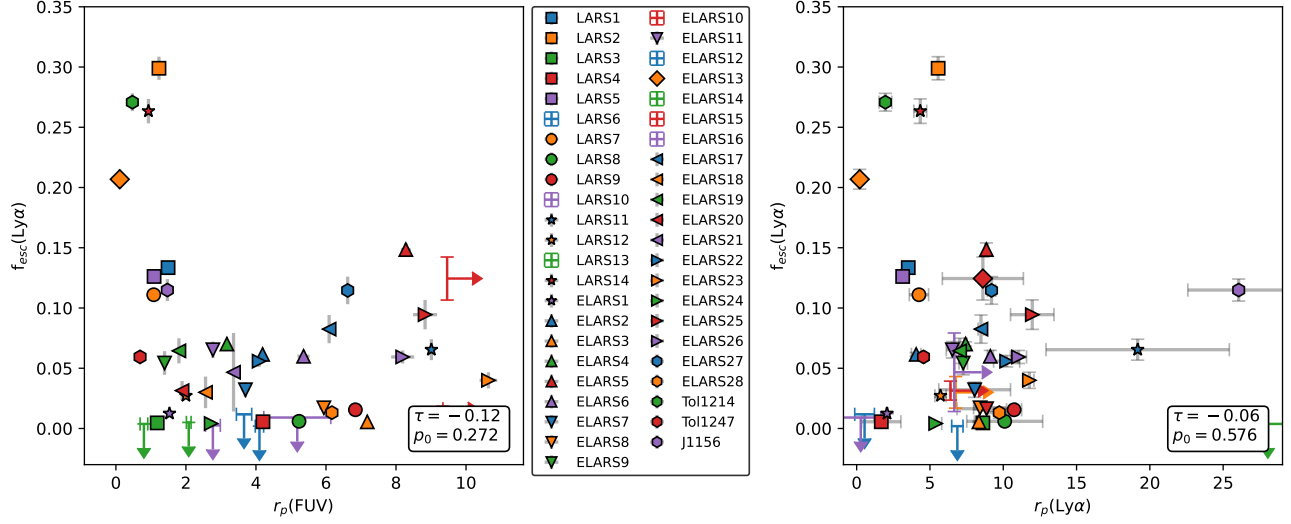


Figure 14. Scatter plots of f_{esc} versus petrosian radii in FUV (left panel) and Ly α (right panel). Note that the galaxy id labels refer to the left panel, therefore some of the galaxies with limits in the right panel are not shown as such in the legend. Please refer to Table 5 for individual galaxy limits.

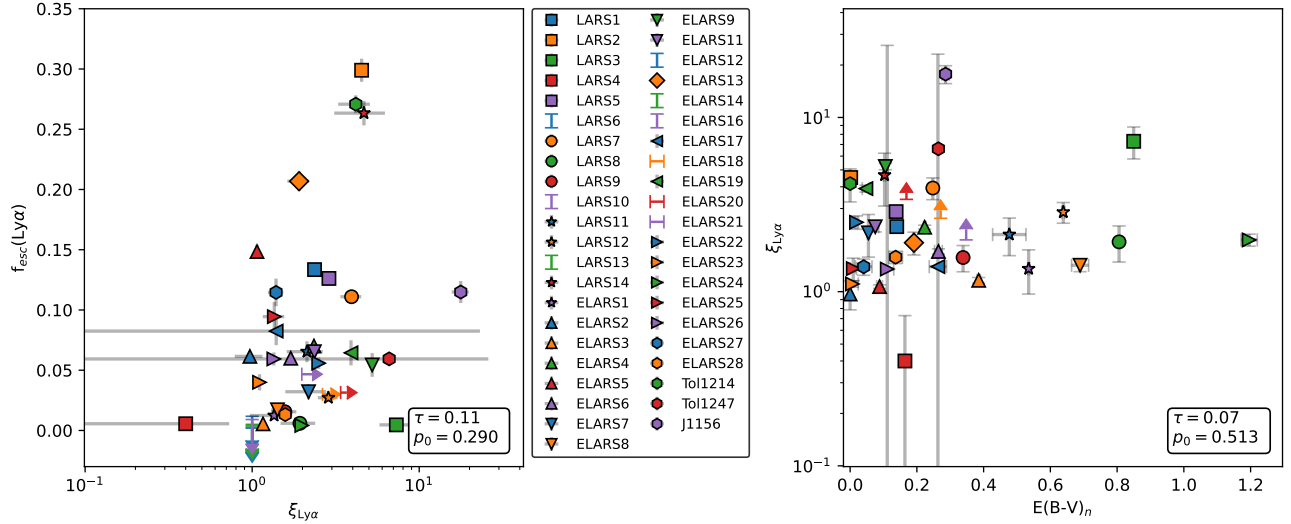


Figure 15. Left panel: f_{esc} versus the $\xi_{\text{Ly}\alpha}$ parameter. Right panel: $\xi_{\text{Ly}\alpha}$ versus nebular extinction. Galaxies with lower limits on $r_{p,\text{FUV}}$ (ELARS15 and ELARS22) are excluded from these plots.

higher than the dust screen models would imply. However, if this effect was present for a majority of the galaxies we would also find a positive correlation of $W_{\text{Ly}\alpha}$ and $E(B - V)_n$ (Scarlata et al. 2009), which we do not find (in fact, they are anti-correlated to the same degree that f_{esc} and $E(B - V)_n$ is). More recent radiative transfer simulations have also found that this type of scattering does not have a large effect on the output Ly α emission (e.g., Laursen et al. 2013; Duval et al. 2016). It is not excluded that f_{esc} could be boosted by this effect in some of the sources, but

it does not seem to be in play for the sample as a whole.

- Pure dust geometrical effects can also cause f_{esc} to be higher than for the uniform dust screen models. In Figure 16 we show the effect of a clumpy dust screen (Natta & Panagia 1984; Calzetti et al. 1994; Scarlata et al. 2009) on the Ly α escape fraction. As the dust content inside the clumps increases the $f_{\text{esc}}-E(B - V)_n$ relation will move along these locii (N is the average number of clumps along the line of sight). The extinction will then become more and more gray — as the individual clump

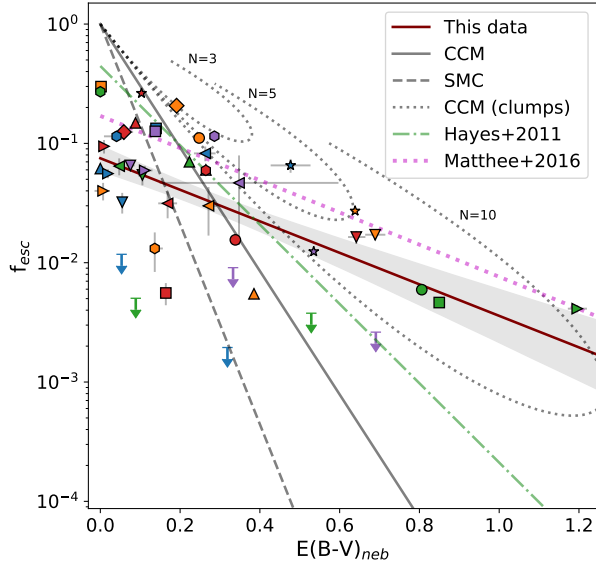


Figure 16. Global escape fraction of $\text{Ly}\alpha$ versus nebular extinction. The gray lines show where the points would fall for different ISM extinction curves. The curve labeled CCM is the galactic extinction curve from Cardelli et al. (1989) and SMC is from Prevot et al. (1984). Coloured lines show curves derived from fitting a line to observation from this and other $\text{Ly}\alpha$ studies. Note that that Hayes et al. (2011) and Matthee et al. (2016) use stellar extinction, for this comparison we multiply their $E(B - V)$ values by a factor 2.27 (Calzetti et al. 2000). The dotted gray lines (labeled CCM (clumps)) show clumpy dust models with varying numbers of clumps along the line of sight.

extinction becomes high the attenuation will tend toward a constant e^{-N} . Many of the galaxies in our sample (in particular the ones with high extinction) show escape fractions that are consistent with clumpy dust geometry.

The overall correlation of extinction and f_{esc} was found already in the original LARS publications (Hayes et al. 2014), and also by other theoretical and observational studies at low and high redshift (Verhamme et al. 2008; Atek et al. 2009; Scarlata et al. 2009; Kornei et al. 2010; Hayes et al. 2011; Matthee et al. 2016). In order to make the comparison to the studies using stellar extinction we use the conversion $E(B - V)_n = 2.27E(B - V)_s$ (Calzetti et al. 2000), and convert the stellar extinctions given in the other publications to nebular. This ratio of stellar to nebular extinction is explained by nebular emission originating from regions within galaxies with higher density ISM, but was derived for a small sample of nearby galaxies. The number is thus not necessarily applicable to the high redshift samples compared with

here, but a similar ratio (2.077 ± 0.088) was found by Reddy et al. (2020) for sample of $z \sim 2$ galaxies.

Similar to this study these authors find that if $\text{Ly}\alpha$ escape were to be explained by extinction alone, the nebular attenuation curve needs to be considerably more shallow than the standard dust screen models. In this paper we include galaxies with substantial extinction, and find a shallower slope than all but one of the earlier studies. The slope is remarkably similar to the one found by Matthee et al. (2016), who uses a sample of 488 $\text{H}\alpha$ -selected galaxies at $z \sim 2$. The sample in their study includes galaxies with $E(B - V)_s \lesssim 0.5$ which, when applying the stellar to nebular extinction conversion, gives a similar range of extinctions as in this data set.

The shallow effective attenuation curve for $\text{Ly}\alpha$ thus seems to be caused by a combination of radiative scatter and dust geometry effects. At low extinction, resonant scattering causes the optical depth for $\text{Ly}\alpha$ photons to become longer and f_{esc} consequently is lowered. The effect of a clumpy dust geometry on the effective attenuation is small at low dust content, and the average f_{esc} thus becomes lower than a simple dust screen would predict (0.075 at $E(B - V)_n = 0$ for the fit above). At higher dust content resonant scattering seems to become less important, and the effects of a clumpy dust geometry results in higher f_{esc} than predicted. One interpretation of this result is that the $\text{Ly}\alpha$ radiative transfer in sufficiently dusty galaxies starts to be less dominated by resonant scattering effects. Instead it is the dust content and clump distribution that has the largest effect on the escape fraction. Remarkably, none of the galaxies with $E(B - V)_n > 0.6$ sits below the dust screen models in the figure, indicating that optical depth effects from resonant scattering are less prominent in this regime. The caveat to this conclusion is that resonant scattering in a clumpy H I + dust medium can also lead to boosted $\text{Ly}\alpha$ escape (Neufeld 1991). However, as discussed above, this effect is likely not enough to cause the observed escape fractions.

While a general prediction of the f_{esc} evolution with redshift based on the overall changes to extinction over cosmic time (Hayes et al. 2011) is outside the scope of this paper we note that the significantly lower slope found in this study means that f_{esc} would evolve less with redshift compared to the earlier study.

6.2. $\text{Ly}\alpha$ luminosity as a diagnostic of star formation rate

The use of $\text{Ly}\alpha$ luminosity to measure star formation rates in galaxies is problematic because of the uncertainties in escape fraction. In contrast to other nebular

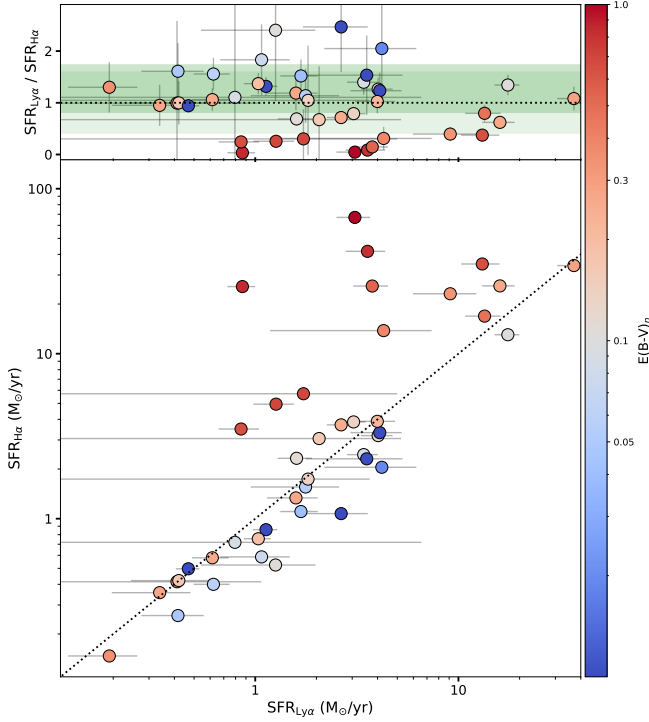


Figure 17. Comparison of the f_{esc} -corrected Ly α SFR diagnostic with SFR derived from H α . The color scale of the circles indicate the $E(B - V)_n$ of the galaxies. Galaxies with a zero or negative Ly α luminosity are excluded from this plot. The dotted line shows the 1-to-1 relation. The upper plot shows the ratio $\text{SFR}_{\text{Ly}\alpha}/\text{SFR}_{\text{H}\alpha}$. The light green band shows the standard deviation of the ratios for the full sample, while the darker green band shows the standard deviation for a sub-sample with $E(B - V)_n < 0.3$.

hydrogen lines (e.g., H α or H β) a simple dust correction is not enough to get measurements of similar precision. Nevertheless earlier studies showed correlations of Ly α luminosity with FUV (e.g., Wisotzki et al. 2016) or H α luminosity (e.g., Hayes et al. 2010), albeit with large scatter. Sobral & Matthee (2019) used a sample of 218 Ly α + H α emitters at $z \lesssim 0.3$ and $z \sim 2.2$ – 2.6 to derive a SFR calibration valid for Ly α luminosity. They find a fairly tight linear relation between f_{esc} and $W_{\text{Ly}\alpha}$ and use this to correct the observed Ly α luminosities which can then be used to define a Ly α -based SFR calibration. This calibration does not require any knowledge of the extinction or escape fraction, but can be used with $W_{\text{Ly}\alpha}$ and luminosity alone.

In Figure 11 we show a linear fit of f_{esc} as a function of $W_{\text{Ly}\alpha}$ (again using LINMIX referenced above):

$$f_{\text{esc}} = (0.0040 \pm 0.00050 \cdot W_{\text{Ly}\alpha}) \pm 0.013, \quad (6)$$

where the error to the right is the uncertainty of the fitted intercept (the best-fit intercept value itself is negligible compared to the uncertainty). While the fit has a

quite small statistical uncertainty (~ 5 – 10% for the range of $W_{\text{Ly}\alpha}$ in this sample), there are also systematic effects that come into play (see Section 5.1 for a discussion of these), in particular the effect of extinction. The found relation is significantly shallower than the one found by Sobral & Matthee (2019), even when comparing to their low redshift fit. As discussed by these authors, the relation of f_{esc} versus $W_{\text{Ly}\alpha}$ is affected strongly by the dust content of the galaxies, and the difference in slope we find could be due to the inclusion of more dusty galaxies in our sample (or other selection effects).

To find an expression for SFR as a function of Ly α luminosity we rewrite Equation 3 and use the H α SFR calibration of Kennicutt & Evans (2012). We then replace f_{esc} with the relation found above and arrive at:

$$\text{SFR}_{\text{Ly}\alpha} = \frac{C_{\text{H}\alpha}^{-1}}{8.7 f_{\text{esc}}} L_{\text{Ly}\alpha} = \frac{5.37 \cdot 10^{-42}}{0.035 \cdot W_{\text{Ly}\alpha}} L_{\text{Ly}\alpha}, \quad (7)$$

where $C_{\text{H}\alpha}$ is the SFR calibration constant from Kennicutt & Evans (2012). Note that this calibration is valid for extinction corrected H α , and $\text{SFR}_{\text{Ly}\alpha}$ thus also provides a dust corrected estimate of the star formation rate. The uncertainty of the f_{esc} ($W_{\text{Ly}\alpha}$) relation translates into an uncertainty on the SFR of ~ 5 – 10% . In Figure 17 we show how the Ly α -based SFR calibration compares to the H α SFR for our sample. Overall the Ly α -based rate follows the H α calibration well, but the scatter is large. The average relative residual for the full sample is 5%, but with a scatter of 59% (0.20 dex). The standard error of mean (σ/\sqrt{N}) for the calibration is 9%. The high scatter seems to be driven by the systemic uncertainties of the $W_{\text{Ly}\alpha}$ to f_{esc} conversion, and in particular the high extinction galaxies that have severely underestimated SFR. If we instead consider only galaxies with low extinction ($E(B - V)_n < 0.3$) the average relative residual is +30%, the scatter is reduced to 46% (0.16 dex), and the standard error of mean stays the same. The positive offset found in this case may reflect systematic effects on the f_{esc} relation resulting from variations in the ionizing radiation production efficiency. Galaxies with less bursty star formation (older average stellar ages) will tend to have over-estimated escape fractions from the fit and will thus get an over-estimated SFR from the diagnostic. The f_{esc} to $W_{\text{Ly}\alpha}$ relation stays the same (within the uncertainties) when excluding high extinction galaxies.

Another systematic uncertainty in the calibration is the assumption on the value of $C_{\text{H}\alpha}$, which itself depends on the age of the stellar population generating the ionizing photons (and the ionized ISM temperature). If the age is significantly lower than the assumption made by Kennicutt & Evans (2012), with massive star forma-

tion already in equilibrium, the SFR could be overestimated by a factor ~ 2 (for ionizing clusters with age $\leq 3 - 4$ Myr). Note that if the $f_{\text{esc}}-W_{\text{Ly}\alpha}$ relation is inverted and $W_{\text{Ly}\alpha}$ at 100% escape calculated, the intrinsic equivalent widths would fall around $200 - 400 \text{ \AA}$. These values are typical of very young bursts of massive star formation, which are the ones probably driving the observed correlation. In any case, we want to stress that this does not affect the comparison shown in Figure 17, given that the SFR indicators there use the same constant. For simplicity and re-usability we choose to use the standard calibration in this work.

The scatter found from comparing to $\text{SFR}_{\text{H}\alpha}$ is comparable to the one reported by Sobral & Matthee (2019), who, comparing to dust corrected UV-based SFR find a scatter of 0.2–0.3 dex. It is also similar to the typical scatter found when comparing extinction corrected $\text{H}\alpha$ SFR to FIR SFR, ~ 0.3 dex (e.g., Domínguez Sánchez et al. 2012). By applying a cut on the extinction we find a scatter which is somewhat lower. Variations in star formation histories of the galaxies (giving rise to variations in the ionizing radiation production efficiency) are likely responsible for part of the remaining scatter. The $\text{Ly}\alpha$ based SFR calibration presented here can thus provide estimates for SFR in high redshift LAEs which do not have any optical line measurements. These estimates will be better if the galaxies have low extinction and similar star formation history as our sample. Without access to the optical lines it is hard to constrain the extinction, but a rough selection could be done using rest-frame UV stellar continuum slopes or SED fitting.

6.3. The effect of aperture size on measurements of f_{esc} and $\text{Ly}\alpha$ luminosity

In Section 4.3 we show and describe how we use stacked growth curves to estimate the aperture losses of $\text{Ly}\alpha$ in the sample and how this translates to some other observational cases. The quite severe losses estimated for our sample do not change the results found for f_{esc} , but the SFR calibration comparison discussed in the previous section could be affected. However, given the large scatter for this relation the overall effect is too small to make a difference to the comparison.

$\text{Ly}\alpha$ emitters at $z \sim 0.3$ is an interesting case because it is possible to observe Lyman continuum (LyC) emission with HST/COS at this redshift. A number of studies targeting galaxies at this redshift have detected LyC emission, and also observe the $\text{Ly}\alpha$ spectrum with COS (e.g., Izotov et al. 2018; Flury et al. 2022). Escape of ionizing photons have been found to correlate with f_{esc} , but if there is a significant amount of $\text{Ly}\alpha$ flux missing from these measurement these conclusions could be mis-

leading. In this study we find that $27 \pm 23\%$ of the $\text{Ly}\alpha$ flux is outside of the COS aperture. An average offset of this magnitude for the individual galaxies in these studies will not change the found correlations, but if there are other dependencies on the amount of $\text{Ly}\alpha$ that is emitted from the outskirts of galaxies there may be systematics of the relations that are poorly constrained. In addition, Rasekh et al. (in prep.) finds that the fraction of $\text{Ly}\alpha$ emitted far outside the star-forming regions for Green Peas seems to be considerably smaller for Lyman continuum leaking galaxies (see also Verhamme et al. 2015). The aperture losses found for the sample in this paper may thus not be applicable to these galaxies and are probably lower than the number reported here.

At high redshift ($z \sim 3$) the aperture losses are consistent with zero for a typical slit width of $1''$, and measurements using this setup should provide good estimates of the total $\text{Ly}\alpha$ flux. However, at extreme redshifts and when using narrow slits (e.g., using the MOS mode with JWST/NIRSPEC and a single slitlet width) the slit loss is very high. In addition, at high redshifts, much more of the circumgalactic medium and ISM inside galaxies is expected to be neutral. Radiative transfer simulations show that this can lead to more radiative transfer of $\text{Ly}\alpha$ photons and thus larger spatial sizes of $\text{Ly}\alpha$ halos (Laursen et al. 2019). Our estimated aperture losses should thus be treated as lower limits in this case.

When using the estimated average aperture losses to correct f_{esc} it should be noted that the values presented here require that all of the $\text{H}\alpha$ emission is measured (i.e. the $\text{H}\alpha$ aperture covers all of the star forming regions in the galaxy). In a matched aperture COS (FUV) and SDSS (optical) setup observing nearby galaxies also $\text{H}\alpha$ will be affected by aperture losses and the simple correction suggested here suffer from additional systematic uncertainty. This could also be true for the NIRSPEC setup pictured above where the very narrow slit width will not cover the full star-forming extent of the galaxies. In the intermediate redshift range all of the $\text{H}\alpha$ emission will be easily measured and our loss values should hold.

7. SUMMARY

In this paper we present $\text{Ly}\alpha$ imaging of a sample of 45 star-forming galaxies at low redshift. We describe the sample selection and data reduction, including specialized tools to match the FUV PSF to the optical data. We also provide a detailed description of the pixel SED-fitting code we use to obtain secure $\text{Ly}\alpha$, $\text{H}\alpha$, and stellar population property maps, as well as error maps for these quantities, for the galaxies.

We then perform circular photometry on the resulting maps to obtain global measurements of fluxes ($\text{Ly}\alpha$, $\text{H}\beta$,

H α , and FUV stellar continuum) and stellar properties (mass, luminosity-weighted stellar population age, and stellar dust extinction). The measurements are also used to derive maps and global measurements of Ly α equivalent width, Ly α escape fraction, star formation rate, and nebular dust extinction. Different size estimates for the Ly α , H α , and FUV emission are obtained using Petrosian radii and growth curve analysis. The main results of the study are summarized below:

- We detect Ly α emission on a global scale from 39 out of 45 galaxies. The equivalent widths and escape fractions range from ~ 1 Å to ~ 80 Å, and 0.1% to 30%, respectively. The total FUV luminosities of the galaxies in our sample are comparable (but slightly lower) to those in Ly α emitter samples at high redshift, but the Ly α luminosities are considerably lower.
- We find that Ly α is more extended than the UV continuum (as measured by Petrosian radius) in 35 out of the 39 galaxies with global Ly α emission. The distribution of Ly α emission in the galaxies tends to be more clumpy and irregular in the sources with low f_{esc} , but can be overall asymmetric also in galaxies with high f_{esc} . Comparing the Ly α maps to nebular extinction maps (H α /H β) we find that Ly α escape tends to happen along directions in the galaxies where there is less extinction.
- We investigate how the escape of Ly α depends on a number of galaxy properties, both stellar (mass, age, dust, and SFR quantities) and ISM (metallicity, O32, dust). We find that the escape fraction is strongly anti-correlated with extinction, both for stars and nebular gas. We also find a weak anti-correlation of f_{esc} with stellar mass and discuss various explanations for this. Neither SFR, specific SFR, or SFR surface density is correlated to f_{esc} in our study. The ionisation state of the ISM (as probed by the O32 ratio) in the galaxies seems not to be related to f_{esc} in a direct way, but we note that most of the galaxies with O32 < 1 have $f_{\text{esc}} < 10\%$.
- The anti-correlation of Ly α escape fraction with nebular extinction is strong, but shows substantial scatter. Fitting a log-linear relation to the measurements we find an intercept of $f_{\text{esc}}(E(B - V)_n = 0) = 0.075 \pm 0.019$ and a slope of 3.30 ± 0.73 . We compare the observations with the expected relation for a number of attenuation curves and find that simple dust screen models are too steep to explain the observations. The shallow slope we find is comparable to those found by other Ly α studies, in particular when the samples include also weak and dusty Ly α emitters. We conclude that the shallow slope found — with the observed f_{esc} being lower than expected at low $E(B - V)_n$, and higher than expected at high $E(B - V)_n$ — can be explained by a combination of radiative transfer effects and a clumpy dust geometry.
- The equivalent width of Ly α is strongly correlated to f_{esc} as found by multiple previous authors. We fit a linear function to the observed data points and find a relatively tight relation: $f_{\text{esc}} = (0.0040 \pm 0.00050 \cdot W_{\text{Ly}\alpha}) \pm 0.013$. However, the scatter around the relation is large and we discuss two different scenarios (high extinction and a non-standard ionisation production efficiency) which could cause individual sources to deviate from the relation. We then use this relation to provide an approximate dust corrected SFR calibration for Ly α luminosity which uses only $W_{\text{Ly}\alpha}$ to correct the luminosity for the non-zero escape fraction. When comparing the Ly α SFR estimate to dust corrected H α estimates for our galaxies we find a good agreement, but with large scatter (0.20 dex for the full sample, 0.16 dex for a sub-sample of galaxies with $E(B - V)_n < 0.3$).
- We characterize the aperture losses of Ly α in limited aperture spectroscopic observations by using stacked growth curves of our sample. We find that the losses can be quite severe for small slit widths or aperture sizes at certain redshift ranges, and that this needs to be taken into account when discussing results or planning new surveys.

The fully reduced data and maps are available to the community along with our measurements as a High Level Science Product at MAST ([10.17909/pbe1-m743](https://doi.org/10.17909/pbe1-m743)). The Ly α images for our reference sample, and the supporting observations can thus be used to interpret and compare to future Ly α observations in both nearby and very distant galaxies.

This work has been supported by the Swedish National Space Agency (SNSA). M.M. acknowledges the support of the Swedish Research Council, Vetenskapsrådet (grant 2019-00502). JMMH is funded by Spanish MCIN/AEI/10.13039/501100011033 grant PID2019-107061GB-C61. The Cosmic Dawn Center (DAWN) is funded by the Danish National Research Foundation under grant No. 140.

This research is based on observations made with the NASA/ESA Hubble Space Telescope obtained from the Space Telescope Science Institute, which is operated by the Association of Universities for Research in Astronomy, Inc., under NASA contract NAS 5-26555. These observations are associated with programs 12310, 13483, 13027, 14923, and 13656. The research has also made use of the NASA/IPAC Infrared Science Archive, which is funded by the National Aeronautics and Space Administration and operated by the California Institute of Technology.

Facilities: Hubble Space Telescope (ACS, WFC3), MAST, IRSA

Software: Astropy (Astropy Collaboration et al. 2013), Drizzlepac (Gonzaga et al. 2012), Matplotlib (Hunter 2007), SCOOP (Hold-Geoffroy et al. 2014), LA-Cosmic (van Dokkum 2001), TinyTim (Krist et al. 2011), LaXS (Hayes et al. 2014; Östlin et al. 2014), Photutils (Bradley et al. 2022)

APPENDIX

A. HST FILTERS USED FOR EACH GALAXY

Table 7. HST imaging for individual galaxies

ID	Ly α (SBC)	H α (UVIS/WFC)	H β (UVIS/WFC)	FUV cont. (SBC)	UV/optical cont. (UVIS/WFC)
(1)	(2)	(3)	(4)	(5)	(6)
LARS01	F125LP	UVIS/F673N	UVIS/F502N	F140LP, F150LP	UVIS/F336W, UVIS/F438W, UVIS/F775W
LARS02	F125LP	UVIS/F673N	UVIS/F502N	F140LP, F150LP	UVIS/F336W, UVIS/F438W, UVIS/F775W
LARS03	F125LP	UVIS/F673N	UVIS/F502N	F140LP, F150LP	UVIS/F336W, WFC/F435W, WFC/F814W
LARS04	F125LP	UVIS/F673N	UVIS/F502N	F140LP, F150LP	UVIS/F336W, UVIS/F438W, UVIS/F775W
LARS05	F125LP	UVIS/F673N	UVIS/F502N	F140LP, F150LP	UVIS/F336W, UVIS/F438W, UVIS/F775W
LARS06	F125LP	UVIS/F673N	UVIS/F502N	F140LP, F150LP	UVIS/F336W, UVIS/F438W, UVIS/F775W
LARS07	F125LP	WFC/FR656N	WFC/F502N	F140LP, F150LP	UVIS/F336W, UVIS/F438W, UVIS/F775W
LARS08	F125LP	WFC/FR656N	WFC/F502N	F140LP, F150LP	UVIS/F336W, UVIS/F438W, UVIS/F775W
LARS09	F125LP	WFC/FR716N	WFC/FR505N	F140LP, F150LP	UVIS/F336W, UVIS/F438W, UVIS/F775W
LARS10	F125LP	WFC/FR716N	WFC/FR505N	F140LP, F150LP	UVIS/F336W, UVIS/F438W, UVIS/F775W
LARS11	F125LP	WFC/FR716N	WFC/FR551N	F140LP, F150LP	UVIS/F336W, UVIS/F438W, UVIS/F775W
LARS12	F125LP	WFC/FR716N	WFC/FR551N	F140LP, F150LP	UVIS/F336W, UVIS/F438W, UVIS/F775W
LARS13	F140LP	WFC/FR782N	WFC/FR551N	F150LP	UVIS/F390W, UVIS/F475W, UVIS/F850LP
LARS14	F140LP	WFC/FR782N	WFC/FR551N	F150LP	UVIS/F390W, UVIS/F475W, WFC/F850LP
ELARS01	F125LP	UVIS/F673N	UVIS/F502N	F140LP, F150LP	UVIS/F336W, WFC/F435W, WFC/F814W
ELARS02	F125LP	UVIS/F680N	UVIS/FQ508N	F140LP, F150LP	UVIS/F336W, UVIS/F438W, UVIS/F775W
ELARS03	F125LP	UVIS/F673N	UVIS/F502N	F140LP, F150LP	UVIS/F336W, UVIS/F438W, UVIS/F775W
ELARS04	F125LP	UVIS/F673N	UVIS/F502N	F140LP, F150LP	UVIS/F336W, UVIS/F438W, UVIS/F775W
ELARS05	F125LP	UVIS/F673N	UVIS/F502N	F140LP, F150LP	UVIS/F336W, UVIS/F438W, UVIS/F775W
ELARS06	F125LP	UVIS/F673N	UVIS/F502N	F140LP, F150LP	UVIS/F336W, UVIS/F438W, UVIS/F775W
ELARS07	F125LP	UVIS/F673N	UVIS/F502N	F140LP, F150LP	UVIS/F336W, UVIS/F438W, UVIS/F775W
ELARS08	F125LP	UVIS/F673N	UVIS/F502N	F140LP, F150LP	UVIS/F336W, UVIS/F438W, UVIS/F775W
ELARS09	F125LP	UVIS/F673N	UVIS/F502N	F140LP, F150LP	UVIS/F336W, UVIS/F438W, UVIS/F775W
ELARS10	F125LP	UVIS/F673N	UVIS/F502N	F140LP, F150LP	UVIS/F336W, UVIS/F438W, UVIS/F775W
ELARS11	F125LP	UVIS/F673N	UVIS/F502N	F140LP, F150LP	UVIS/F336W, UVIS/F438W, UVIS/F775W
ELARS12	F125LP	UVIS/F673N	UVIS/F502N	F140LP, F150LP	UVIS/F336W, UVIS/F438W, UVIS/F775W
ELARS13	F125LP	UVIS/F673N	UVIS/F502N	F140LP, F150LP	UVIS/F336W, UVIS/F438W, UVIS/F775W
ELARS14	F125LP	UVIS/F673N	UVIS/F502N	F140LP, F150LP	UVIS/F336W, UVIS/F438W, UVIS/F775W
ELARS15	F125LP	UVIS/F673N	UVIS/F502N	F140LP, F150LP	UVIS/F336W, UVIS/F438W, UVIS/F775W
ELARS16	F125LP	UVIS/F673N	UVIS/F502N	F140LP, F150LP	UVIS/F336W, UVIS/F438W, UVIS/F775W
ELARS17	F125LP	UVIS/F673N	UVIS/F502N	F140LP, F150LP	UVIS/F336W, UVIS/F438W, UVIS/F775W
ELARS18	F125LP	UVIS/F673N	UVIS/F502N	F140LP, F150LP	UVIS/F336W, UVIS/F438W, UVIS/F775W
ELARS19	F125LP	UVIS/F673N	UVIS/F502N	F140LP, F150LP	UVIS/F336W, UVIS/F438W, UVIS/F775W
ELARS20	F125LP	UVIS/F673N	UVIS/F502N	F140LP, F150LP	UVIS/F336W, UVIS/F438W, UVIS/F775W
ELARS21	F125LP	UVIS/F673N	UVIS/F502N	F140LP, F150LP	UVIS/F336W, UVIS/F438W, UVIS/F775W
ELARS22	F125LP	UVIS/F680N	UVIS/FQ508N	F140LP, F150LP	UVIS/F336W, UVIS/F438W, UVIS/F775W
ELARS23	F125LP	UVIS/F680N	UVIS/FQ508N	F140LP, F150LP	UVIS/F336W, UVIS/F438W, UVIS/F775W
ELARS24	F125LP	UVIS/F680N	UVIS/FQ508N	F140LP, F150LP	UVIS/F336W, UVIS/F438W, UVIS/F775W
ELARS25	F125LP	UVIS/F680N	UVIS/FQ508N	F140LP, F150LP	UVIS/F336W, UVIS/F438W, UVIS/F775W
ELARS26	F125LP	UVIS/F680N	UVIS/FQ508N	F140LP, F150LP	UVIS/F336W, UVIS/F438W, UVIS/F775W
ELARS27	F125LP	UVIS/F680N	UVIS/FQ508N	F140LP, F150LP	UVIS/F336W, UVIS/F438W, UVIS/F775W
ELARS28	F125LP	UVIS/F680N	UVIS/FQ508N	F140LP, F150LP	UVIS/F336W, UVIS/F438W, UVIS/F775W
Tol1214	F125LP	UVIS/F680N	UVIS/F502N	F140LP, F150LP	UVIS/F336W, UVIS/F438W, UVIS/F775W
Tol1247	F125LP	UVIS/FQ674N	WFC/FR505N	F140LP	UVIS/F336W, UVIS/F438W, UVIS/F775W
J1156	F140LP	WFC/FR782N	WFC/FR601N	F150LP, F165LP	UVIS/F390W, UVIS/F475W, UVIS/F850LP

NOTE—The filter columns shows the instruments and filters used.

B. POINT SPREAD FUNCTION MATCHING

B.1. Building PSF models

Accurate PSF models are available for most of the filters in HST instruments, but some of these only cover the inner parts of the PSF. In order to correctly estimate low surface brightness emission of Ly α using SBC we need match the PSF over a larger area than what is usually done. For the study reported in this paper we thus make custom models that reach a radius of at least 1'' (25 pixels for the resampled pixel scale in use). In Figure 18 we show models for a selection of filters used.

Models for the optical (ACS/WFC and WFC3/UVIS) filters were generated by adding a synthetic point source to individual reduced data frames, drizzling these using the same procedure as for the science frames, and then cutting out a thumbnail image of the PSF which was then properly background subtracted and normalized. The synthetic point source used for this comes from the *TinyTim* software, which is able to produce models out to the needed radius, and each individual frame has the correct defocus parameter and position on chip (we use the center of the galaxy) set for the model. We thus obtain one PSF model per filter and galaxy which has undergone the same treatment (drizzling and distortion correction) as the real data.

For ACS/SBC the models from *TinyTim* are inaccurate in the wings and are therefore unusable for the matching required in this study. Instead we use HST calibration data targeting the stellar cluster NGC 6681. We drizzle this data to the same pixel scale as the one used in our data set (0.04'' per pixel), find sufficiently

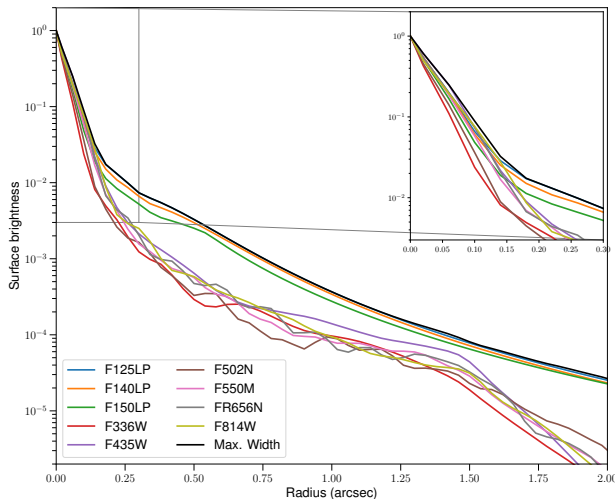


Figure 18. PSF models for a selection of filters.

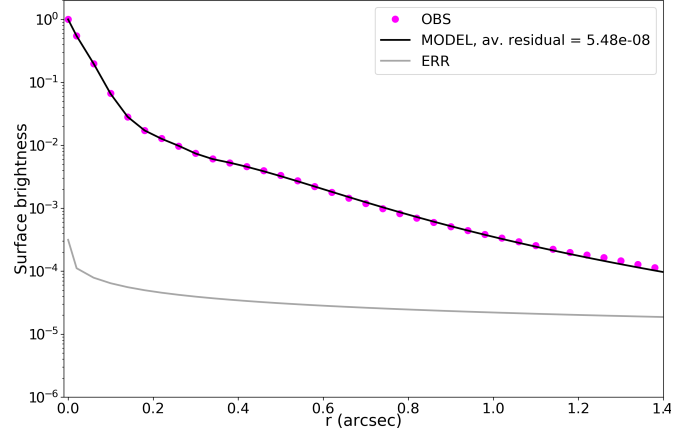


Figure 19. Best fit PSF model for the SBC F125LP filter. Observed data points come from a stack of stars in NGC 6681. The average residual for the observed data points is given in the legend.

isolated stars (roughly 50 stars) in the frame and fit a 2D model to them, making sure to subtract background. This is done iteratively and nearby stars that may affect the fit are removed from the image before the next pass is done. The model that provides the best fit to the SBC PSF consists of three components: (i) a Moffat model with seven free parameters, including the center coordinates and ellipticity, (ii) a Gaussian model with three free parameters, and (iii) a radially symmetric 4th order polynomial function. The Moffat function dominates in the center and the polynomial function in the outer parts. The Gaussian function is needed to correctly characterize the observed bump in the SBC PSF wings at a radius of $\sim 0.5''$. An example of a SBC PSF model fit is shown in Figure 19.

A number of different functions have been tried to find a suitable model for the SBC filters, and this is by far the best option we have found. Another option would be to use a thumbnail of stacked stars directly, but the resulting PSF model is then too noisy to be used in the PSF matching code. It should be noted that the PSF models for SBC are not dependent on defocus, nor location on chip, they are instead an average model per filter that we use for all galaxies. The uncertainty resulting from not taking these second order effects into account is negligible compared to the inaccuracy found for the SBC *TinyTim* models. Note that, somewhat unintuitively, the bluest SBC filter (F125LP for most of the galaxies) has the widest PSF in terms of power contained in the wings.

From the set of PSF models for a given galaxy (one per filter) we construct a maximum width 2D PSF model by finding the maximum value per pixel in the set of normalized models. This is then the PSF model that all of

the filters are later on matched to. We have found that this step is necessary to limit the appearance of convolution artifacts in the matching kernel. The maximum width PSF model is generally dominated by the reddest filter in the center regions, and by the bluest SBC filter in the wings.

B.2. The PSF matching technique

Initial attempts to match the PSFs from FUV to red optical using a single Gaussian convolution kernel showed very poor results, in particular in the wings. The reason for this is the non-standard shape of the SBC PSF, which is very narrow in the center but has strong extended wings. Motivated by this we have developed a matching tool with a more general kernel base, which has the freedom to correctly find the optimum matching solution also for complicated PSFs. We base our algorithm on the work of [Becker et al. \(2012\)](#), who use a convolution kernel built from a linear combination of multiple delta functions (one per pixel in the kernel). A kernel of this type is shown to be very powerful in finding an optimal matching solution, but is very sensitive to noise (both in the data and numerical), due to the high number of degrees of freedom in finding the matching kernel. The authors address this issue by adding regularisation to the kernel solving. They show that moderate regularisation makes it possible to find robust matching kernels without significant loss of accuracy.

Following [Becker et al. \(2012\)](#) the expression for the kernel we use is:

$$K_{i,j}(u, v) = \delta(u - i)\delta(v - j), \quad (\text{B1})$$

which represents one delta function per kernel pixel. The final convolution kernel is then modelled as a linear combination of these basis functions, $K(u, v) = \sum_{i,j} a_{i,j} K_{i,j}(u, v)$. The convolution of the input PSF model (\mathbf{R}) with the kernel basis functions can then be written as $\mathbf{C} = \mathbf{R} \otimes K_{i,j}$. We then want to find the optimum matching kernel (i.e., solve for $a_{i,j}$) that best transforms the input model into the maximum width filter PSF (\mathbf{S}). This is done by solving the following matrix equation:

$$\mathbf{b} = \mathbf{M}_\lambda \mathbf{a} = (\mathbf{M} + \lambda_r \mathbf{H}) \mathbf{a}, \quad (\text{B2})$$

where $\mathbf{b} = \mathbf{C}^T \mathbf{\Sigma}^{-1} \mathbf{S}$, $\mathbf{M} = \mathbf{C}^T \mathbf{\Sigma}^{-1} \mathbf{C}$ and $\lambda_r \mathbf{H}$ is the regularisation term. For details of the matrix equation and definitions refer to [Becker et al. \(2012\)](#). The best value to use for λ_r depends on the input models and we run tests to find a good number that limits the amount of over-fitting artifacts in the matched PSF models while still keeping the overall matching residuals low. For the models used in this project we have

found that $\lambda_r \sim 10^{-5}$ is usually good, but for some of the galaxies a higher regularisation strength is needed (up to 10^{-4}). The algorithm is implemented as a parallelised python code which can find the optimum matching kernel for PSF models using a given kernel size. The number of operations performed by the code scale with kernel size to the power of three, which means that this size should be kept as low as possible. For our data set we have found that a kernel size of 40 pixels ($1.6''$, corresponding to a radius of $\sim 0.8''$) is adequate to get accurate matching results while keeping the computing time reasonable.

In Figure 20 we show example relative residual maps $((\mathbf{R} - \mathbf{S})/\mathbf{S})$ of comparing individual filter models (using the same filters as the PSF models displayed in Figure 18) to the maximum width model without performing any PSF matching. As expected the residuals are very strong in the wings of the optical filter PSFs, and quite substantial also in the core. The SBC filters look slightly better, but the core regions are problematic also there. In Figure 21 we show the result of applying the optimum PSF matching with a kernel size of 40 pixels. This changes the residual maps drastically, decreasing the average residual by a factor ~ 10 – 20 (depending on the individual filter).

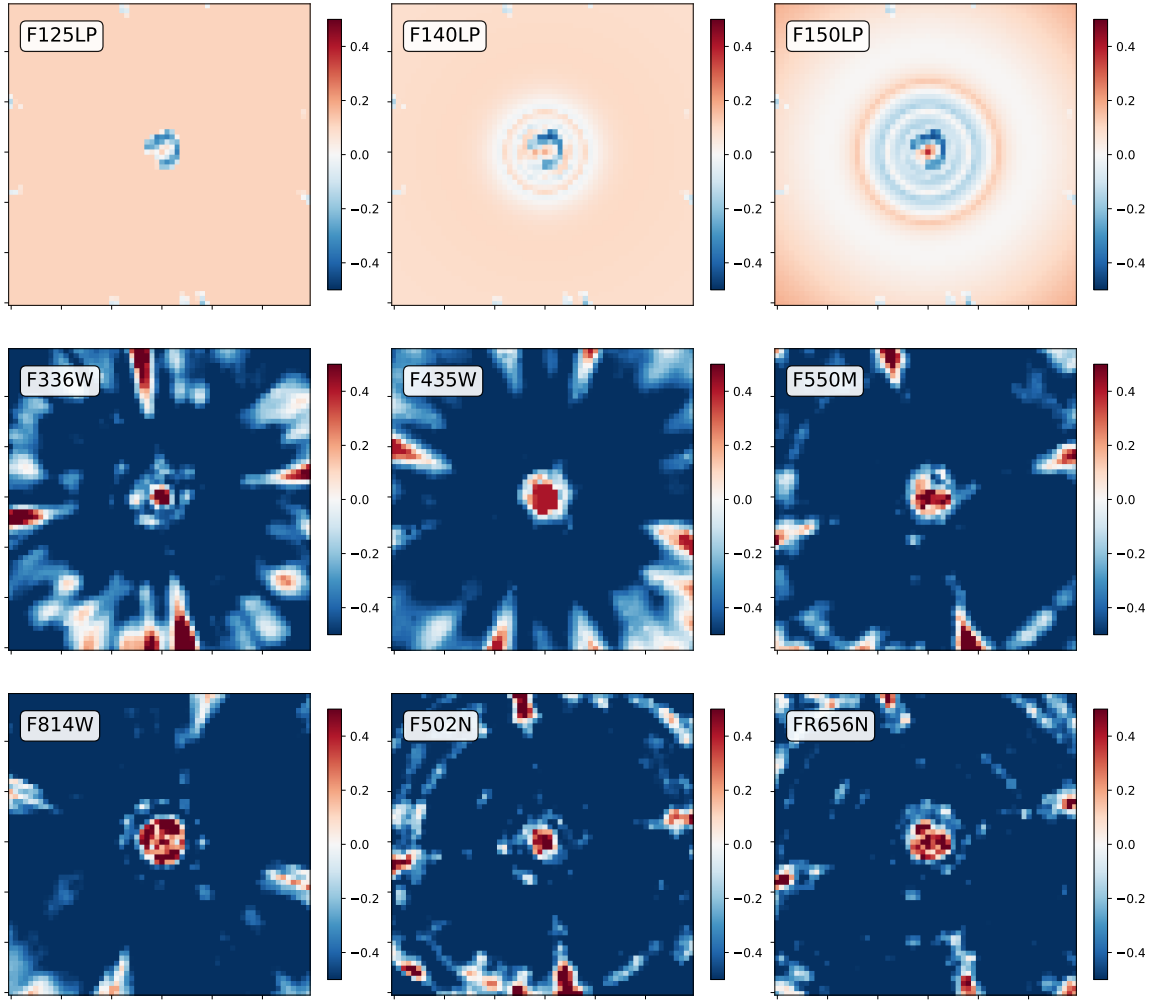


Figure 20. Relative residual of PSF models compared to a maximum width PSF (filter setup and individual models from the ELARS01 data set). This figure shows residuals without performing any matching.

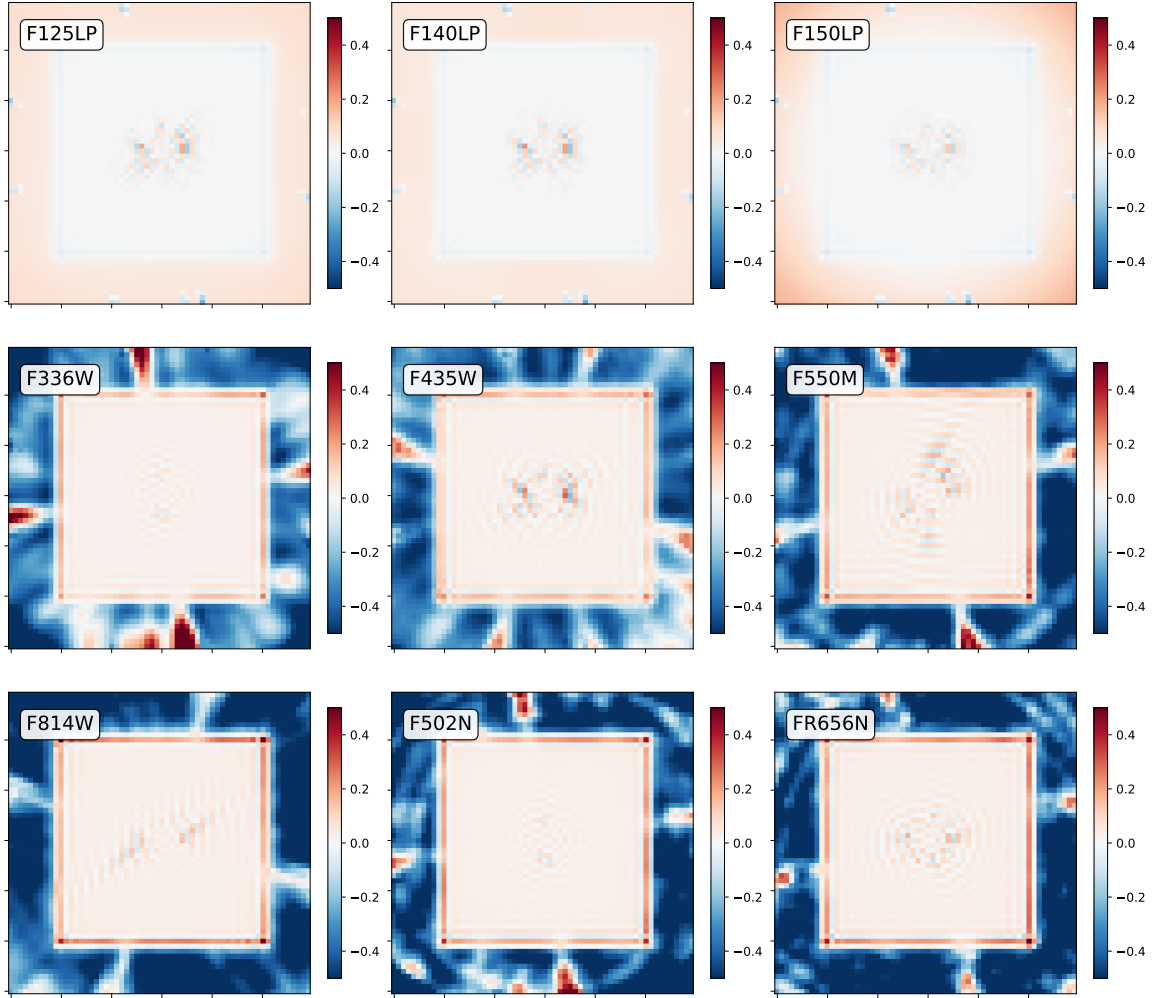


Figure 21. Relative residual of PSF models after matching them to the maximum width PSF using the technique described in this paper.

C. SURFACE BRIGHTNESS, $W_{\text{Ly}\alpha}$, AND f_{esc} PROFILES

This section contains tables of surface brightness, $W_{\text{Ly}\alpha}$, and f_{esc} profiles for the galaxies. Note that we have elected to use the same number of significant digits for all the entries, even if the errors are sometimes large. The dynamic range of the measurements is very large, and the errors depend both on the measurements and the fitting uncertainties. This means that the errors are often very small far away from the bright galaxy centres, and the number of significant digits have been chosen to be able to show these errors.

Table 8. Surface brightness, $W_{\text{Ly}\alpha}$, and f_{esc} profiles

Galaxy ID	r	SB_{FUV}	$\text{SB}_{\text{H}\alpha}$	$\text{SB}_{\text{Ly}\alpha}$	$W_{\text{Ly}\alpha}$	f_{esc}
	kpc	$10^{39} \text{erg/s}/\text{\AA}/\text{kpc}^2$	$10^{40} \text{erg/s}/\text{kpc}^2$	$10^{40} \text{erg/s}/\text{kpc}^2$	\AA	
(1)	(2)	(3)	(4)	(5)	(6)	(7)
LARS01	0.10	70.99200 ^{0.21275} _{0.29892}	38.51040 ^{0.32427} _{0.19535}	158.01700 ^{8.49713} _{6.68443}	22.25840 ^{1.10507} _{0.98618}	0.42986 ^{0.01997} _{0.01997}
LARS01	0.33	13.05120 ^{0.03799} _{0.04493}	28.19240 ^{0.06018} _{0.06222}	36.39420 ^{0.82643} _{1.09275}	25.86760 ^{0.54082} _{0.47232}	0.16459 ^{0.00309} _{0.00309}
LARS01	0.56	3.83610 ^{0.01055} _{0.01470}	10.98370 ^{0.02638} _{0.02848}	12.20720 ^{0.24303} _{0.29510}	27.53570 ^{0.45634} _{0.42431}	0.13933 ^{0.00251} _{0.00251}
LARS01	0.78	1.99101 ^{0.00827} _{0.00719}	6.78822 ^{0.01633} _{0.02206}	8.20741 ^{0.18546} _{0.18433}	30.00710 ^{0.37692} _{0.41020}	0.13022 ^{0.00187} _{0.00187}
LARS01	1.01	1.31142 ^{0.00459} _{0.00568}	5.01932 ^{0.01185} _{0.01414}	5.55087 ^{0.13061} _{0.11409}	31.70100 ^{0.38338} _{0.34369}	0.12243 ^{0.00139} _{0.00139}
LARS01	1.24	0.70184 ^{0.00375} _{0.00446}	3.16691 ^{0.00720} _{0.01451}	3.01222 ^{0.07880} _{0.07796}	32.64860 ^{0.37942} _{0.31905}	0.11510 ^{0.00124} _{0.00124}
LARS01	1.47	0.48885 ^{0.00262} _{0.00377}	1.29346 ^{0.00739} _{0.00808}	2.02582 ^{0.06760} _{0.07115}	33.22940 ^{0.31417} _{0.35021}	0.11564 ^{0.00136} _{0.00136}
LARS01	1.69	0.38911 ^{0.00254} _{0.00263}	0.76669 ^{0.00729} _{0.00601}	1.47740 ^{0.06151} _{0.05702}	33.50380 ^{0.35916} _{0.36378}	0.11658 ^{0.00131} _{0.00131}
LARS01	1.92	0.24877 ^{0.00193} _{0.00191}	0.56295 ^{0.00503} _{0.00470}	1.08880 ^{0.03709} _{0.03840}	33.92070 ^{0.37290} _{0.35802}	0.11715 ^{0.00125} _{0.00125}
LARS01	2.15	0.16905 ^{0.00162} _{0.00192}	0.42472 ^{0.00466} _{0.00481}	0.95145 ^{0.04196} _{0.03103}	34.59480 ^{0.34963} _{0.31824}	0.11843 ^{0.00125} _{0.00125}
LARS01	2.38	0.13984 ^{0.00142} _{0.00167}	0.56876 ^{0.00442} _{0.00374}	0.85177 ^{0.04317} _{0.03095}	35.30470 ^{0.29758} _{0.38651}	0.11819 ^{0.00136} _{0.00136}
LARS01	2.60	0.10606 ^{0.00140} _{0.00127}	0.43856 ^{0.00355} _{0.00408}	0.65158 ^{0.02706} _{0.03461}	35.88010 ^{0.29408} _{0.36342}	0.11771 ^{0.00130} _{0.00130}
LARS01	2.83	0.10035 ^{0.00143} _{0.00142}	0.26576 ^{0.00410} _{0.00252}	0.57028 ^{0.03272} _{0.02338}	36.34590 ^{0.34410} _{0.35660}	0.11874 ^{0.00129} _{0.00129}
LARS01	3.06	0.10276 ^{0.00120} _{0.00162}	0.28880 ^{0.00460} _{0.00203}	0.46350 ^{0.03008} _{0.02990}	36.55690 ^{0.36894} _{0.33116}	0.11906 ^{0.00129} _{0.00129}
LARS01	3.29	0.06105 ^{0.00114} _{0.00107}	0.16322 ^{0.00358} _{0.00314}	0.39626 ^{0.02541} _{0.01937}	36.98720 ^{0.33533} _{0.33296}	0.12001 ^{0.00126} _{0.00126}
LARS01	3.51	0.04505 ^{0.00081} _{0.00081}	0.11332 ^{0.00277} _{0.00277}	0.36863 ^{0.02556} _{0.02067}	37.51910 ^{0.35437} _{0.33064}	0.12177 ^{0.00135} _{0.00135}
LARS01	3.74	0.03694 ^{0.00091} _{0.00103}	0.09549 ^{0.00212} _{0.00297}	0.34906 ^{0.02507} _{0.02205}	38.10440 ^{0.35960} _{0.42559}	0.12314 ^{0.00137} _{0.00137}
LARS01	3.97	0.02005 ^{0.00094} _{0.00082}	0.05743 ^{0.00252} _{0.00261}	0.28614 ^{0.02067} _{0.01302}	38.72050 ^{0.36458} _{0.41239}	0.12436 ^{0.00132} _{0.00132}
LARS01	4.20	0.01615 ^{0.00077} _{0.00079}	0.04557 ^{0.00257} _{0.00232}	0.24280 ^{0.01844} _{0.01352}	39.27850 ^{0.37909} _{0.40120}	0.12549 ^{0.00137} _{0.00137}
LARS01	4.42	0.01513 ^{0.00082} _{0.00073}	0.03664 ^{0.00274} _{0.00231}	0.22110 ^{0.01709} _{0.01102}	39.80430 ^{0.40556} _{0.39713}	0.12631 ^{0.00137} _{0.00137}
LARS01	4.65	0.02175 ^{0.00060} _{0.00071}	0.03915 ^{0.00217} _{0.00200}	0.18782 ^{0.01392} _{0.01542}	40.14830 ^{0.47300} _{0.40845}	0.12664 ^{0.00144} _{0.00144}
LARS01	4.88	0.02118 ^{0.00066} _{0.00061}	0.03577 ^{0.00185} _{0.00249}	0.16818 ^{0.01260} _{0.01297}	40.44280 ^{0.47217} _{0.40367}	0.12682 ^{0.00144} _{0.00144}
LARS01	5.11	0.01575 ^{0.00069} _{0.00068}	0.03014 ^{0.00234} _{0.00237}	0.14806 ^{0.01234} _{0.01511}	40.75410 ^{0.44259} _{0.39275}	0.12685 ^{0.00137} _{0.00137}
LARS01	5.33	0.01151 ^{0.00068} _{0.00055}	0.01777 ^{0.00249} _{0.00199}	0.11454 ^{0.01025} _{0.01322}	41.01380 ^{0.41764} _{0.37782}	0.12789 ^{0.00127} _{0.00127}
LARS01	5.56	0.01064 ^{0.00062} _{0.00053}	0.01521 ^{0.00209} _{0.00190}	0.09811 ^{0.01347} _{0.01009}	41.23110 ^{0.42272} _{0.37352}	0.12881 ^{0.00127} _{0.00127}
LARS01	5.79	0.00773 ^{0.00043} _{0.00052}	0.01026 ^{0.00176} _{0.00229}	0.09727 ^{0.01223} _{0.01083}	41.50220 ^{0.45148} _{0.38337}	0.12986 ^{0.00135} _{0.00135}
LARS01	6.02	0.00674 ^{0.00049} _{0.00046}	0.00840 ^{0.00181} _{0.00166}	0.08448 ^{0.00951} _{0.01706}	41.74500 ^{0.42879} _{0.40574}	0.13082 ^{0.00140} _{0.00140}
LARS01	6.24	0.00600 ^{0.00042} _{0.00048}	0.00742 ^{0.00189} _{0.00157}	0.06429 ^{0.01176} _{0.00996}	41.91980 ^{0.41685} _{0.41548}	0.13155 ^{0.00141} _{0.00141}
LARS01	6.47	0.00514 ^{0.00043} _{0.00047}	0.00801 ^{0.00200} _{0.00184}	0.05201 ^{0.01151} _{0.01377}	42.06010 ^{0.42333} _{0.42472}	0.13212 ^{0.00148} _{0.00148}
LARS01	6.70	0.00485 ^{0.00046} _{0.00037}	0.00783 ^{0.00208} _{0.00182}	0.04873 ^{0.01181} _{0.01241}	42.19510 ^{0.39695} _{0.45770}	0.13266 ^{0.00156} _{0.00156}
LARS02	0.10	17.01260 ^{0.09033} _{0.12730}	25.70370 ^{0.22320} _{0.17739}	< 2.83704	< 1.63848	< 0.00958
LARS02	0.38	1.83723 ^{0.01042} _{0.01057}	5.91272 ^{0.02139} _{0.03036}	7.51897 ^{0.28318} _{0.17952}	22.34760 ^{1.01958} _{1.15808}	0.09356 ^{0.00451} _{0.00451}
LARS02	0.65	0.96809 ^{0.00567} _{0.00461}	1.97144 ^{0.01040} _{0.01155}	2.94720 ^{0.11996} _{0.11656}	25.59460 ^{0.82924} _{1.09964}	0.10887 ^{0.00431} _{0.00431}
LARS02	0.93	0.52246 ^{0.00399} _{0.00492}	0.86781 ^{0.00474} _{0.00516}	2.23548 ^{0.09785} _{0.08832}	29.88720 ^{0.83957} _{0.88144}	0.13106 ^{0.00382} _{0.00382}
LARS02	1.21	0.41289 ^{0.00235} _{0.00350}	0.81836 ^{0.00759} _{0.00491}	2.07652 ^{0.05451} _{0.07493}	34.17820 ^{0.70548} _{0.97234}	0.15393 ^{0.00411} _{0.00411}

NOTE—Table 8 is published in its entirety in machine-readable format. A portion (profiles for LARS01 and part of LARS02) is shown here for guidance regarding its form and content.

REFERENCES

- Adams, J. J., Blanc, G. A., Hill, G. J., et al. 2011, *ApJS*, 192, 5, doi: [10.1088/0067-0049/192/1/5](https://doi.org/10.1088/0067-0049/192/1/5)
- Akritis, M. G., Murphy, S. A., & LaValley, M. P. 1995, *Journal of the American Statistical Association*, 90, 170. <http://www.jstor.org/stable/2291140>
- Aller, L. H. 1984, *Physics of thermal gaseous nebulae*, doi: [10.1007/978-94-010-9639-3](https://doi.org/10.1007/978-94-010-9639-3)
- Anders, P., & Fritze-v. Alvensleben, U. 2003, *A&A*, 401, 1063, doi: [10.1051/0004-6361/20030151](https://doi.org/10.1051/0004-6361/20030151)
- Astropy Collaboration, Robitaille, T. P., Tollerud, E. J., et al. 2013, *A&A*, 558, A33, doi: [10.1051/0004-6361/201322068](https://doi.org/10.1051/0004-6361/201322068)
- Atek, H., Kunth, D., Schaerer, D., et al. 2009, *A&A*, 506, L1, doi: [10.1051/0004-6361/200912787](https://doi.org/10.1051/0004-6361/200912787)
- . 2014, *A&A*, 561, A89, doi: [10.1051/0004-6361/201321519](https://doi.org/10.1051/0004-6361/201321519)
- Baldwin, J. A., Phillips, M. M., & Terlevich, R. 1981, *PASP*, 93, 5, doi: [10.1086/130766](https://doi.org/10.1086/130766)
- Becker, A. C., Homrighausen, D., Connolly, A. J., et al. 2012, *MNRAS*, 425, 1341, doi: [10.1111/j.1365-2966.2012.21542.x](https://doi.org/10.1111/j.1365-2966.2012.21542.x)
- Blanton, M. R., Dalcanton, J., Eisenstein, D., et al. 2001, *AJ*, 121, 2358, doi: [10.1086/320405](https://doi.org/10.1086/320405)
- Bradley, L., Sipőcz, B., Robitaille, T., et al. 2022, *astropy/photutils: 1.5.0*, Zenodo, Zenodo, doi: [10.5281/zenodo.6825092](https://doi.org/10.5281/zenodo.6825092)
- Bridge, J. S., Hayes, M., Melinder, J., et al. 2018, *ApJ*, 852, 9, doi: [10.3847/1538-4357/aa9932](https://doi.org/10.3847/1538-4357/aa9932)
- Brinchmann, J., Charlot, S., White, S. D. M., et al. 2004, *MNRAS*, 351, 1151, doi: [10.1111/j.1365-2966.2004.07881.x](https://doi.org/10.1111/j.1365-2966.2004.07881.x)
- Calzetti, D., Armus, L., Bohlin, R. C., et al. 2000, *ApJ*, 533, 682, doi: [10.1086/308692](https://doi.org/10.1086/308692)
- Calzetti, D., Kinney, A. L., & Storchi-Bergmann, T. 1994, *ApJ*, 429, 582, doi: [10.1086/174346](https://doi.org/10.1086/174346)
- Cardelli, J. A., Clayton, G. C., & Mathis, J. S. 1989, *ApJ*, 345, 245, doi: [10.1086/167900](https://doi.org/10.1086/167900)
- Casey, C. M., Narayanan, D., & Cooray, A. 2014, *PhR*, 541, 45, doi: [10.1016/j.physrep.2014.02.009](https://doi.org/10.1016/j.physrep.2014.02.009)
- Cowie, L. L., Barger, A. J., & Hu, E. M. 2011, *ApJ*, 738, 136, doi: [10.1088/0004-637X/738/2/136](https://doi.org/10.1088/0004-637X/738/2/136)
- Cowie, L. L., & Hu, E. M. 1998, *AJ*, 115, 1319, doi: [10.1086/300309](https://doi.org/10.1086/300309)
- Davidson, A. F., Hartig, G. F., & Fastie, W. G. 1977, *Nature*, 269, 203, doi: [10.1038/269203a0](https://doi.org/10.1038/269203a0)
- Dijkstra, M. 2014, *PASA*, 31, e040, doi: [10.1017/pasa.2014.33](https://doi.org/10.1017/pasa.2014.33)
- . 2017, *arXiv e-prints*, arXiv:1704.03416. <https://arxiv.org/abs/1704.03416>
- Domínguez Sánchez, H., Mignoli, M., Pozzi, F., et al. 2012, *MNRAS*, 426, 330, doi: [10.1111/j.1365-2966.2012.21710.x](https://doi.org/10.1111/j.1365-2966.2012.21710.x)
- Duval, F., Östlin, G., Hayes, M., et al. 2016, *A&A*, 587, A77, doi: [10.1051/0004-6361/201526876](https://doi.org/10.1051/0004-6361/201526876)
- Erb, D. K., Steidel, C. C., Trainor, R. F., et al. 2014, *ApJ*, 795, 33, doi: [10.1088/0004-637X/795/1/33](https://doi.org/10.1088/0004-637X/795/1/33)
- Flury, S. R., Jaskot, A. E., Ferguson, H. C., et al. 2022, *ApJS*, 260, 1, doi: [10.3847/1538-4365/ac5331](https://doi.org/10.3847/1538-4365/ac5331)
- Fricke, K. J., Izotov, Y. I., Papaderos, P., Guseva, N. G., & Thuan, T. X. 2001, *AJ*, 121, 169, doi: [10.1086/318016](https://doi.org/10.1086/318016)
- Fruchter, A. S., & Hook, R. N. 2002, *PASP*, 114, 144, doi: [10.1086/338393](https://doi.org/10.1086/338393)
- Giavalisco, M., Koratkar, A., & Calzetti, D. 1996, *ApJ*, 466, 831, doi: [10.1086/177557](https://doi.org/10.1086/177557)
- Gonzaga, S., Hack, W., Fruchter, A., & Mack, J. 2012, *The DrizzlePac Handbook*
- Gronke, M., & Dijkstra, M. 2016, *ApJ*, 826, 14, doi: [10.3847/0004-637X/826/1/14](https://doi.org/10.3847/0004-637X/826/1/14)
- Guaita, L., Melinder, J., Hayes, M., et al. 2015, *A&A*, 576, A51, doi: [10.1051/0004-6361/201425053](https://doi.org/10.1051/0004-6361/201425053)
- Guseva, N. G., Izotov, Y. I., Stasińska, G., et al. 2011, *A&A*, 529, A149, doi: [10.1051/0004-6361/201016291](https://doi.org/10.1051/0004-6361/201016291)
- Hayes, M. 2015, *PASA*, 32, e027, doi: [10.1017/pasa.2015.25](https://doi.org/10.1017/pasa.2015.25)
- Hayes, M., Melinder, J., Östlin, G., et al. 2016, *ApJ*, 828, 49, doi: [10.3847/0004-637X/828/1/49](https://doi.org/10.3847/0004-637X/828/1/49)
- Hayes, M., Östlin, G., Atek, H., et al. 2007, *MNRAS*, 382, 1465, doi: [10.1111/j.1365-2966.2007.12482.x](https://doi.org/10.1111/j.1365-2966.2007.12482.x)
- Hayes, M., Östlin, G., Mas-Hesse, J. M., & Kunth, D. 2009, *AJ*, 138, 911, doi: [10.1088/0004-6256/138/3/911](https://doi.org/10.1088/0004-6256/138/3/911)
- Hayes, M., Östlin, G., Mas-Hesse, J. M., et al. 2005, *A&A*, 438, 71, doi: [10.1051/0004-6361:20052702](https://doi.org/10.1051/0004-6361:20052702)
- Hayes, M., Schaerer, D., Östlin, G., et al. 2011, *ApJ*, 730, 8, doi: [10.1088/0004-637X/730/1/8](https://doi.org/10.1088/0004-637X/730/1/8)
- Hayes, M., Östlin, G., Schaerer, D., et al. 2010, *Nature*, 464, 562, doi: [10.1038/nature08881](https://doi.org/10.1038/nature08881)
- . 2013, *ApJL*, 765, L27, doi: [10.1088/2041-8205/765/2/L27](https://doi.org/10.1088/2041-8205/765/2/L27)
- Hayes, M., Östlin, G., Duval, F., et al. 2014, *ApJ*, 782, 6, doi: [10.1088/0004-637X/782/1/6](https://doi.org/10.1088/0004-637X/782/1/6)
- Heckman, T. M., Borthakur, S., Overzier, R., et al. 2011, *ApJ*, 730, 5, doi: [10.1088/0004-637X/730/1/5](https://doi.org/10.1088/0004-637X/730/1/5)
- Henry, A., Scarlata, C., Martin, C. L., & Erb, D. 2015, *ApJ*, 809, 19, doi: [10.1088/0004-637X/809/1/19](https://doi.org/10.1088/0004-637X/809/1/19)
- Herenz, E. C., Gruyters, P., Orlitova, I., et al. 2016, *A&A*, 587, A78, doi: [10.1051/0004-6361/201527373](https://doi.org/10.1051/0004-6361/201527373)
- Herenz, E. C., Urrutia, T., Wisotzki, L., et al. 2017, *A&A*, 606, A12, doi: [10.1051/0004-6361/201731055](https://doi.org/10.1051/0004-6361/201731055)

- Hold-Geoffroy, Y., Gagnon, O., & Parizeau, M. 2014, in Proceedings of the 2014 Annual Conference on Extreme Science and Engineering Discovery Environment, XSEDE '14 (New York, NY, USA: Association for Computing Machinery), doi: [10.1145/2616498.2616565](https://doi.org/10.1145/2616498.2616565)
- Hunter, J. D. 2007, Computing In Science & Engineering, 9, 90, doi: [10.1109/MCSE.2007.55](https://doi.org/10.1109/MCSE.2007.55)
- Izotov, Y. I., Schaerer, D., Worseck, G., et al. 2020, MNRAS, 491, 468, doi: [10.1093/mnras/stz3041](https://doi.org/10.1093/mnras/stz3041)
- Izotov, Y. I., Worseck, G., Schaerer, D., et al. 2018, MNRAS, 478, 4851, doi: [10.1093/mnras/sty1378](https://doi.org/10.1093/mnras/sty1378)
- Jaskot, A. E., Oey, M. S., Scarlata, C., & Dowd, T. 2017, ApJL, 851, L9, doi: [10.3847/2041-8213/aa9d83](https://doi.org/10.3847/2041-8213/aa9d83)
- Jensen, H., Laursen, P., Mellema, G., et al. 2013, MNRAS, 428, 1366, doi: [10.1093/mnras/sts116](https://doi.org/10.1093/mnras/sts116)
- Kelly, B. C. 2007, ApJ, 665, 1489, doi: [10.1086/519947](https://doi.org/10.1086/519947)
- Kennicutt, R. C., & Evans, N. J. 2012, ARA&A, 50, 531, doi: [10.1146/annurev-astro-081811-125610](https://doi.org/10.1146/annurev-astro-081811-125610)
- Kewley, L. J., & Dopita, M. A. 2002, ApJS, 142, 35, doi: [10.1086/341326](https://doi.org/10.1086/341326)
- Kimm, T., Blaizot, J., Garel, T., et al. 2019, MNRAS, 486, 2215, doi: [10.1093/mnras/stz989](https://doi.org/10.1093/mnras/stz989)
- Kornei, K. A., Shapley, A. E., Erb, D. K., et al. 2010, ApJ, 711, 693, doi: [10.1088/0004-637X/711/2/693](https://doi.org/10.1088/0004-637X/711/2/693)
- Krist, J. E., Hook, R. N., & Stoehr, F. 2011, in Society of Photo-Optical Instrumentation Engineers (SPIE) Conference Series, Vol. 8127, Optical Modeling and Performance Predictions V, ed. M. A. Kahan, 81270J, doi: [10.1117/12.892762](https://doi.org/10.1117/12.892762)
- Kroupa, P., Tout, C. A., & Gilmore, G. 1993, MNRAS, 262, 545, doi: [10.1093/mnras/262.3.545](https://doi.org/10.1093/mnras/262.3.545)
- Kunth, D., Leitherer, C., Mas-Hesse, J. M., Östlin, G., & Petrosian, A. 2003, ApJ, 597, 263, doi: [10.1086/378396](https://doi.org/10.1086/378396)
- Kunth, D., Mas-Hesse, J. M., Terlevich, E., et al. 1998, A&A, 334, 11. <https://arxiv.org/abs/astro-ph/9802253>
- Laursen, P., Duval, F., & Östlin, G. 2013, ApJ, 766, 124, doi: [10.1088/0004-637X/766/2/124](https://doi.org/10.1088/0004-637X/766/2/124)
- Laursen, P., Sommer-Larsen, J., & Andersen, A. C. 2009, ApJ, 704, 1640, doi: [10.1088/0004-637X/704/2/1640](https://doi.org/10.1088/0004-637X/704/2/1640)
- Laursen, P., Sommer-Larsen, J., Milvang-Jensen, B., Fynbo, J. P. U., & Razoumov, A. O. 2019, A&A, 627, A84, doi: [10.1051/0004-6361/201833645](https://doi.org/10.1051/0004-6361/201833645)
- Le Reste, A., Hayes, M., Cannon, J. M., et al. 2022, ApJ, 934, 69, doi: [10.3847/1538-4357/ac77ed](https://doi.org/10.3847/1538-4357/ac77ed)
- Leclercq, F., Bacon, R., Wisotzki, L., et al. 2017, A&A, 608, A8, doi: [10.1051/0004-6361/201731480](https://doi.org/10.1051/0004-6361/201731480)
- Leitherer, C., Schaerer, D., Goldader, J. D., et al. 1999, ApJS, 123, 3, doi: [10.1086/313233](https://doi.org/10.1086/313233)
- Malhotra, S., & Rhoads, J. E. 2004, ApJL, 617, L5, doi: [10.1086/427182](https://doi.org/10.1086/427182)
- Matthee, J., Sobral, D., Oteo, I., et al. 2016, MNRAS, 458, 449, doi: [10.1093/mnras/stw322](https://doi.org/10.1093/mnras/stw322)
- Meier, D. L., & Terlevich, R. 1981, ApJL, 246, L109, doi: [10.1086/183565](https://doi.org/10.1086/183565)
- Momose, R., Ouchi, M., Nakajima, K., et al. 2014, MNRAS, 442, 110, doi: [10.1093/mnras/stu825](https://doi.org/10.1093/mnras/stu825)
- Montero-Dorta, A. D., Bolton, A. S., Brownstein, J. R., et al. 2016, MNRAS, 461, 1131, doi: [10.1093/mnras/stw1352](https://doi.org/10.1093/mnras/stw1352)
- Nakajima, K., Fletcher, T., Ellis, R. S., Robertson, B. E., & Iwata, I. 2018, MNRAS, 477, 2098, doi: [10.1093/mnras/sty750](https://doi.org/10.1093/mnras/sty750)
- Natta, A., & Panagia, N. 1984, ApJ, 287, 228, doi: [10.1086/162681](https://doi.org/10.1086/162681)
- Neufeld, D. A. 1991, ApJL, 370, L85, doi: [10.1086/185983](https://doi.org/10.1086/185983)
- Östlin, G., Hayes, M., Kunth, D., et al. 2009, AJ, 138, 923, doi: [10.1088/0004-6256/138/3/923](https://doi.org/10.1088/0004-6256/138/3/923)
- Östlin, G., Hayes, M., Duval, F., et al. 2014, ApJ, 797, 11, doi: [10.1088/0004-637X/797/1/11](https://doi.org/10.1088/0004-637X/797/1/11)
- Ouchi, M., Harikane, Y., Shibuya, T., et al. 2018, PASJ, 70, S13, doi: [10.1093/pasj/psx074](https://doi.org/10.1093/pasj/psx074)
- Pardy, S. A., Cannon, J. M., Östlin, G., et al. 2014, ApJ, 794, 101, doi: [10.1088/0004-637X/794/2/101](https://doi.org/10.1088/0004-637X/794/2/101)
- Partridge, R. B., & Peebles, P. J. E. 1967, ApJ, 147, 868, doi: [10.1086/149079](https://doi.org/10.1086/149079)
- Petrosian, V. 1976, ApJL, 210, L53, doi: [10.1086/182301](https://doi.org/10.1086/182301)
- Prevot, M. L., Lequeux, J., Maurice, E., Prevot, L., & Rocca-Volmerange, B. 1984, A&A, 132, 389
- Puschnig, J., Hayes, M., Östlin, G., et al. 2017, MNRAS, 469, 3252, doi: [10.1093/mnras/stx951](https://doi.org/10.1093/mnras/stx951)
- Rasekh, A., Melinder, J., Östlin, G., et al. 2022, A&A, 662, A64, doi: [10.1051/0004-6361/202140734](https://doi.org/10.1051/0004-6361/202140734)
- Reddy, N. A., Shapley, A. E., Kriek, M., et al. 2020, ApJ, 902, 123, doi: [10.3847/1538-4357/abb674](https://doi.org/10.3847/1538-4357/abb674)
- Rivera-Thorsen, T. E., Hayes, M., Östlin, G., et al. 2015, ApJ, 805, 14, doi: [10.1088/0004-637X/805/1/14](https://doi.org/10.1088/0004-637X/805/1/14)
- Rodighiero, G., Daddi, E., Baronchelli, I., et al. 2011, ApJL, 739, L40, doi: [10.1088/2041-8205/739/2/L40](https://doi.org/10.1088/2041-8205/739/2/L40)
- Runnholm, A., Hayes, M., Melinder, J., et al. 2020, ApJ, 892, 48, doi: [10.3847/1538-4357/ab7a91](https://doi.org/10.3847/1538-4357/ab7a91)
- Salim, S., Rich, R. M., Charlot, S., et al. 2007, ApJS, 173, 267, doi: [10.1086/519218](https://doi.org/10.1086/519218)
- Scarlata, C., Colbert, J., Teplitz, H. I., et al. 2009, ApJL, 704, L98, doi: [10.1088/0004-637X/704/2/L98](https://doi.org/10.1088/0004-637X/704/2/L98)
- Schlafly, E. F., & Finkbeiner, D. P. 2011, ApJ, 737, 103, doi: [10.1088/0004-637X/737/2/103](https://doi.org/10.1088/0004-637X/737/2/103)
- Smith, A., Safraneck-Shrader, C., Bromm, V., & Milosavljević, M. 2015, MNRAS, 449, 4336, doi: [10.1093/mnras/stv565](https://doi.org/10.1093/mnras/stv565)

- Sobral, D., & Matthee, J. 2019, *A&A*, 623, A157, doi: [10.1051/0004-6361/201833075](https://doi.org/10.1051/0004-6361/201833075)
- Sobral, D., Matthee, J., Darvish, B., et al. 2018, *MNRAS*, 477, 2817, doi: [10.1093/mnras/sty782](https://doi.org/10.1093/mnras/sty782)
- Steidel, C. C., Bogosavljević, M., Shapley, A. E., et al. 2011, *ApJ*, 736, 160, doi: [10.1088/0004-637X/736/2/160](https://doi.org/10.1088/0004-637X/736/2/160)
- Terlevich, E., Diaz, A. I., Terlevich, R., & Vargas, M. L. G. 1993, *MNRAS*, 260, 3, doi: [10.1093/mnras/260.1.3](https://doi.org/10.1093/mnras/260.1.3)
- Terlevich, R., Melnick, J., Masegosa, J., Moles, M., & Copetti, M. V. F. 1991, *A&AS*, 91, 285
- Trainor, R. F., Strom, A. L., Steidel, C. C., et al. 2019, *ApJ*, 887, 85, doi: [10.3847/1538-4357/ab4993](https://doi.org/10.3847/1538-4357/ab4993)
- van der Walt, S., Schönberger, J. L., Nunez-Iglesias, J., et al. 2014, *PeerJ*, 2, e453, doi: [10.7717/peerj.453](https://doi.org/10.7717/peerj.453)
- van Dokkum, P. G. 2001, *PASP*, 113, 1420, doi: [10.1086/32389410.48550/arXiv.astro-ph/0108003](https://doi.org/10.1086/32389410.48550/arXiv.astro-ph/0108003)
- Verhamme, A., Dubois, Y., Blaizot, J., et al. 2012, *A&A*, 546, A111, doi: [10.1051/0004-6361/201218783](https://doi.org/10.1051/0004-6361/201218783)
- Verhamme, A., Orlitová, I., Schaerer, D., & Hayes, M. 2015, *A&A*, 578, A7, doi: [10.1051/0004-6361/201423978](https://doi.org/10.1051/0004-6361/201423978)
- Verhamme, A., Schaerer, D., Atek, H., & Tapken, C. 2008, *A&A*, 491, 89, doi: [10.1051/0004-6361:200809648](https://doi.org/10.1051/0004-6361:200809648)
- Wisotzki, L., Bacon, R., Blaizot, J., et al. 2016, *A&A*, 587, A98, doi: [10.1051/0004-6361/201527384](https://doi.org/10.1051/0004-6361/201527384)
- Yang, H., Malhotra, S., Rhoads, J. E., et al. 2017a, *ApJ*, 838, 4, doi: [10.3847/1538-4357/aa6337](https://doi.org/10.3847/1538-4357/aa6337)
- Yang, H., Malhotra, S., Gronke, M., et al. 2017b, *ApJ*, 844, 171, doi: [10.3847/1538-4357/aa7d4d](https://doi.org/10.3847/1538-4357/aa7d4d)
- Yin, S. Y., Liang, Y. C., Hammer, F., et al. 2007, *A&A*, 462, 535, doi: [10.1051/0004-6361:20065798](https://doi.org/10.1051/0004-6361:20065798)